Raman Scattering in Carbon Nanotubes

Christian Thomsen[1] and Stephanie Reich[2]

[1] Institut für Festkörperphysik, PN5-4, Technische Universität Berlin,
Hardenbergstraße 36, 10623 Berlin, Germany
`thomsen@physik.tu-berlin.de`
[2] Department of Materials Science and Engineering,
Massachusetts Institute of Technology,
77 Massachusetts Avenue, Cambridge, MA 02139-4307, USA
`sreich@mit.edu`

Abstract. The vibrational properties of single-walled carbon nanotubes reflect the electron and phonon confinement as well as the cylindrical geometry of the tubes. Raman scattering is one of the prime techniques for studying the fundamental properties of carbon tubes and nanotube characterization. The most important phonon for sample characterization is the radial-breathing mode, an in-phase radial movement of all carbon atoms. In combination with resonant excitation it can be used to determine the nanotube microscopic structure.

Metallic and semiconducting tubes can be distinguished from the high-energy Raman spectra. The high-energy phonons are remarkable because of their strong electron–phonon coupling, which leads to phonon anomalies in metallic tubes. A common characteristic of the Raman spectra in nanotubes and graphite is the appearance of Raman peaks that correspond to phonons from inside the Brillouin zone, the defect-induced modes. In this Chapter we first introduce the vibrational, electronic, and optical properties of carbon tubes and explain important concepts such as the nanotubes' family behavior. We then discuss the Raman-active phonons of carbon tubes. Besides the vibrational frequencies and symmetries Raman spectroscopy also allows optical (excitonic) transitions, electron–phonon coupling and phase transitions in single-walled carbon nanotubes to be studied.

1 Introduction

Carbon nanotubes have attracted tremendous interest from the scientific community over the last few years since their discovery by *Iijima* in 1991 [1] and in 1993 in their single-walled form [2]. Over 15 000 publications have appeared up to the time of writing this article[1] with an ever-growing number of papers per year. The reason for this enthusiasm lies in their fascinating physical properties, which make them a model system for one-dimensional physics, their relative ease of preparation, and their large potential for applications. The combination of these features keeps the interest alive for new investigations in the research community as well as in large and small industrial companies.

---

[1] Institute of Scientific Information; general search with keywords "nanotube*".

The one-dimensionality of carbon nanotubes leads to a number of easily observable, physically interesting effects, from absorption anisotropy, depolarization effects and one-dimensional vibrational confinement to possible Luttinger-liquid behavior of the electrons. The physical properties of the "theoretical" starting material for a single-walled carbon nanotube – a sheet of graphene – are relatively well understood. Still, nanotube research has given new impetus to the study of graphite e.g., its phonon dispersion [3] or the large shift of the so-called D-mode with laser excitation energy [4]. Theoretically, the electronic dispersion of nanotubes may be described by analytic expressions using the tight-binding parameters of graphite [5], which have given access to an initial understanding of the processes involved in absorption. Improvements of this formula taking into account more distant neighbors [6] allowed a quantitative comparison of the electronic properties of graphite with those of carbon nanotubes.

The nanotube wall has a curvature with profound effects on the electronic properties, in particular of small nanotubes. The effect of $\sigma - \pi$ hybridization has been described by a symmetry-adapted nonorthogonal tight-binding model [7] and, in a more sophisticated way, by ab-initio calculations [8–10] with increasing agreement with experiment. Most recently, the effect of excitons on the absorption properties has come into focus [10–13]; we will discuss this topic in Sect. 5.3.

A number of exciting applications have emerged for carbon nanotubes. Due to their extreme toughness-to-weight ratio they have become a prime choice for mechanical reinforcement of polymers and composites [14]. The fact that they can be both semiconducting or metallic (displaying even ballistic electron transport) for slightly different atomic structures opens up the field of applications in micro or nanoelectronics. Although it is not yet possible to control the growth of one specific type (chirality) of nanotube, successful procedures for separating metallic and semiconducting nanotubes have been reported [15]. We expect schemes for specific-chirality growth to appear in the near future [16]. Identifying the chiral index – i.e., their microscopic structure – of individual isolated nanotubes via Raman scattering has become routinely possible. The nonlinear absorption properties of carbon nanotubes have opened the field of saturable absorbers in laser and optical limiters [17]. Other research has focused on the application in fiber materials [18] or as artificial muscles [19].

Raman scattering has become one of the main characterization tools for carbon nanotubes. It tells us about the quality of the material, the microscopic structure of the tube, and phonon and electron quantum confinement. Other methods, such as electron microscopy, near-field optical techniques, or tunneling measurements can give similar information. Often, though, these methods require expert knowledge in handling and are quite time consuming. They are less suited for routine characterization.

Carbon nanotubes have advanced in the general interest and found their way into several textbooks, see the book by *Reich* et al. [20] for a recent

overview of their fundamental physical properties. Older texts include those by *Dresselhaus* et al. [21, 22], *Saito* et al. [23], and *Harris* [24]. A number of review articles on specialized topics have been published recently, e.g., on the electronic states [25], Raman scattering [26], power applications of nanotubes [27], application as biosensors [28], and the behavior of nanotubes under high pressure [29]. Particularly useful collections of articles can be found in a special issue of The New Journal of Physics [30] (Eds. C. Thomsen and H. Kataura), and the Philosophical Transactions of the Royal Society [31] (Eds. A. C. Ferrari and J. Robertson).

In this Chapter, after a general introduction to structure and growth of carbon nanotubes (Sect. 2), we describe their lattice dynamics in Sect. 3, their electronic properties in Sect. 4, and their optical properties in Sect. 5. We then discuss some features of Raman scattering specific to one-dimensional systems such as the carbon nanotubes (Sect. 6). In Sect. 7 we show how, with resonant Raman spectroscopy, it is possible to find a unique assignment to the multitude of tubes with different chirality. The assignment is based on the chirality dependence of both the bandgap energies and the vibrational frequency of the radial-breathing mode (RBM) of the nanotubes. In Sect. 8 we discuss the difference between the Raman spectra of metallic and semiconducting carbon nanotubes, which is important for the different envisioned technological applications of nanotubes, e.g., as electrical connectors or in devices with transistor action. Raman scattering offers a nondestructive, efficient way of identifying this property. Some aspects of electrochemical studies of carbon nanotubes are reviewed as well. Effects of electron–phonon coupling on the Raman spectra are presented in Sect. 9. This section also deals with interference effects on the resonant Raman intensities and Kohn anomalies. In Sect. 10 the role of defects in the high-energy region of the Raman spectra are discussed; they show a strong, curious shift of one of the defect-induced modes with excitation energy, which can be explained in terms of a Raman double resonance also found in graphite [4]. Throughout the Chapter we focus on single-walled carbon nanotubes.

2 Structure and Growth

Carbon nanotubes are tiny hollow graphite-based cylinders [20, 23]. Depending on the number of graphite layers of the wall they are called single-walled (one graphite layer), double-walled (two layers), triple-walled (three layers) and so forth. Tubes with a large number of concentric cylinders – ten or more – are known as multiwall nanotubes. Graphene, a single sheet of graphite, is thus the basic building block of carbon nanotubes. We obtain a carbon nanotube by cutting a tiny strip out of a graphene sheet and rolling it up into a cylinder. This procedure is shown in Fig. 1. In the laboratory, carbon nanotubes grow from carbon plasma by adding metal catalysts.
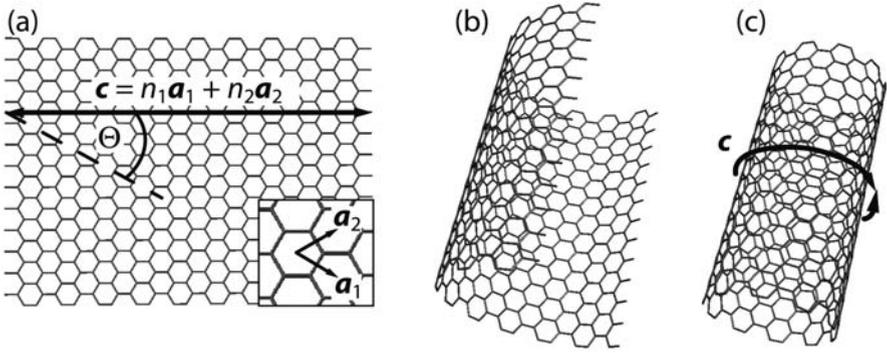
Fig. 1. Carbon nanotubes are tiny graphene cylinders. A strip is cut out of graphene (**a**) and then rolled up (**b**) to form a seamless cylinder (**c**). The chiral vector $\boldsymbol{c} = 10(\boldsymbol{a}_1 + \boldsymbol{a}_2)$ in (**a**) forms the circumference of the (10,10) nanotube in (**c**). Along the nanotube axis the unit cell is repeated periodically, i.e., a nanotube is a one-dimensional periodic system. The segment shown in (**c**) contains 13 unit cells along the nanotube axis. The *inset* in (**a**) shows the graphene lattice and the graphene unit cell vectors $\boldsymbol{a}_1$ and $\boldsymbol{a}_2$ on an enlarged scale

Before discussing the growth, we introduce the basic concepts and parameters that determine the properties of carbon nanotubes. As can be seen in Fig. 1a the cutting of graphene fixes the so-called chiral or roll-up vector $\boldsymbol{c}$. This vector goes around the circumference of the final tube in Fig. 1c. There are two parameters that control the microscopic structure of a nanotube, its diameter and its chiral angle or twist along the axis. Both are specified completely by $\boldsymbol{c}$, which is normally given in terms of the graphene lattice vectors $\boldsymbol{a}_1$ and $\boldsymbol{a}_2$ (see inset of Fig. 1a)

$$\boldsymbol{c} = n_1\boldsymbol{a}_1 + n_2\boldsymbol{a}_2 \,. \tag{1}$$

(n_1, n_2) are called the chiral index of a tube or, briefly, the chirality. A tube is characterized by (n_1, n_2). In Fig. 1c we show as an example the (10,10) nanotube.

The diameter of a tube is related to the chiral vector by

$$d = \frac{|\boldsymbol{c}|}{\pi} = \frac{a_0}{\pi}\sqrt{n_1^2 + n_1 n_2 + n_2^2} \,, \tag{2}$$

where $a_0 = 2.460\,\text{Å}$ is the graphene lattice constant [32–35]. For small tubes ($d < 0.8\,\text{nm}$) the diameter is predicted to deviate from the geometrical diameter of a graphene cylinder in (2). Moreover, ab-initio calculations show that d becomes a function of the chiral angle below 0.8 nm [36]. Deviations from (2) are below 2 % for tube diameters $d \geq 5\,\text{Å}$ [36]. Note also that sometimes different lattice constants are used to calculate d. A popular value is $a_0 = 2.494\,\text{Å}$ obtained from a carbon–carbon distance $a_{\text{CC}} = a_0/\sqrt{3} = 1.44\,\text{Å}$; this value
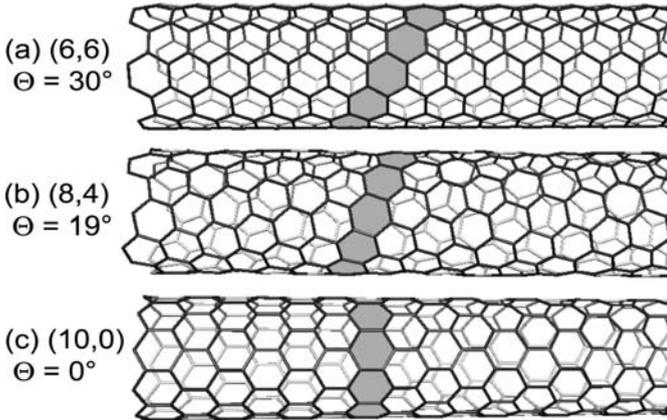
Fig. 2. Three carbon nanotubes with diameters around 0.8 nm: (**a**) (6,6) armchair, (**b**) (8,4) chiral tube and (**c**) (10,0) zigzag nanotube. The *gray hexagons* indicate the helix around the nanotube

for a_{CC} was most likely taken from fullerenes that have a larger carbon–carbon spacing than graphite and carbon nanotubes [37].

The second important parameter for carbon nanotubes is the chiral angle Θ, which is the angle between $\boldsymbol{a}_1$ and the chiral vector (see Fig. 1a). The chiral angle specifies the arrangement of the graphene hexagons on the wall of the tube. This is illustrated in Fig. 2, where we show three single-walled nanotubes with similar diameters but very different microscopic structure due to different chiral angles. Θ is related to the chiral index by

$$\Theta = \arccos\left[\frac{n_1 + n_2/2}{\sqrt{n_1^2 + n_1 n_2 + n_2^2}}\right],$$

or

$$= 30° - \arctan\left[\frac{1}{\sqrt{3}}\frac{n_1 - n_2}{n_1 + n_2}\right]. \tag{3}$$

The chiral angle is allowed to vary between $0° \leq \Theta \leq 30°$; all other ranges of Θ are equivalent to this interval because of the hexagonal symmetry of graphene (see Fig. 1a). A chiral angle of $0°$ and $30°$ corresponds to tubes with a particular high symmetry, as we discuss later. They are called *zigzag* ($\Theta = 0°$) and *armchair* tubes ($\Theta = 30°$).

The chiral vector not only determines the tube diameter and chiral angle, but all other structural parameters including the length of the unit cell and the number of carbon atoms in the unit cell. A compilation of these parameters can be found in Table 1.

A very useful illustration for the chiral vectors is to draw all possible nanotubes of a given diameter range onto a graphene lattice as in Fig. 3.

Table 1. Structural parameters, symmetry and reciprocal lattice vectors of single-walled carbon nanotubes. Armchair and zigzag tubes are special cases of the general expression given in the last column. n is the greatest common divisor of n_1 and n_2. n_c and q are the number of carbon atoms and the number of graphene hexagons in the nanotube unit cell, respectively; wv stands for wavevector. m is the z component of the angular momentum quantum number; it indexes electronic and vibrational bands of carbon nanotubes and takes only integer values

Parameter	Armchair	Zigzag	Chiral
	(n, n)	$(n, 0)$	(n_1, n_2)
Chiral vector $\boldsymbol{c}$	$n(\boldsymbol{a_1} + \boldsymbol{a_2})$	$n\boldsymbol{a_1}$	$n_1\boldsymbol{a_1} + n_2\boldsymbol{a_2}$
Diameter d	$\sqrt{3}a_0 n/\pi$	$a_0 n/\pi$	$a_0\sqrt{n_1^2 + n_1 n_2 + n_2^2}/\pi$
Chiral angle Θ	$30°$	$0°$	$30° - \arctan\dfrac{1}{\sqrt{3}}\dfrac{n_1 - n_2}{n_1 + n_2}$
Lattice vector $\boldsymbol{a}$	$-\boldsymbol{a_1} + \boldsymbol{a_2}$	$-\boldsymbol{a_1} + 2\boldsymbol{a_2}$	$-\dfrac{2n_2 + n_1}{n\mathcal{R}}\boldsymbol{a_1} + \dfrac{2n_1 + n_2}{n\mathcal{R}}\boldsymbol{a_2}$
Lattice const. a	a_0	$\sqrt{3}a_0$	$a_0\dfrac{\sqrt{3(n_1^2 + n_1 n_2 + n_2^2)}}{n\mathcal{R}}$
Point group	D_{2nh}	D_{2nh}	D_q
$n_c = 2q$	$4n$	$4n$	$4\dfrac{(n_1^2 + n_1 n_2 + n_2^2)}{n\mathcal{R}}$
$\mathcal{R}$	3	1	3 if $(n_1 - n_2)/3n = $ integer 1 if $(n_1 - n_2)/3n \neq $ integer
Quantized wv $\boldsymbol{k_\perp}$	$\dfrac{\boldsymbol{k_1} + \boldsymbol{k_2}}{2n}$	$\dfrac{\boldsymbol{k_1}}{n} + \dfrac{\boldsymbol{k_2}}{2n}$	$\dfrac{2n_1 + n_2}{qn\mathcal{R}}\boldsymbol{k_1} + \dfrac{2n_2 + n_1}{qn\mathcal{R}}\boldsymbol{k_2}$
Axial wv $\boldsymbol{k_z}$	$\dfrac{-\boldsymbol{k_1} + \boldsymbol{k_2}}{2}$	$\dfrac{\boldsymbol{k_2}}{2}$	$\dfrac{-n_2\boldsymbol{k_1}}{q} + \dfrac{n_1\boldsymbol{k_2}}{q}$
Range of m	$-(n-1)\ldots n$	$-(n-1)\ldots n$	$-(q/2 - 1)\ldots q/2$
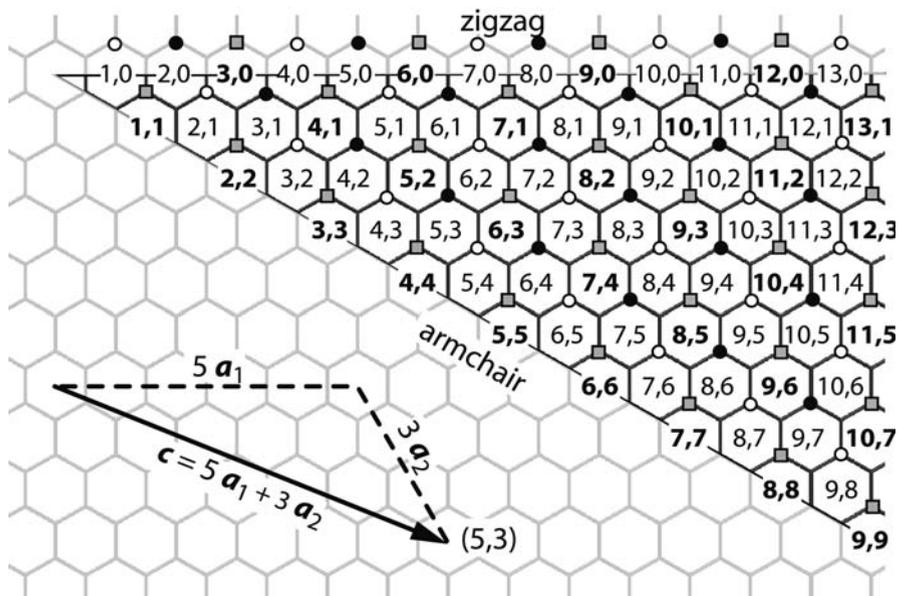
Fig. 3. Chiral indices of single-walled carbon nanotubes mapped onto a graphene sheet for tube diameters $d \leq 1.2$ nm. The *small symbols* at the upper corner of a hexagon indicate the family of a nanotube. *Closed circles* are semiconducting tubes belonging to the $\nu = (n_1 - n_2) \mod 3 = -1$ family; *open circles* belong to the $\nu = +1$ family, the second semiconducting family. *Squares* are tubes from the $\nu = 0$ family; their chiral indices are in boldface. These tubes are metallic or quasimetallic, which means that their electronic bandgap is 10 meV to 100 meV and induced by the curvature of the nanotube wall. Note that tubes from one family are connected by the three armchair-like directions. Nanotube indices that are connected by the vertical armchair-like direction belong to the same nanotube branch (see also Table 2)

This plot highlights systematics in the nanotube properties such as their metallic and semiconducting character, the family behavior, and nanotube branches. We will discuss these topics throughout this Chapter. In the lower left part of Fig. 3 we show in detail how to construct a (5,3) nanotube on a graphene sheet.

The series of $(n, 0)$ zigzag nanotubes that run horizontally in Fig. 3 have $\Theta = 0°$. The name derives from the zigzag chain that forms the edge of this high-symmetry type of tubes (see Fig. 2c). The other high-symmetry nanotube structures are the (n, n) armchair tubes with $\Theta = 30°$. The edge of their unit cell resembles a row of armchairs when viewed from above (Fig. 2a), hence the name. Zigzag and armchair tubes are both called *achiral* tubes. A general nanotube with lower symmetry, like the (8,4) tube in Fig. 2b, is referred to as *chiral*.

Table 2. Frequently used classifications for a general nanotube used in this work. Families and branches may be visualized as lines parallel to the armchair direction and as vertical lines in Fig. 3, respectively. "Neighbor" refers to the nanotube closest to a particular one on the same branch and with $d' \geq d$

	Symbol	Definition	Remark
Family index	ν	$(n_1 - n_2) \mod 3$	$\nu = 0, \pm 1$ (or $\nu = 0, 1, 2$) lines parallel to armchair
Semiconducting	S	$(n_1 - n_2) \mod 3 = \pm 1$	
Metallic	M	$(n_1 - n_2) \mod 3 = 0$	
Branch index	β	$2n_1 + n_2$	vertical lines in Fig. 3
Neighbor	(n_1', n_2')	$(n_1 - 1, n_2 + 2)$	$n_1' \geq n_2'; \beta = \text{const}$

Achiral tubes have a number of properties that distinguish them from chiral tubes. For example, armchair nanotubes are the only tubes where the electronic bandgap is strictly zero. From a practical point of view the number of carbon atoms in the unit cell n_c is much smaller in achiral than in chiral tubes of the same diameter, see Table 1. Most calculations of, e.g., the lattice dynamics or the electronic band structure have been performed for armchair and zigzag tubes [38, 39]. This should be kept in mind when comparing experiment and theory, since chiral tubes greatly outnumber the achiral species in real samples.

Carbon nanotubes are grown by three major methods, laser ablation, arc-discharge, and chemical vapor deposition (CVD) and CVD-related processes [1, 2, 40, 44, 45, 49–54]. All growth processes have in common that a carbon plasma is formed either by heating or by chemical decomposition. Tubes grow when metal catalysts are added to this plasma. The type of catalyst and the growth conditions determine whether single, double or multiwall tubes are obtained; the latter also grow in small quantities without any catalysts. Besides the number of walls, the yield, tube diameter and length can be controlled during growth. Table 3 lists some typical values for the tubes most widely used in optical studies.

Different methods used to grow carbon nanotubes have their advantages and disadvantages [52]. We are not going to discuss them in detail. The first processes that produced nanotubes with high yield were arc-discharge and laser ablation [40, 51].

A scanning electron microscopy (SEM) image of carbon nanotubes grown by arc-discharge is shown in Fig. 4a. The web-like structure consists of nanotube bundles. Every bundle or rope in Fig. 4a is formed by 20–100 single-walled nanotubes, as can be seen in the high-resolution transmission electron
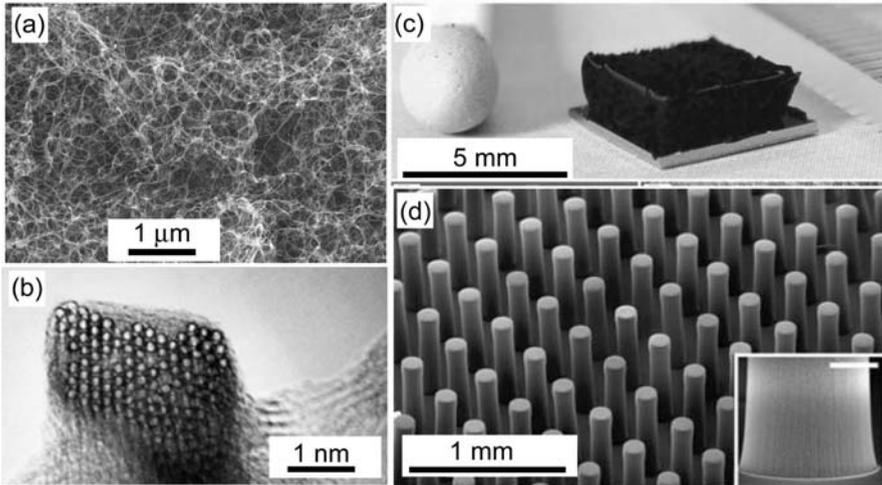
Fig. 4. (**a**) SEM images of single-walled carbon-nanotube bundles. (**b**) High-resolution TEM image showing the cross section of a bundle of tubes. Every circle is the circumference of a single-walled carbon nanotube. The tubes are arranged in a hexagonal packing. (**c**) Water-assisted CVD-grown carbon nanotubes of high purity and length. The nanotube mat is shown next to the head of a matchstick. (**d**) A patterned substrate allows the growth of carbon nanotubes in predefined places as shown in this SEM picture. The *inset* displays an expanded view of one of the pillars. After [40] and [41]

microscope picture in part (b) of the figure. In such a bundle the tubes are packed in a two-dimensional hexagonal lattice.

The bundling results from the attractive van-der-Waals forces between nanotubes [55–58]. For more than ten years it had been a great challenge to break these bundles and prevent the isolated tubes from rebundling. This problem was solved in 2002 by a postprocessing routine [59], where first the bundles are broken apart by ultrasonification. The tubes are then coated by a surfactant to eliminate interactions between them. Finally, the remaining small bundles with 3–10 tubes are removed from the solution with a centrifuge [59]. In this way, solutions with isolated nanotubes were produced for a wide range of nanotubes [44, 59–62].

Finding a way to produce large quantities of isolated nanotubes in solution is particularly important for optical studies and Raman spectroscopy on single-walled carbon nanotubes [60, 63–65]. In contrast to bundled tubes, isolated nanotubes behave like truly one-dimensional systems from an optical point of view. They show sharp absorption peaks and Raman resonances [59, 63]; they also emit light in the near infrared [60]. Based on optical spectroscopy of isolated nanotubes in solution it was possible – for the first time – to determine which nanotube chiralities are present in a sample [44, 60–64]. These topics will be discussed in Sects. 5 and 7.

Table 3. Typical diameters for carbon nanotubes grown by different methods. σ is the standard deviation of a Gaussian distribution. The length is categorized as short (below 100 nm), medium (100 nm to 1000 nm) and long (above 1 µm). A special, ultralong case is the 4 cm nanotube reported in [42]. The "special" tubes types (HiPCo, CoMocat etc.) are all grown by CVD-related processes

Growth method	d (nm)	σ (nm)	Length	Remark
Laser ablation	1.5	0.1	medium	
Arc-discharge	1.5	0.1	medium	
CVD	strongly varying depending on catalyst and growth conditions			
HiPCo	1.0	0.2	medium	[43]
CoMoCat	0.7	0.1	medium	[44]
Alcohol	0.7	0.1	medium	[45]
Zeolites	0.4	–	short	[46]
cm tubes	1.4	–	ultralong	[42]
Supergrowth	2.0	1.0	long	[41]
Double-walled tubes (inner tube diameters)				
CVD	0.7	0.05		[47]
Peapods	0.75	0.05		[48]

Chemical vapor deposition recently evolved into the most widely used growth technique, because it is cheap, scalable and allows a high degree of control over the tubes. With CVD it is possible to grow nanotubes on well-defined places with patterned substrates and, e.g., to produce an individual tube that bridges two catalytic particles [66, 67]. Also, CVD tends to produce isolated rather than bundled tubes, which is interesting for optical spectroscopy [68, 69], and it works at lower growth temperatures [70]. The great disadvantage of CVD is the lower quality of the nanotubes obtained.

A major step forward in terms of quality, purity, yield, and length of CVD tubes was recently reported by *Hata* et al. [41]. By adding water during the CVD process they obtained mm-thick mats of single-walled nanotubes. Figure 4c compares such a mat with a matchstick. The nanotube forest is free of catalytic particles and amorphous carbon. These two contaminations are normally present in as-grown tube samples and need to be removed by subsequent purification. Figure 4d demonstrates how the places in which the tubes grow can be defined by patterning the substrate.

The growth of carbon nanotubes remains a rapidly evolving field. Especially on the theoretical side much needs to be done for a better understanding of the processes. The major challenge for the growth of carbon nanotubes is to grow tubes with a unique chirality. We mentioned that the tube diameter can
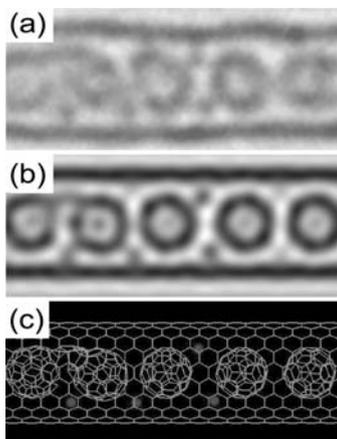
Fig. 5. (**a**) High-resolution transmission-electron-microscope image of a potassium-doped C_{60} peapod. (**b**) A simulation of the image. (**c**) Model of the doped peapods. Seen are the nanotube walls (*horizontal dark lines*), the fullerene molecules (large circular molecules), and the potassium doping atoms (*small black dots*). From [71]

be controlled to some extent by the growth parameters. What about the second important parameter, the chiral angles of the tubes? The general answer is that nanotube samples show a homogeneous distribution of chiral angles from armchair to zigzag [72, 73]. There seems to be some preference for specific chiralities when the tube diameters are very small ($d < 0.8\,\mathrm{nm}$) [44, 45]. This conclusion was drawn, however, from optical spectroscopy under the assumption that the cross section is independent of chirality. This assumption is most likely incorrect [74, 75]. For fundamental studies and Raman scattering, in particular, nanotube samples with a unique type of tube are not as critical as, e.g., for applications. By tuning the laser-excitation energy we can now select a specific nanotube chirality with resonant Raman scattering. This will be discussed in Sect. 7.

Carbon nanotubes can be prepared containing small molecules and one-dimensional crystals. We show in Fig. 5, as an example, an image of so-called peapods, that is, nanotubes containing C_{60} molecules. Such peapods were discovered by *Smith* et al. [76] and produced in large quantities by *Kataura* et al. [77]. The peapods used for the image in Fig. 5 were doped with potassium. One can readily see the K-atoms in the image. From a study of the electronic state of the potassium atoms *Guan* et al. [71] were able to show that the peapod was n-doped, suggesting that electrically conductive nanowires are technologically feasible. Doped peapods were also studied with Raman scattering by *Pichler* et al. [78]. For more details on the determination of the charge state of doped peapods, see [71, 78] and Sect. 8.3.

Another example of inorganic molecules or crystals prepared in nanotubes is shown in Fig. 6 [79]. The image shows two layers of a KI crystal in the carbon nanotube. It is remarkable that the atoms in the KI crystal all lie at the surface; the crystal has no "volume". The structural and electronic properties of one-dimensional crystals of this type can be investigated only if the surface atoms are passivated, here by the surrounding nanotube. Possible
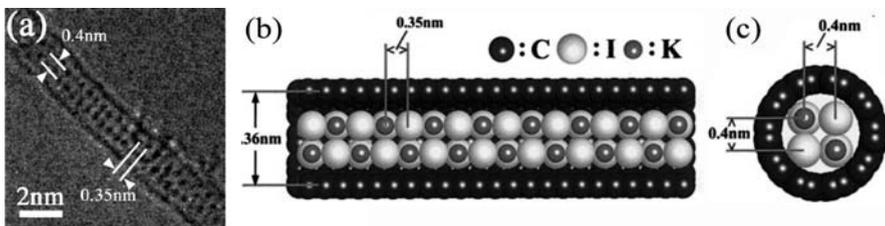
Fig. 6. (**a**) High-resolution transmission electron microscope (TEM) image of a bilayer crystal of potassium iodide grown inside a carbon nanotube with diameter of $\approx 1.36\,\text{Å}$. (**b**) Model of the KI crystal-in-nanotube image of (**a**). (**c**) Cross section of this nanotube. After [79]

structures of alkali halide clusters have been predicted by *Diefenbach* and *Martin* [80].

3 Lattice Dynamics

Carbon nanotubes have many vibrational degrees of freedom because of the large number of atoms in their unit cells. Achiral tubes of $d \approx 1\,\text{nm}$ diameter have 100–150 phonon branches; in chiral nanotubes this number can be higher by one or two orders of magnitude. Only a very small fraction of these phonons is Raman or infrared active. The Raman-active modes fall into a low-energy range where radial vibrations are observed, a high-energy range with inplane carbon–carbon vibrations, and an intermediate-frequency range. The low- and high-energy phonons have received most attention; their Raman signal is very strong and they can be used for characterizing and studying nanotubes as they give information about the tube diameter and chirality, phonon confinement, the semiconducting or metallic character, optical transition energies and more. In this section we first study the number of nanotube vibrations and their symmetry from group theory. Then we discuss the distinct energy ranges of the phonons that can be studied by optical spectroscopy.

3.1 Symmetry

Carbon nanotubes are structures with particularly high symmetry. This comes from the underlying hexagonal lattice. The translations of graphene turn into rotational and helical symmetry operations for nanotubes, because we build the tube by rolling up graphene. The symmetry of carbon nanotubes was rigorously derived within the framework of line groups [81, 82]. Line groups deal with systems that are periodic in one dimension. They are the equivalent of crystal space groups for one-dimensional solids. The line-group treatment is very powerful, see *Reich* et al. [20] for an introduction
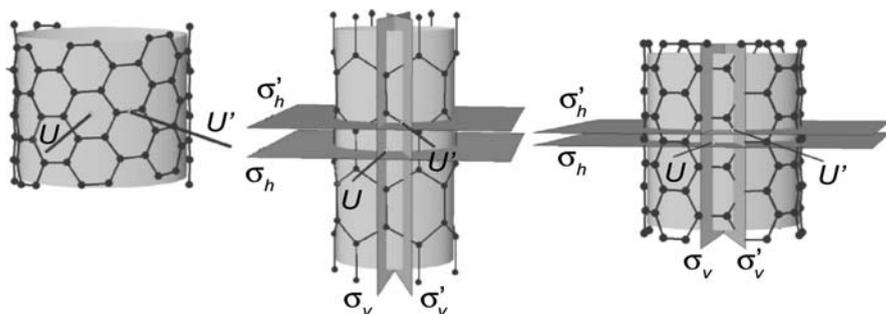
Fig. 7. Symmetry operations of chiral (*left*), zigzag (*middle*) and armchair (*right*) nanotubes. Besides the operations shown here all tube types also have a principal screw axis – achiral tubes also have a principal rotation axis. U and U' are frequently denoted by C_2' and C_2'', respectively. In all three panels, primed operations involve translations by a fraction of the nanotube lattice vector $\boldsymbol{a}$. From [81]

and [83–88] for applications of the method to carbon nanotubes. Here we will use the isogonal point groups of single-walled carbon nanotubes to discuss their symmetry. We assume that the reader is familiar with this aspect of group theory [89, 90].

Looking back at the (10,0) nanotube in Fig. 2c a number of symmetry operations are apparent: We can rotate the tube by $360°/10 = 36°$ about its z-axis, the nanotube axis. There is a series of so-called primed rotations, which are perpendicular to z. The most obvious one has its rotational axis normal to the paper. We can also reflect the lattice at a mirror plane normal to z going through the centers of the hexagons (horizontal mirror plane). And, finally, one can identify a set of vertical mirror planes including the nanotube axis and the carbon–carbon bonds parallel to it [81].

The symmetry operations mentioned so far do not require a translation of the tube by a fraction of its lattice vector $\boldsymbol{a}$. There is, however, a second set of operations in a (10,0) nanotube that preserve the lattice. They involve translations, i.e., screw axes and glide planes. The main screw axis is best seen for the (6,6) nanotube in Fig. 2a. The tube can be rotated by $360°/6 = 60°$, but we can also apply a rotation by 30° followed by a translation by $\boldsymbol{a}/2$. This generates the helix twisting around the tube's circumference (gray hexagons in Fig. 2a). Likewise, the (8,4) and (10,0) tubes have a screw axis. In addition, carbon nanotubes always have two sets of C_2 rotations perpendicular to z, see U and U' in Fig. 7. Achiral tubes possess two horizontal (σ_{h}, σ_{h}') and two sets of vertical (σ_{v}, σ_{v}') mirror planes (see Fig. 7).

The isogonal point group of a carbon nanotube depends on its chirality. (n, n) armchair and $(n, 0)$ zigzag tubes belong to D_{2nh}; chiral (n_1, n_2) nanotubes to D_q, where q is the number of hexagons in the unit cell of the tube [81], see Table 1. The character table for these groups is given in Table 3.1.

Table 4. Character table of the D_{qh} point groups with even q, which applied to all nanotubes (q is always even, see Table 1). $\alpha = 2\pi/q$, $n = q/2$. To obtain the table for D_q omit the inversion I plus all following symmetry operations and drop the subscripts g and u. The basis functions indicate the translations ($T_{x,y,z}$) and rotations ($R_{x,y,z}$). Phonons belonging to the translational representations are infrared active. The Raman activity is indicated in the last column, which also gives the Raman selection rules

D_{qh}	E	$2C_q$	$2C_q^2$	...	$C_q^n = C_2$	$\frac{q}{2}C_2 = U$	$\frac{q}{2}C_2'' = U'$	I	$2IC_q$	$2IC_q^2$	...	$IC_2 = \sigma_h$	$\frac{q}{2}\sigma_v$	$\frac{q}{2}\sigma_{v'}$	Basis functions
A_{1g}	1	1	1	...	1	1	1	1	1	1	...	1	1	1	$\alpha_{xx}+\alpha_{yy},\alpha_{zz}$
A_{1u}	1	1	1	...	1	1	1	-1	-1	-1	...	-1	-1	-1	
A_{2g}	1	1	1	...	1	-1	-1	1	1	1	...	1	-1	-1	R_z
A_{2u}	1	1	1	...	1	-1	-1	-1	-1	-1	...	-1	1	1	T_z
B_{1g}	1	-1	1	...	$(-1)^n$	1	-1	1	-1	1	...	$(-1)^n$	1	-1	
B_{1u}	1	-1	1	...	$(-1)^n$	1	-1	-1	1	-1	...	$-(-1)^n$	-1	1	
B_{2g}	1	-1	1	...	$(-1)^n$	-1	1	1	-1	1	...	$(-1)^n$	-1	1	
B_{2u}	1	-1	1	...	$(-1)^n$	-1	1	-1	1	-1	...	$-(-1)^n$	1	-1	
E_{1g}	2	$2\cos\alpha$	$2\cos2\alpha$	...	-2	0	0	2	$2\cos\alpha$	$2\cos2\alpha$	...	-2	0	0	(R_x,R_y) $(\alpha_{yz},\alpha_{zx})$
E_{1u}	2	$2\cos\alpha$	$2\cos2\alpha$	...	-2	0	0	-2	$-2\cos\alpha$	$-2\cos2\alpha$	...	2	0	0	(T_x,T_y)
E_{2g}	2	$2\cos2\alpha$	$2\cos4\alpha$	...	2	0	0	2	$2\cos2\alpha$	$2\cos4\alpha$	...	2	0	0	$(\alpha_{xx}-\alpha_{yy},\alpha_{xy})$
E_{2u}	2	$2\cos2\alpha$	$2\cos4\alpha$	...	2	0	0	-2	$-2\cos2\alpha$	$-2\cos4\alpha$	...	-2	0	0	
...	...	...	...	...	...	...	...	...	...	...	...	...	...	...	
$E_{(n-1)g}$	2	$2\cos(n-1)\alpha$	$2\cos2(n-1)\alpha$	...	$2\cos(n-1)\pi$	0	0	2	$2\cos(n-1)\alpha$	$2\cos2(n-1)\alpha$	...	$2\cos(n-1)\pi$	0	0	
$E_{(n-1)u}$	2	$2\cos(n-1)\alpha$	$2\cos2(n-1)\alpha$	...	$2\cos(n-1)\pi$	0	0	-2	$-2\cos(n-1)\alpha$	$-2\cos2(n-1)\alpha$	...	$-2\cos(n-1)\pi$	0	0	

Table 5. Phonon symmetries of single-walled carbon nanotubes

Tube	Phonon symmetry	m
(n,n) armchair		
n even	$2(A_{1g} + A_{2g} + B_{1g} + B_{2g}) + A_{2u} + A_{1u} + B_{2u} + B_{1u}$ $+ \sum_{m\,\mathrm{odd}} (4E_{mu} + 2E_{mg}) + \sum_{m\,\mathrm{even}} (4E_{mg} + 2E_{mu})$	$[1, n-1]$
n odd	$2(A_{1g} + A_{2g} + B_{1u} + B_{2u}) + A_{2u} + A_{1u} + B_{2g} + B_{1g}$ $+ \sum_{m\,\mathrm{odd}} (4E_{mu} + 2E_{mg}) + \sum_{m\,\mathrm{even}} (4E_{mg} + 2E_{mu})$	$[1, n-1]$
$(n,0)$ zigzag	$2(A_{1g} + A_{2u} + B_{1g} + B_{2u}) + A_{2g} + A_{1u} + B_{2g} + B_{1u}$ $+3\sum_{m}(E_{mg} + E_{mu})$	$[1, n-1]$
(n_1,n_2) chiral	$3(A_1 + A_2 + B_1 + B_2) + 6\sum_{m} E_m$	$[1, \frac{q}{2} - 1]$

In the literature, one often finds lower point group symmetries for both achiral and chiral nanotubes [21, 23, 91–94]. We want to comment on this, because the (incorrect) lower-symmetry groups strongly affect the phonon-selection rules. Essentially, they double the number of Raman-active vibrations in armchair and zigzag tubes [20, 93]. For chiral tubes the effect is less pronounced; we expect one totally symmetric A_1 phonon less when using the correct nanotube symmetry [82]. The screw axes and the glide planes of achiral nanotubes are often neglected in the literature [23]. These symmetry operations were most likely ignored because in the early days of nanotube research carbon nanotubes were modeled as extended fullerenes [91]. Typical carbon nanotubes, however, are at least several hundred of nanometers long. A description as a one-dimensional solid is therefore much more adequate than the molecular approach.[2] In chiral tubes the C_2 rotations perpendicular to the nanotube axis are often missing. This seems to be due to an error in the first publication about the symmetry of chiral tubes [95].

From the point group and the positions of the carbon atoms the number and symmetry of the phonon eigenvectors are found by one of the standard procedures [20, 81, 89, 90, 96]. The symmetries of the eigenmodes are given in Table 5. A and B modes are nondegenerate; E modes have a twofold degeneracy. The character table (Table 3.1) shows that the $A_{1(g)}$, $E_{1(g)}$ and $E_{2(g)}$

---

[2] The solid-state and the molecular picture must not be mixed. When using solid-state concepts such as band structures and phonon dispersions, translations need to be included among the symmetry operations.

representations are Raman active (the subscript g represents achiral tubes). We thus obtain a total of 8 Raman-active phonons in achiral and 15 in chiral nanotubes

$$
\begin{array}{ll}
\text{armchair} & 2A_{1g} \oplus 2E_{1g} \oplus 4E_{2g} \\
\text{zigzag} & 2A_{1g} \oplus 3E_{1g} \oplus 3E_{2g} \\
\text{chiral} & 3A_1 \ \oplus 6E_1 \ \oplus 6E_2 \, .
\end{array}
\tag{4}
$$

The totally symmetric modes in achiral tubes are the radial-breathing vibration, which is discussed in the next section, and a high-energy phonon. In armchair tubes the circumferential eigenvector is Raman active; in zigzag tubes the axial vibration. In chiral nanotubes, the three totally symmetric modes are the radial-breathing mode and two high-frequency vibrations. They resemble the circumferential and axial vibrations, but are, in general, of mixed character. This is typical for low-dimensional systems; it originates from the mechanical boundary conditions (around the circumference in the case of nanotubes) [38, 97, 98]. As we show in Sect. 6 the Raman spectrum of carbon nanotubes is dominated by scattering from totally symmetric phonons [99–102]. In the following we discuss the radial vibrations of carbon nanotubes and, in particular, the radial-breathing mode before turning to the high-energy frequencies.

3.2 Radial-Breathing Mode

The radial-breathing mode (RBM) is an important mode for the characterization and identification of specific nanotubes, in particular of their chirality. Its eigenvector is purely radial by symmetry for armchair tubes only; these have mirror planes perpendicular to the nanotube axis, and the radial-breathing mode is fully symmetric. For all other chiralities $n_1 \neq n_2$ the eigenvector has a small axial component, which is largest for zigzag tubes [36, 103, 104]. For most practical purposes, however, the radial-breathing mode may be considered purely radial. In Fig. 8 we show its eigenvector for an (8,4) nanotube.

The significance of the radial-breathing mode for the characterization of nanotubes comes from the inverse dependence of its frequency on the diameter of the nanotube

$$
\omega_{\text{RBM}} = \frac{c_1}{d} + c_2 \, .
\tag{5}
$$

This quite general relationship may be derived, e.g., from the continuum mechanics of a small hollow cylinder as shown by *Mahan* [105]. From one of the solutions to the standard wave equation for sound in homogeneous solids, one obtains the frequency of the breathing mode[3]

$$
\omega_{\text{RBM}} = \frac{v_{\text{B}}}{2\pi c d} \, ,
\tag{6}
$$

---

[3] Note that in (6) the phonon frequency has units of cm^{-1}. This is the common definition in the nanotube community for the quantity "wave number", $\tilde{k} = \lambda^{-1}$, and differs from that of Mahan.

(8,4)
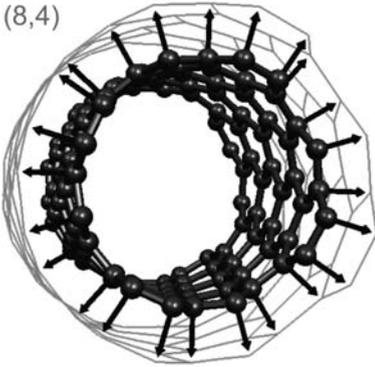
Fig. 8. Radial-breathing mode of an (8,4) nanotube. Shown are the displacement vectors of the atoms along the radius vector. In armchair nanotubes the eigenvectors are *exactly* radial, in all other tubes the eigenvector has a small axial component (on the order of 10^{-3} of the radial component) [103, 104]

with the velocity v_B given by

$$v_B = 4c_t \sqrt{1 - \frac{c_t}{c_l}} \approx 42.8 \, \text{km/s}. \tag{7}$$

The constants $c_t = (C_{66}/\rho)^{1/2} = 14.0 \, \text{km/s}$ and $c_l = (C_{11}/\rho)^{1/2} = 21.7 \, \text{km/s}$ are the transverse and longitudinal sound velocities ($C_{66} = 44 \times 10^{11} \, \text{dyn/cm}^2$, $C_{11} = 106 \times 10^{11} \, \text{dyn/cm}^2$ [106–108], and $\rho = 2.66 \, \text{g/cm}^3$, the density of graphite). Inserting the velocity (7) in (6) yields

$$\omega_{RBM} = \frac{227 \, \text{cm}^{-1} \cdot \text{nm}}{d}, \tag{8}$$

which is in very good quantitative agreement with other calculations for isolated nanotubes and with experiment, as we shall see.

The constant c_2 in (5) is believed to describe the additional interaction in bundles of nanotubes. For a compilation of values for c_1 and c_2 both from experiment and theory (see Table 8.2 in Ref. [20]). Alternative ways of showing the inverse dependence of ω_{RBM} on diameter have been published by *Jishi* et al. [95] and *Wirtz* et al. [109].

The problem with using (5) to find the chiral index in practice is that many slightly different nanotubes lie in a small range of diameters. The experimental uncertainty of the constants in (5) is too large to find uniquely the chiral index of a specific tube. To give an example, for a diameter distribution centered around 0.95 nm with $\sigma \approx 0.2$ nm, as is typical for the HiPCO process, there are 40 chiral indices to be assigned. In laser-ablation-grown samples the mean diameters are larger and, correspondingly, many more chiralities fall into the range of tubes to be identified in a sample.
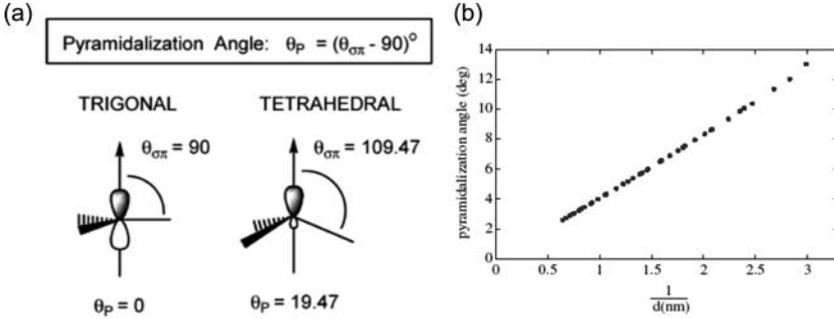
Fig. 9. (a) Definition of the pyramidalization angle θ_{p} [110]; $\theta_{\mathrm{p}} = 0°$ corresponds to sp^2- and $\theta_{\mathrm{p}} = 19.47°$ to sp^3-coordinated carbon. **(b)** Plot of θ_{p} as a function of inverse tube diameter showing how smaller tubes lead to a more sp^3-type coordination of the carbon atoms. After [36]

It turns out that only the simultaneous measurement of the radial-breathing mode frequency and the optical transition energies by resonant Raman spectroscopy yields sufficient information to identify uniquely the chiral index (n_1, n_2) of a nanotube. We will show how this works in Sect. 7.

3.2.1 Chirality Dependence

As the diameter of the nanotubes becomes smaller, the deviations from the analogy to graphene and the continuum-like models become larger. This concerns the geometric changes introduced by the curvature of the nanotube as well as the deviations of the radial-breathing mode frequency from the large-d behavior in (5). Aside from bond-length changes and bond-angle distortions *Niyogi* et al. [110] considered the chemical reactivity that arises from increasing sp^3 components in the bonds of rolled-up graphene. They defined the pyramidalization angle θ_{p} as the difference between $90°$ and the angle between the inplane σ and out-of-plane π bonds in the trigonal configuration (graphite or graphene). Graphene thus has $\theta_{\mathrm{p}} = 0°$; the other limit is $\theta_{\mathrm{p}} = 19.47°$, which corresponds to purely tetrahedrally bonded carbon (diamond) (see Fig. 9a).

Figure 9b shows the pyramidalization angle θ_{p} as function of inverse diameter for tubes in the diameter range $0.3\,\mathrm{nm}$ to $1.5\,\mathrm{nm}$. While it is clear that larger tubes (say, diameter $\geq 1\,\mathrm{nm}$) are not affected much, tubes with diameter below $0.5\,\mathrm{nm}$ have bonds with considerable sp^3 character. Fullerenes, by comparison, have $\theta_{\mathrm{p}} = 11.4°$ [110].

These geometric deviations lead naturally also to deviations of the radial-breathing mode frequency from the simple $1/d$ relationship. Because of the different symmetry of armchair and zigzag nanotubes, the zigzag tubes are more strongly affected by increasing curvature. This is shown in Fig. 10, where the deviation of ω_{RBM} from the value predicted by (5) is plotted vs. diameter
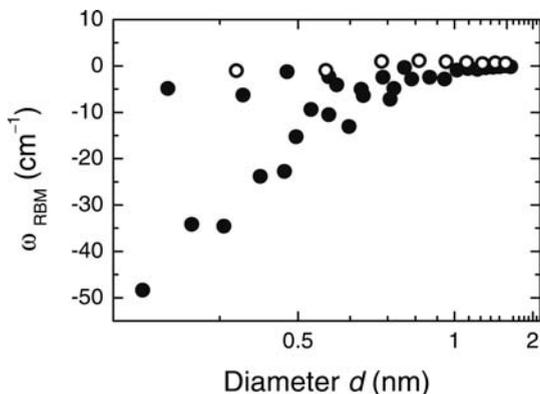
Fig. 10. Frequency of the radial-breathing mode vs. log d to illustrate the departure from the simple $1/d$ behavior predicted by (5). The deviations become larger for smaller nanotubes. Armchair nanotubes (*open symbols*) are not affected. After [36]
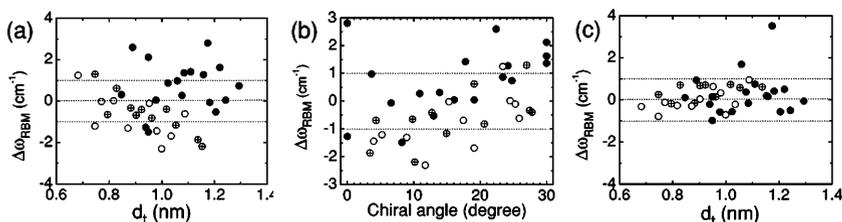
Fig. 11. Frequency differences $\Delta\omega_{RBM}$ of the radial-breathing mode with respect to the simple $1/d$ behavior, as a function of nanotube diameter (**a**) and chiral angle (**b**). The *horizontal lines* indicate the $1/d$ approximation and the experimental error bars of the measurement. A higher parametrization, (9), leads to a much better description of the data (**c**). *Open circles*, *crossed circles* and *solid circles* correspond to $\nu = -1$, $\nu = +1$ semiconducting, and $\nu = 0$ metallic nanotubes, respectively. From [111]

of the nanotubes. *Kürti* et al. [36] observed that, in addition to a softening for smaller nanotubes, there is a dependence on chirality in the vibrational frequencies calculated ab initio. Again, armchair tubes are almost unaffected, even for quite small diameters. Alternatively, continuum mechanics becomes worse as an approximation, and the chirality of a nanotube should become more noticeable for very small nanotubes. For nanotubes around 1 nm the differences are small, but for even smaller tubes there is a systematic deviation, stronger for zigzag tubes, as expected.

Jorio et al. [111] did a systematic experimental study of the ω_{RBM} of small nanotubes. Their results are shown in Figs. 11a and b where the frequency deviations $\Delta\omega_{RBM}$, compared to (5), are plotted as a function of diameter

and chiral angle. There appear to be systematic deviations as a function of diameter for metallic tubes (closed circles) and the two semiconducting families (crossed and open circles in Fig. 11a). If we assume that the positive offset of the armchair tubes is an artifact of the fit and shift down the zero in Fig. 11a by, say, $2 \, \text{cm}^{-1}$, the agreement of the data to the theory of [36] turns out rather well.

The data in Fig. 11b show a systematic increase of $\Delta\omega_{\text{RBM}}$ as a function of chiral angle Θ. Again, compared to the results of Kürti et al., who showed that on an absolute scale armchair tubes (large chiral angles) tend to follow the simple $1/d$ law, the data of Fig. 11b appear centered around their mean value at $\Theta \approx 15°$. Shifting them down by about $2 \, \text{cm}^{-1}$ to make their armchair shift zero shows that zigzag tubes deviate by about $3 \, \text{cm}^{-1}$ to $4 \, \text{cm}^{-1}$ from the $1/d$ expression. Thus, there is a good agreement between theory and experiment.

It is possible to parametrize the deviations from the simple $1/d$ form to include the effect of the threefold symmetry of the band structure [111]:

$$\omega_{\text{RBM}} = \frac{A}{d} + B + \frac{C + D(\cos 3\Theta)^2}{d^2} \, . \tag{9}$$

Equation (9) was used in Fig. 11c providing a much better description of the data than a or b. However, the need to do this parametrization separately for metallic and semiconducting nanotubes limits somewhat the use of expression (9) with eight parameters. We list them in Table 6; for their discussion, see [111].

Table 6. Parameters for metallic and semiconducting nanotubes used in (9). These parameters describe the frequency of the radial-breathing mode in carbon nanotubes. From [111]

	A (cm^{-1} nm)	B (cm^{-1})	C (cm^{-1} nm)	D (cm^{-1})
Semicond.	227	7.3 ± 0.3	-1.1 ± 0.3	-0.9 ± 0.2
Metallic	227	11.8 ± 1.0	-2.7 ± 1.2	-2.7 ± 0.8

3.2.2 Double-Walled Nanotubes

The radial-breathing modes of double-walled nanotubes are interesting as well. The eigenmodes of the inner and outer tubes combine into inphase and out-of-phase modes in the double-walled tube, and their coupling is described best by the graphite interlayer coupling strength. *Popov* and *Henrard* showed using a valence-force field model that the coupled radial modes both increase in frequency compared to the same tube in single-walled form (see Fig. 12 [112]).
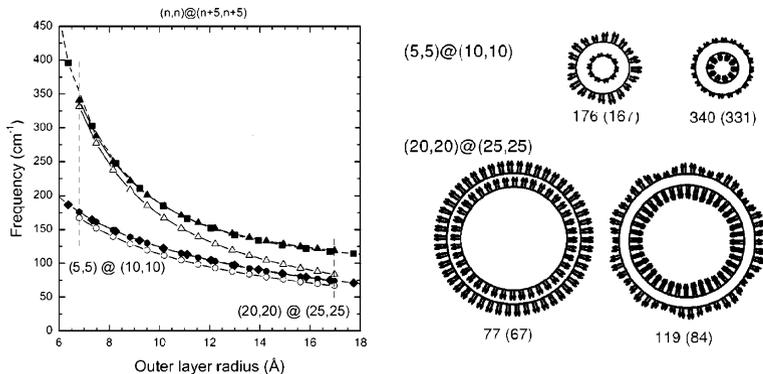
Fig. 12. (**left**) Frequencies of coupled radial-breathing modes in double-walled nanotubes. *Open symbols* belong to uncoupled tubes of the same diameter, *solid symbols* to double-walled nanotubes. The coupled frequencies are always higher than the uncoupled ones. (**right**) Eigenvectors and eigenfrequencies (in cm^{-1}) of the radial-breathing mode of two different diameters double-walled tubes. Inphase and corresponding out-of-phase modes are seen. After [112]

A simplified view of the coupled radial vibrations may be obtained by considering inner and outer tube oscillators connected by a spring. The inner and outer tubes have a diameter difference of 3.44 Å, the interplane spacing of graphite, and hence different eigenfrequencies $\omega_i = \sqrt{k_i/m_i}$, as given by (8). From the solution of the coupled-oscillator equations

$$m_1\ddot{x}_1 = -k_1 x_1 - k(x_1 - x_2) \quad \text{and}$$
$$m_2\ddot{x}_2 = -k_2 x_2 - k(x_2 - x_1). \tag{10}$$

Dobardžić et al. [113] obtained the same dependence of inner and outer frequencies on diameter as [112]. In addition, the analytical solution to (10) yields the relative phases of inner and outer displacements and allows an approximate expression for the shift of both upper and lower modes:

$$\Delta\omega_{\mathrm{RBM}} \approx \frac{\kappa' d_i}{2cc_1} \quad \text{for} \quad d_i \leq 7\,\text{Å}, \tag{11}$$

where $\kappa' = 115\,927\,\mathrm{u \cdot cm^{-2} \cdot \mathring{A}^{-1}}$ is the effective spring constant between inner and outer shell, d_i is the diameter of the inner shell, $c = 14.375\,\mathrm{u \cdot \mathring{A}^{-1}}$ is the linear mass density of a carbon nanotube, and c_1 is defined in (5). Note that the constant κ' is determined by the limiting case $d \to \infty$, where the out-of-phase mode becomes the interlayer mode of graphite [113]. For the diameters typically involved in the investigation of double-walled tubes, (11) is a useful expression for estimating the RBM frequencies. For further work based on this model, see [114].

Experimentally, the modes of double-walled tubes have not been conclusively identified. The measurements reported in [115, 116] have to be re-
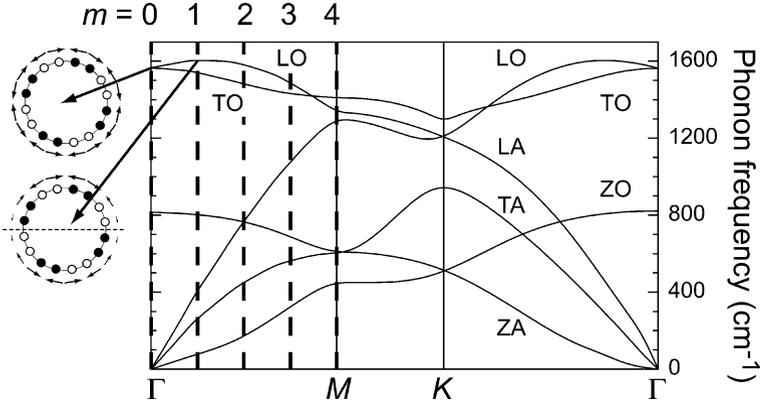
Fig. 13. Phonon dispersion of graphite and Γ-point vibrations of a (4,4) nanotube by zone folding. The nanotube contains several graphene unit cells around the circumference. Traveling waves of graphite that fulfill the periodic boundary conditions around the tube circumference are Γ-point vibrations of the nanotube (*dashed lines*). m labels the eigenvalues and is related to the z component of the angular momentum of a mode. Eigenvectors from the mth line have $2m$ nodes around the circumference, see the two circumferential eigenvectors for examples. The two eigenvectors are the A_{1g} (*upper*) and E_{1u} (*lower*) circumferential modes of the (4,4) nanotube. The tube cross section is schematically shown by the *large open circle* with the carbon atoms at $0 \cdot a$ (*closed symbols*) and $1/2 \cdot a$ (*open*) arranged around the circumference. The *arrows* next to the atoms indicate their displacement. The horizontal *dashed line* marks the nodal plane (zero displacement) of the lower $m = 1$ eigenvector. Data from [3]

evaluated in view of recent resonant Raman studies [63]. *Bacsa* et al. [47] identified several pairs of RBM peaks in tubes grown by a catalytic chemical vapor deposition (CVD) method. However, in their analysis they neglected the intertube interaction, i.e., they assumed $\Delta\omega_{\mathrm{RBM}} = 0$ in (11).

3.3 Tangential Modes

Tangential modes refer to all phonon bands of a nanotube originating from the optical phonons of graphite. Their eigenvectors are characterized by an out-of-phase displacement of two neighboring carbon atoms. The displacement is directed parallel to the nanotube wall, along the circumference, the axis, or a direction in between. The tangential modes involve predominantly the sp^2 inplane carbon–carbon bonds, which are extremely strong, even stronger than in the sp^3 diamond bond. Therefore, these modes have very high frequencies lying between $1100\,\mathrm{cm}^{-1}$ and $1600\,\mathrm{cm}^{-1}$ [20]. The Raman-active vibrations of the tangential modes fall into two groups, the high-energy modes (HEM) just below $1600\,\mathrm{cm}^{-1}$ and the D mode $\approx 1350\,\mathrm{cm}^{-1}$. The HEM is also called the G line in the nanotube literature; the "G" originally stood for

Table 7. Raman-active tangential modes. These phonons originate from the LO and TO branches of graphene; neighboring carbon atoms move out of phase. "circumferential" means parallel to the tube cirumference or chiral vector c; "axial", parallel to the nanotube axis or its unit cell vector a. In armchair and zigzag tubes there is only one phonon per irreducible resprensentation, in chiral tubes there are two. The subscript g holds for achiral tubes. All Raman-active eigenvectors of archiral tubes can be found in [20]

	$A_{1(g)}$	$E_{1(g)}$	$E_{2(g)}$
$|q_m|$	0	$2/d$	$4/d$
(n, n) armchair	circumferential	axial	circumferential
$(n, 0)$ zigzag	axial	cirumferential	axial
(n_1, n_2) chiral	mixed (2 modes)	mixed (2modes)	mixed (2modes)

graphite and was taken over from the graphite Raman spectrum to carbon nanotubes.

The theoretical phonon dispersion of the tangential modes and their eigenvectors can be derived from the graphite phonon dispersion [8,20,23,117–119] using the concept of zone folding, which we explain in more detail in Sect. 4.1. The general idea is shown in Fig. 13 for a (4,4) armchair tube. In such small tubes, zone folding is not very accurate for the phonon frequencies on an absolute scale, but it helps to understand the systematics in the tangential modes.

The unit cell of a nanotube contains many more carbon atoms than that of graphene, but they are built from the same lattice. Hence we expect similar phonon frequencies in the two materials. The main difference between graphene and a tube is that a number of traveling waves in graphene ($q \neq 0$) correspond to the Γ point of the tube ($q = 0$). More precisely, the wave with a wavelength $\lambda_m = \pi d/m$ fulfills the periodic boundary conditions around the tube (m integer, see also Sect. 4.1). In an (n, n) armchair tube, several graphene unit cells are joined across the corners of the hexagons ($a_1 + a_2$ direction) to the nanotube unit cell. A wave with wavelength λ_m and traveling along the ΓM direction of graphene thus corresponds to the Γ point of the tube. This is shown in Fig. 13; the dashed lines indicate k vectors that are folded onto the Γ point of the (4,4) nanotube.

The Γ point of graphene gives rise to nanotube phonon eigenvectors with a constant displacement around the circumference, see the circumferential A_{1g} eigenvector in Fig. 13. These modes are always nondegenerate (A or B modes). There is a second tangential mode coming from the Γ-point optical mode of graphene. It is axial and Raman inactive in armchair tubes. Phonons with $m = 1, 2, \ldots, (n - 1)$ are doubly degenerate E modes. They have $2m$ nodes in their phonon displacements when going around the tube's circumference. The circumferential E_{1u} phonon in Fig. 13 has two nodes (dashed horizontal line) and is infrared active. Note that this phonon is higher
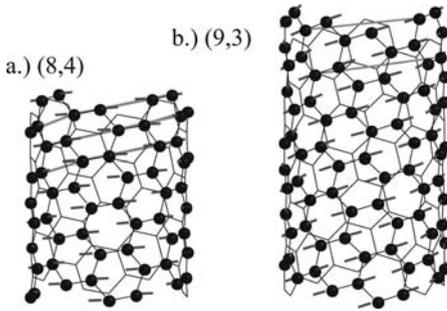
Fig. 14. (**a**) A_1 high-energy eigenvector of an (8,4) nanotube calculated from first principles. The atomic displacement is parallel to the circumference. (**b**) A_1 high-energy eigenvector of a (9,3) tube. The displacement is parallel to the carbon–carbon bonds. The direction of the helix in both tubes, obtained from the screw-axis operation, is indicated by the *gray lines*. From [20]

in frequency than the A_{1g} mode discussed previously. This comes from the overbending of the graphene LO branches (overbending means that the highest phonon frequency occurs inside the Brillouin zone, not at the Γ point, as in most materials; other examples of this phenomena besides graphite are diamond [120, 121] and hexagonal boron nitride [122, 123]). Phonons from the $m = 1$ and 2 line can be Raman active, see Table 7. Finally, phonons with $m = n$ originate from the M point of graphene. They are nondegenerate as are the modes originating from the graphene Γ point. These phonons are infrared- and Raman-inactive in all carbon nanotubes [20, 81].

To find the Γ-point vibrations of an $(n, 0)$ zigzag tube we need to divide the ΓKM direction in Fig. 13 into n segments. The degeneracy and the number of tangential high-energy modes follow as for armchair tubes. The Raman activity is reversed, see Table 7. An axial phonon that is Raman active in an armchair tube is inactive in a zigzag tube and vice versa [38, 81, 103].

In chiral tubes the chiral vector is along a low-symmetry direction of graphene. Then, also the confinement direction is a low-symmetry direction in reciprocal space. Once again, the degeneracy of the modes is the same as in armchair tubes (nondegenerate for $m = 0, q$, twofold degenerate for all other m and $2m$ nodes around the circumference). Because of the low symmetry of the tubes, the phonons are no longer axial and circumferential by symmetry [38, 124]. Examples are the A_1 eigenvectors of an (8,4) and a (9,3) tube in Fig. 14. Moreover, both A_1 ($m = 0$) phonons are Raman active. Their relative intensity depends on the chiral vector of the tube and the displacement direction of the eigenvector. For a nanotube with large Θ (close to armchair), the circumferential mode is expected to dominate, for a tube with small Θ (close to zigzag) the axial mode dominates.

Zone folding is a first approximation to the phonon frequencies of the high-energy tangential modes. As can be seen in Fig. 13 it predicts the axial

Table 8. Labeling used for the displacement direction (displ.) of the high-energy modes. tube: displacement direction is given as circumferential/axial; confinement: classification as LO/TO with respect to the confinement direction (tube circumference); propagation: classification as LO/TO with respect to the propagation direction (tube axes). symmetry: representation of the $m = 0$ mode in armchair (AC), zigzag (ZZ) and chiral (CH) tubes; graph.: graphene phonon branch from which a mode originates in the zone-folding scheme; overb. in tube indicates whether the $m = 0$ nanotube branches have an overbending or not. Selected references are given for each convention

Displ.	Symmetry	Graph.	Overb. in tube [38, 129, 130]	Tube [8, 38, 117]	Confinement [126, 131, 132] [118, 128]	Propagation
$\|\boldsymbol{c}$	A_{1g}(AC) A_{1u}(ZZ) A_1(CH)	LO	no	circumfer.	LO-like, LO$_m$	TO, T[a]
$\|\boldsymbol{a}$	A_{1u}(AC) A_{1g}(ZZ) A_1(CH)	TO	yes	axial	TO-like, TO$_m$	LO, L

[a] [133] The modes with a displacement along the nanotube circumference are called "axial" (A) in [118]; for the displacement along the tube axis "longitudinal" (L) is used in both [133] and [118]

and circumferential $m = 0$ eigenvector of a (4,4) tube to be degenerate, because they both arise from the doubly degenerate E_{2g} optical phonon of graphene (see [125] for a review of the lattice dynamics of graphite). There are two reasons why this is not the case for carbon nanotubes: curvature and, in the case of metallic tubes, the Kohn anomaly [3, 8, 38, 117, 118, 126–128].

Curvature softens the force constant in both semiconducting and metallic tubes. In Sect. 3.2 we discussed how the bonds along the nanotube circumference get an sp^3 component with decreasing diameter. Since the optical phonon of diamond is at a lower frequency ($1332\,\mathrm{cm}^{-1}$) than that of graphite ($1589\,\mathrm{cm}^{-1}$), curvature shifts the circumferential vibrations to lower frequencies. The axial vibrations are much less affected, see [8] and [118].

The Kohn anomaly affects the phonons in metallic tubes (see below). It strongly reduces the frequency of the axial A_1 mode. Before discussing this, we consider briefly the terms axial and circumferential versus transversal and longitudinal vibrations in connection with carbon nanotubes. These terms are used in a somewhat confusing way in the literature and are frequently intermixed.

We already pointed out that the tangential vibrations are, in general, of mixed axial and circumferential character in chiral carbon nanotubes [38], because of the mechanical boundary conditions and the low-symmetry con-

finement direction. Most of the theory of lattice dynamics, however, was developed for armchair and zigzag tubes. In achiral tubes the tangential modes have a definite parity and displacement direction with respect to the tube axis. Therefore, classifications of the tangential modes as axial/circumferential, LO/TO, and LO-like/TO-like are often used; see Table 8. The main confusion with the terms transverse and longitudinal arises because they can be referred to the confinement direction – as is normally done for low-dimensional systems [98, 134] – or with respect to the propagation direction – as is the standard convention for three-dimensional systems.

Take, for example, the two eigenvectors in Fig. 13. These circumferential vibrations should be called LO-like when referred to the confinement direction (the circumference), but TOs when referred to the only possible propagation direction, the z-axis of the nanotube. Labeling them as TOs leads to the result that the highest TO vibrations are higher in frequency than the LOs. Referring to the eigenvectors with respect to the confinement direction as LO-like or LO_0 and LO_1 in Fig. 13, on the other hand, we find that the nanotube LO modes have no overbending, whereas the TO modes do, see Table 8. While the "folded" nanotube Γ-point modes are higher in frequency than the $m = 0$ Γ-point mode due to overbending of the graphene LO mode, their propagation direction is perpendicular to the confinement direction, where the phonon dispersion has no overbending. This might lead to confusion compared to graphene, where the LO branches show a strong overbending. For these reasons we use the terms axial and circumferential in this work; they indicate the atomic displacement direction without making direct reference to the confinement or propagation direction of a phonon.

In armchair nanotubes, the valence and conduction bands cross at $\approx 2\pi/3a$. These tubes are always metallic and have a Fermi surface that is a single point, see Sect. 4. Chiral and zigzag tubes are metallic within the zone-folding approximation (neglecting curvature) if $(n_1 - n_2)/3$ is an integer. When curvature is included, these tubes have a small secondary gap at the Fermi level, on the order of $10\,\mathrm{meV}$ [6, 135–137] and are called quasimetallic tubes. A phonon that couples to the electronic states at the Fermi level opens a gap in armchair tubes and strongly modulates the gap in quasimetallic tubes [133]. This coupling reduces the total energy of the distorted system (nanotube plus phonon) and hence softens the force constants. One then finds in the phonon dispersion of the material a singular behavior for certain q vectors and phonon branches, referred to as a Kohn anomaly [138, 139].

In graphite and single-walled carbon nanotubes, a Kohn anomaly occurs at the Γ and the K point or at $2\pi/3a_0$ for the tubes[4] [3, 127, 140–142]. It reduces the Γ-point frequency of the axial high-energy vibration in metallic tubes. The softening by the electron–phonon coupling is larger than the curvature-induced softening [133]. Therefore, the axial $m = 0$ vibration of

---

[4] The Kohn anomaly at $q = 0$ originates from the special Fermi surface of graphene and nanotubes, which are single points. We will explain this in Sect. 9.3.
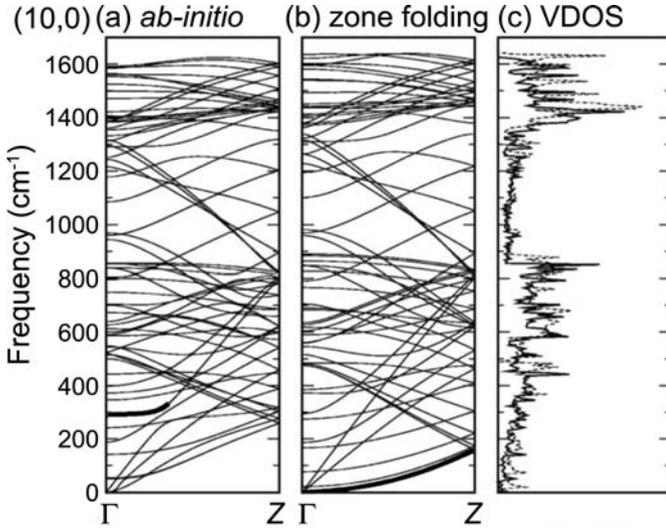
Fig. 15. Phonon dispersion of a (10,0) nanotube from (**a**) first principles and (**b**) zone folding of the graphene phonon dispersion. (**c**) Vibrational density of states from first principles (*full line*) and zone folding (*dashed*). From [118]

metallic nanotubes is lower in frequency than the circumferential phonon. This is opposite to semiconducting tubes, for which no Kohn anomaly occurs, but the circumferential phonon still feels the curvature of the nanotube wall.

We can obtain a good approximation for the phonon dispersion using zone folding. This works best for semiconducting tubes (no Kohn anomaly) with diameters $d \gtrsim 1\,\mathrm{nm}$ (little curvature effects). As an example, we compare the ab-initio phonon dispersion of a semiconducting (10,0) tube in Fig. 15a with the zone-folding approximation in Fig. 15b. In the low-energy range, zone folding fails to predict the radial-breathing mode (thick line at $300\,\mathrm{cm^{-1}}$ in Fig. 15a) [8,133,143]. This totally symmetric phonon has no simple equivalent among the Γ-point vibrations of graphene (upon zone folding $A_{1(g)}$ totally symmetric modes must originate from the graphene Γ point, see [20, 103]). Instead, the radial-breathing mode corresponds to an inplane uniaxial stress along the chiral vector [144].

Other low-energy vibrations typically show a frequency change when comparing Figs. 15a and b. This is mainly a curvature effect due to the rather small diameter of the (10,0) tube [9]. Another interesting difference is the parabolic acoustic dispersion upon zone folding shown by the thick line in Fig. 15b originating from the out-of-plane acoustic (ZA) branch of graphene (see Fig. 13). Because of the cylindrical geometry of the tube this peculiar dispersion disappears.
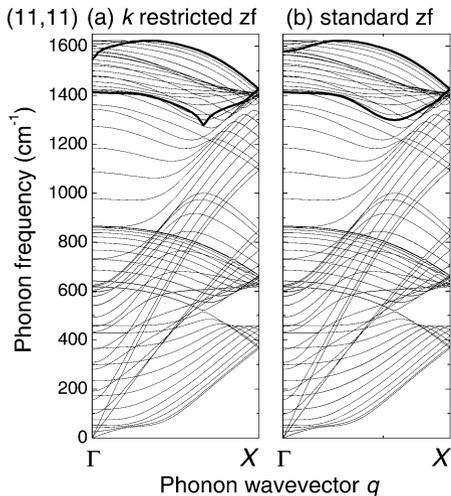
Fig. 16. Phonon dispersion of an (11,11) nanotube. (**a**) Calculated using linear response (ab-initio calculation) by restricting the *electronic* wavevectors to the allowed wavevectors of an (11,11) tube. This is an unconventional zone folding scheme, which takes into account the one-dimensional character of the tube, but neglects curvature. (**b**) Conventional zone folding of the graphene phonon dispersion obtained by restricting the *vibrational* states to the allowed wavevectors of the tube. In the one-dimensional nanotube Kohn anomalies are stronger (see *bold lines* in (**a**)) than in graphene (*bold lines* in (**b**)). From [141]

Zone folding is a better approximation for the high-energy tangential modes than for the low-energy vibrations. We can see some curvature induced effects in Fig. 15, for example, the softening of the highest-frequency vibrations in Fig. 15a compared to Fig. 15b. As discussed above, the highest phonons branches in carbon nanotubes are always circumferential because of the overbending in graphene. Circumferential modes soften due to curvature, a fact that explains the high-energy part of the phonon dispersion. This is also seen in the vibrational density of states (Fig. 15c). The softening of the vibrational DOS has been measured by two-phonon Raman scattering, see Sect. 10.3 and [145].

Figure 16 shows phonon-dispersion curves for a metallic (11,11) armachair tube [141]. Both dispersions were obtained by a zone-folding approach. Figure 16a represents an ab-initio calculation of graphene, where the calculated points in reciprocal space were restricted to the allowed $\boldsymbol{k}$ vectors of a (11,11) tube. Using this restricted Hamiltonian, the phonon bands were obtained from linear response theory [141]. This *unconventional zone folding* takes into account the one-dimensional character of carbon nanotubes, but not their curvature (for the (11,11) tube with $d = 1.5$ nm curvature effects are small [9]). The dispersion in Fig. 16b corresponds to standard zone folding,
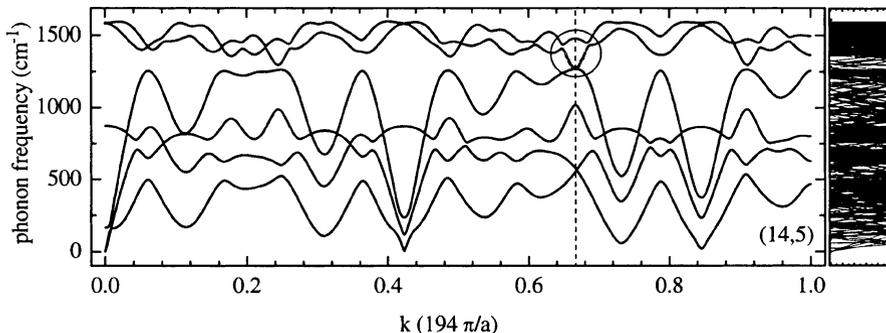
Fig. 17. Phonon dispersion of a (14,5) nanotube. **Left**: Dispersion as a function of the helical wavevector $\tilde{k}$. **Right**: Dispersion as a function of the linear wavevector k as in Figs. 15 and 16. The unit cell is very small in this chiral tube because the axial lattice vector $a = 29.5a_0$. From [85]

i.e., the graphene phonon dispersion was calculated from first principles and then used for finding the dispersion of the (11,11) tube (see Sect. 4.1 or [20]).

The axial $m = 0$ phonon band in Fig. 16a (thick line) drops sharply in frequency when approaching the Γ point [127, 140, 141, 146]. The phonon dispersion has a singularity at Γ, which reflects the Kohn anomaly of metallic nanotubes introduced above. The Γ-point axial frequency – A_{1u} symmetry – is at $1547 \, \text{cm}^{-1}$ as opposed to $1579 \, \text{cm}^{-1}$ in standard zone folding in Fig. 16b. A second singularity occurs for the back-folded $\Gamma K M$ branch at $2\pi/3a$ ($m = n$ phonon of the (11,11) tube). This corresponds to the K point of graphene, see Sect. 4.1. Graphene also has Kohn anomalies at Γ and K [3, 127]. These two wavevectors couple electrons at the Fermi level. The Kohn anomalies are more pronounced in metallic nanotubes than in graphene, because of the one-dimensional character of the tubes [140–142].

In Fig. 16a only one phonon branch shows a singular behavior at Γ and K, respectively. Besides the correct q, a phonon also needs the correct symmetry to mediate an interaction between electrons. We discuss this topic in more detail in Sects. 8 and 9.3.

Carbon nanotubes have a large number of vibrational degrees of freedom and hence phonon bands. Figures 15 and 16 correspond to achiral tubes, where the number of atoms in the unit cell is small compared to the chiral species of similar diameter. In the right panel of Fig. 17 we show as a final example the dispersion of a (14,5) nanotube. The number of phonon bands in this case is 1164 [85]. A more transparent dispersion is obtained when using the so-called helical quantum numbers [85, 136]. In the left panel of Fig. 17 we show the phonon dispersion of the (14,5) as a function of the helical momentum instead of the linear momentum in the right panel. Details can be found in [20, 86, 136].

Out of the hundreds or thousands of phonon branches only a tiny fraction is Raman active (8 in achiral and 15 in chiral tubes, see Sect. 3.1). Moreover, the Raman spectra are dominated by totally symmetric phonons, see Sect. 6.4 [99, 101, 147]. Thus, only three branches are easily accessible experimentally, the radial-breathing mode and in the high-energy range the $m = 0$ tangential vibrations. Additionally, the K-point phonon of graphene gives rise to the D mode in the Raman spectra of nanotubes. The other vibrations are either very low in intensity or not observed at all. In the remainder of this work we mainly discuss the totally symmetric vibrations and the D mode, their overtones, resonances, and the corresponding electron–phonon coupling.

4 Electronic Properties

Single-walled carbon nanotubes are metals or semiconductors depending on their chirality. From the chiral index plot in Fig. 3 we see that every metallic tube (squares) is surrounded by six semiconducting neighbors (open and closed circles). Very subtle changes in the microscopic structure, e.g., a (10,5) and a (10,6) tube are almost indistinguishable concerning their atomic structure, result in drastic changes in the electronic properties. This is one of the reasons why carbon nanotubes evolved into a model system for one-dimensional nanostructures. They are a prime example of structure and shape being as important as, or even more than, chemical composition for very small systems.

A detailed review of the electronic and optical properties of carbon nanotubes is beyond the scope of this Chapter. Instead we introduce in this section the main concepts used for describing their physical properties: zone folding, family and branch behavior. We then concentrate on the optical range (visible and infrared transition energies) and exciton formation in nanotubes. This field has developed very rapidly over the last two years, after the first report of photoluminescence from carbon nanotubes [59, 60].

4.1 Zone Folding

Single-walled carbon nanotubes are one-dimensional solids [20]. Along the nanotube circumference electrons, phonons and other quasiparticles can only have certain, discrete wavelengths, because of the periodic boundary conditions [6, 20, 23, 83, 148–151]. On the other hand, quasiparticles can travel along the nanotube axis. An infinitely long tube has continuous electronic and vibrational states in this direction.

In the following we show how the quantization condition can be used to estimate the electronic band structure of carbon nanotubes from the electronic states of graphene. We do this by restricting the graphene eigenstates
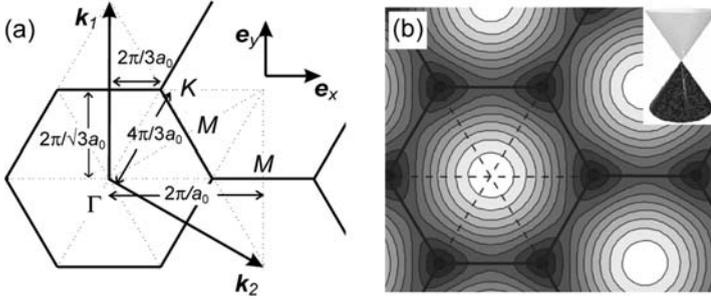
Fig. 18. (**a**) Hexagonal Brillouin zone of graphene. The reciprocal lattice vectors in terms of a Cartesian coordinate system are given by $\boldsymbol{k}_1 = 4\pi/\sqrt{3}a_0(1,0)$ and $\boldsymbol{k}_2 = 4\pi/\sqrt{3}a_0(\sqrt{3}/2, 1/2)$; their length is $4\pi/\sqrt{3}a_0$. The figure shows the high-symmetry Γ, M and K points. (**b**) Same as (**a**) but with a contour plot of the electronic band structure of graphene. Eigenstates at the Fermi level are shown in *black*; *white* marks energies far away from the Fermi level. The *inset* shows the valence (*dark*) and conduction (*bright*) band around the K points of the Brillouin zone. The two bands touch at a single point (K). After [20]

to the allowed wavevectors of a tube. We now introduce briefly the electronic properties of graphene.

Graphene is a semimetal. This means that its valence and conduction bands cross, but the electronic density of states is zero at the Fermi level (the crossing point). The most widely used description of the electronic band structure of graphene is an empirical tight-binding model [5, 6, 20, 23]. This model includes only the π states perpendicular to the graphene sheet and their interactions, because these states give rise to the electronic bands close to the Fermi level. We restrict the interaction between the carbon electrons to nearest neighbors in the graphene sheet and neglect the overlap between two π wavefunctions centered at different atoms. Under these approximations the valence E^- and conduction bands E^+ of graphene are given by the simple analytic expression [5, 20, 23]

$$E^{\pm}(\boldsymbol{k}) = \gamma_0 \sqrt{3 + 2\cos \boldsymbol{k} \cdot \boldsymbol{a}_1 + 2\cos \boldsymbol{k} \cdot \boldsymbol{a}_2 + 2\cos \boldsymbol{k} \cdot (\boldsymbol{a}_1 - \boldsymbol{a}_2)}. \qquad (12)$$

γ_0 describes the interactions between two π electrons; typical values range from 2.7 eV to 3.1 eV. $\boldsymbol{k}$ is the electronic wavevector (see Fig. 18a) for the graphene Brillouin zone, and $\boldsymbol{a}_1$ and $\boldsymbol{a}_2$ are the lattice vectors.

The nearest-neighbor tight-binding model of (12) describes well the electrons close to the Fermi energy (within $\sim$ 0.2 eV of E_F). In the range of optical-transition energies, however, it deviates by 0.5 eV to 1 eV from ab-initio calculations and from measurements [6]. This can be fixed by including more neighbors; if up to third-neighbor interaction and the overlap between the π wavefunctions are included, there is virtually no difference between the semiempirical description and first-principles results. A discussion of the
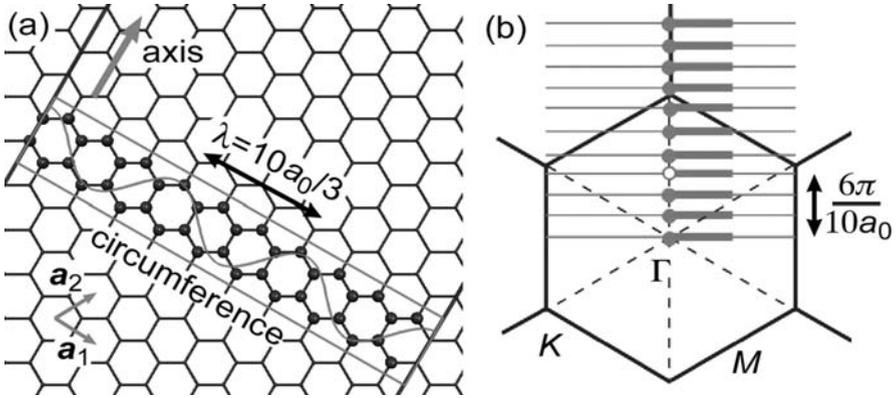
Fig. 19. Quantized wavevectors and zone folding of graphite. (**a**) a (10,0) nanotube unwrapped to a graphene sheet. The atoms shown are those inside the unit cell of the tube. The *gray line* is a wave with wavelength $\lambda = 10a_0/3$, which corresponds to an allowed state of the nanotube. (**b**) Allowed, discrete wavevectors of a (10,0) tube shown in the Brillouin zone of graphene. The wave in (**a**) corresponds to the *open circle* in (**b**). The *thick lines* form the one-dimensional Brillouin zone of the (10,0) tube

level of approximation and the derivation of (12) as well as a corresponding analytic expression for larger interaction ranges can be found in [6, 20].

Figure 18b shows a contour plot of the electronic band structure of graphene. For the π^* conduction band the electronic energies range from 12.2 eV at Γ to zero at the K point of the Brillouin zone; the π valence band varies between -8.8 eV and the Fermi level. The two Γ-point energies are from experiment [20, 152]. To obtain nonsymmetric π and π^* bands within the tight-binding approximation we need to consider the finite overlap between electrons at different atoms or include more neighbors [5, 9, 20, 23]. Close to the six K points, where valence and conduction bands touch at a single point, the two bands are linear with k to a very good approximation. The inset of Fig. 18b shows the cones that represent the band structure very close to the Fermi energy.

Having obtained the electronic band structure of graphene, how can we use it to obtain the band structure of single-walled carbon nanotubes? Consider quantization in a (10,0) nanotube. An allowed wave for this tube is shown in Fig. 19a. It has three nodes along the circumference or a wavelength $\lambda = 10a_0/3$. For graphene this corresponds to wavevectors away from the Γ point of the hexagonal Brillouin zone (see Fig. 18a). The quantization condition for an (n_1, n_2) nanotube in reciprocal space can be derived from its chiral vector $\boldsymbol{c}$ and the axial lattice vector $\boldsymbol{a}$. The general expressions are given in Table 1.

For a (10,0) zigzag tube we find

$$\boldsymbol{k}_\perp \overset{(n,0)}{=} \frac{\boldsymbol{k}_1}{n} + \frac{\boldsymbol{k}_2}{2n} \overset{(10,0)}{=} \frac{\boldsymbol{k}_1}{10} + \frac{\boldsymbol{k}_2}{20}, \tag{13}$$

i.e., when starting from the Γ point and going along ΓKM ($\boldsymbol{k}_1 + \boldsymbol{k}_2/2$, see Fig. 18a) we find 10 equally spaced points that are allowed. All these points correspond to the Γ point of the (10,0) nanotube. They are shown as circles in Fig. 19b. The forth circle (open) represents the wave in Fig. 19a in reciprocal space. The distance between two allowed points, $2\pi/10a_0$ for the (10,0) tube, is given by the nanotube diameter $|\boldsymbol{k}_\perp| = 2/d$.

The reciprocal lattice vector along the nanotube axis is $\boldsymbol{k}_z = \boldsymbol{k}_2/2$ for the (10,0) and any other zigzag tube. The nanotube Brillouin zone is thus built as shown in Fig. 19b: The quantized circumferential vectors (circles) correspond to the Γ point of the tube (Γ_{nt}). Perpendicular to the quantization direction the allowed states are continuous. For the special case of zigzag tubes the general expression for allowed wavevectors (see Table 1) reduces to [20]

$$\boldsymbol{k}_{zz} = \frac{m}{n}\boldsymbol{k}_1 + \left(\frac{m}{2n} + \frac{k_z}{2}\right)\boldsymbol{k}_2 \ \ \text{with } m = -(n-1)\ldots n; k_z = 0\ldots 0.5. \tag{14}$$

m (the z component of the angular momentum of a particle) indexes the bands of a nanotube. k_z is the magnitude of the axial wavevector in units of the reciprocal lattice vector. Inserting the allowed wavevectors in (12) we obtain the electronic band structure of zigzag carbon nanotubes within the tight-binding zone-folding approximation

$$E_{zz}^\pm(m, k_z) = \gamma_0\sqrt{3 + 2\cos 2\pi\frac{m}{n} + 4\cos\pi\frac{m}{n}\cdot\cos\pi k_z}\,. \tag{15}$$

The corresponding expression for armchair tubes is

$$E_{\mathrm{ac}}^\pm(m, k_z) = \gamma_0\sqrt{3 + 4\cos\pi\frac{m}{n}\cdot\cos\pi k_z + 2\cos 2\pi k_z}\,. \tag{16}$$

For armchair as for zigzag tubes, the quantum number m satisfies $-(n-1) \leq m \leq n$. Finally, the band structure for a chiral (n_1, n_2) nanotube within the nearest-neighbor tight-binding model is given by

$$\begin{aligned}
E_{\mathrm{c}}^\pm(m, k_z) = \gamma_0\bigg[3 &+ 2\cos\left(m\frac{2n_1 + n_2}{qn\mathcal{R}} - \frac{n_2}{q}k_z\right) \\
&+ 2\cos\left(m\frac{2n_2 + n_1}{nq\mathcal{R}} + \frac{n_1}{q}k_z\right) \\
&+ 2\cos\left(m\frac{n_1 - n_2}{qn\mathcal{R}} - \frac{n_1 + n_2}{q}k_z\right)\bigg]^{1/2},
\end{aligned} \tag{17}$$
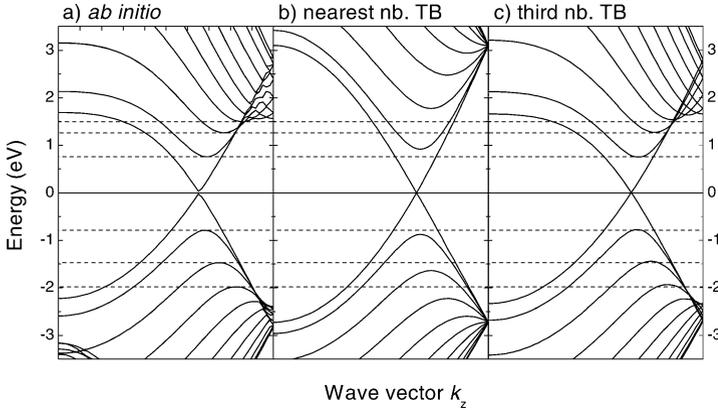
Fig. 20. Band structure of a (10,10) armchair nanotube with diameter $d = 1.4\,\text{nm}$. (**a**) Ab-initio calculation; (**b**) nearest-neighbor tight-binding calculation with $\gamma_0 = -2.7$ eV [(16) with $n = 10$]; (**c**) third-nearest neighbors tight-binding calculation. The *dashed lines* denote ab-initio calculated energies of the band extrema. The agreement of the energies in (**a**) and (**c**) is excellent. From [6]

where m is an integer running from $-(q/2 - 1)$ to $q/2$ [81]; see Table 1 for q, n and $\mathcal{R}$ as a function of n_1 and n_2.

The quantum number m is very useful to index bands and phonon branches and to derive selection rules, e.g., for Raman scattering, infrared vibronic and optical electronic absorption [20, 81, 83, 87]. The $m = 0$ electronic bands and phonon branches always contain the graphene Γ point (see Fig. 19b); $m = q/2$ ($= n$ for achiral tubes) is the M point of graphene for $k_z = 0$ [9]. These two bands are nondegenerate for any quasiparticle and any nanotube. In achiral tubes, all other bands are twofold degenerate in chiral tubes, none, see [20, 85, 86] for a discussion and examples.

4.2 Electronic Band Structure

Figures 20 and 21 show the electronic band structure of a (10,10) and (19,0) nanotube, respectively. Parts (a) in both figures are from first-principles calculations, while parts (b) were obtained with (16) and (15), and parts (c) are the results of the extended tight-binding model using up to third neighbors [6]. For all practical purposes, the extended tight-binding model is indistinguishable from the ab-initio calculations. The simple nearest-neighbors tight-binding scheme works reasonably well. There are certain systematics in Figs. 20 and 21 about which we will not comment in detail. For example, the band extrema are at the Γ point in the (19,0) tube, but at $2\pi/3a$ in the (10,10) tube. General rules for the overall shape of the band structure and the position of the band extrema as a function of n_1 and n_2 can be found in [20].
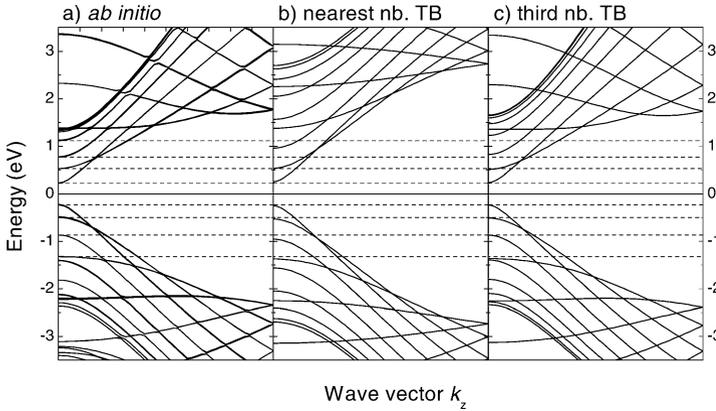
Fig. 21. Band structure of a (19,0) zigzag nanotube with a diameter of $d = 1.5$ nm. (**a**) Ab-initio calculation; (**b**) nearest-neighbor tight-binding calculation with $\gamma_0 = -2.7$ eV [(15) with $n = 19$]; (**c**) third-nearest neighbors tight-binding calculation. The *dashed lines* denote ab-initio calculated energies of the band extrema. From [6]
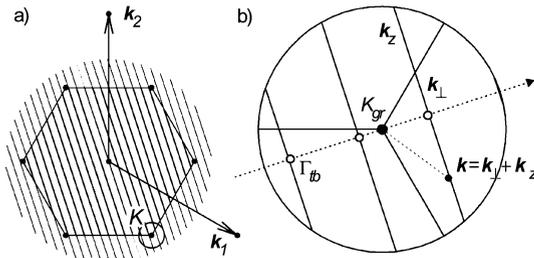
Fig. 22. (**a**) Allowed wavevectors of a nanotube in the Brillouin zone of graphene (see also Fig. 19). (**b**) Expanded view of the allowed wavevectors $\boldsymbol{k}$ around the K point. $\boldsymbol{k}_\perp$ is an allowed wavevector around the circumference of the tube; $\boldsymbol{k}_z$ is continuous. The *open dots* are points with $k_z = 0$; they all correspond to the Γ point of the tube. From [153]

As can be seen in Figs. 20 and 21 the (10,10) tube is metallic, whereas the (19,0) tube has a bandgap of 0.5 eV. The metallic and semiconducting character of the nanotubes can be explained by zone folding using the Fermi surface of graphene. In the last section we saw that the valence and conduction bands of graphene cross at the K point of the Brillouin zone. If the graphene K point is among the allowed states of a carbon nanotube, the tube is metallic. Otherwise, it is semiconducting with a moderate bandgap. To quantify this hand-waving argument let us consider an (n_1, n_2) nanotube. Figure 22a shows the quantized states of a general nanotube; the region around the K point is expanded in Fig. 22b. The electronic states are restricted to wavevectors that fulfill the condition $\boldsymbol{k} \cdot \boldsymbol{c} = 2\pi m$, where $\boldsymbol{c}$ is the

chiral vector of the tube and m is an integer. For the tube in Fig. 22 the K point is not allowed and the tube is a semiconductor. The K point of graphene is at $\frac{1}{3}(\boldsymbol{k}_1 - \boldsymbol{k}_2)$; thus, a nanotube is a metal if

$$\boldsymbol{K} \cdot \boldsymbol{c} = 2\pi m = \tfrac{1}{3}(\boldsymbol{k}_1 - \boldsymbol{k}_2)(n_1\boldsymbol{a}_1 + n_2\boldsymbol{a}_2) = \tfrac{2\pi}{3}(n_1 - n_2),$$

which implies

$$3m = n_1 - n_2. \tag{18}$$

This famous result, derived by *Hamada* et al. [148] and *Saito* et al. [149], means that a tube is a metal if $n_1 - n_2$ is a multiple of three.

We can now understand the pattern of metallic tubes in the chiral index plot in Fig. 3. (n, n) armchair nanotubes are always metallic, $(n, 0)$ zigzag tubes only if n is a multiple of three. The sets of metallic chiral indices parallel to the armchair-like directions arise, because for these sets $n_1 - n_2$ is either constant or changes by ± 3 from tube to tube. Take, for example, the (5,5) nanotube. Along the main armchair line (labeled armchair in Fig. 3) $n_1 - n_2$ is constant, since we change both n_1 and n_2 by the same amount, e.g., (5,5) to (6,6). Along the vertical direction n_1 decreases by 1 and n_2 increases by 2 when going from top to bottom, i.e., the difference between n_1 and n_2 changes by 3, such as for (5,5) to (6,3); similarly for the third armchair-like direction [(5,5) to (7,4)]. The same pattern is found for the open and closed symbols in Fig. 3. The reason is that metallic nanotubes are just a special case of the nanotube family, which we discuss in connection with the optical spectra of single-walled carbon nanotubes (Sect. 5.2).

The good agreement between first-principles and zone-folding calculations for the (10,10) and (19,0) nanotubes is also found for tubes with diameters ≥ 1.5 nm. For smaller-diameter tubes, the curvature of the nanotube wall can no longer be neglected. Curvature mixes the inplane σ and out-of-plane π states of graphene [9, 135]. It thereby shifts the electronic bands towards the Fermi level. Since this shift is larger for bands originating from the part between the K and the M point of the Brillouin zone than for bands from the part between Γ and K, curvature can change the order of the bands in single-walled nanotubes. It mainly affects the conduction bands and thus lifts the symmetry between the electron and the hole, which – to a very good approximation – is present in graphite, compare Figs. 20 and 21. For very small diameter nanotubes ($d \approx 0.5$ nm) the zone-folding picture fails completely [9, 10, 88, 135, 154–159]. For example, the (5,0) nanotube is metallic, although it is predicted to be semiconducting within the zone-folding approximation.

5 Optical Properties

The resonant Raman effect is intimately related to the optical properties of a material. Using Raman spectroscopy we can, therefore, study not only
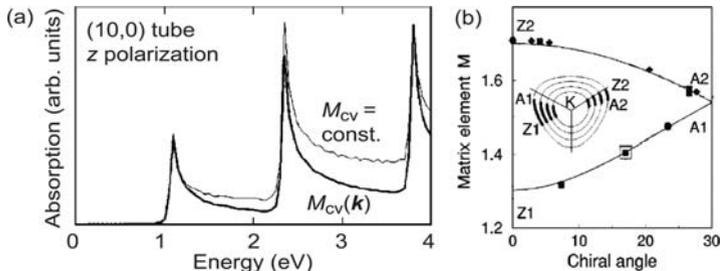
Fig. 23. (**a**) Band-to-band absorption spectra for a $(10,0)$ nanotube calculated within tight binding. Note the sharp van-Hove singularities, typical for one-dimensional systems. The *thin line* assumes the optical matrix elements to be independent of the axial wavevector of the tube k_z; the *thick line* includes the dependence of the optical transition elements on k_z. (**b**) Chirality and family dependence of the matrix elements. A2 to Z2 refers to transitions originating close to the KM line of the graphene Brillouin zone. A1 to Z1 correspond to states between Γ and K (see *inset*). After [162]

the vibrations of a molecule or solid, but their electronic excitations and the optical response. This adds greatly to the power of Raman scattering for investigating and characterizing materials.

Resonances arise when the incoming or outgoing photon in the Raman process matches an optical singularity of the system (Sect. 6). They can be very strong in one-dimensional structures, because the electronic density of states diverges at the band extrema. In the following, we discuss the optical properties of carbon nanotubes. We start by considering the joint density of states (JDOS) in band-to-band transitions and then turn to exciton formation, which is important for understanding the optical properties.

5.1 Band-to-Band Transitions

In a band-to-band transition a photon excites an electron from the valence into the conduction band. The interaction between the electron and the hole it leaves behind is neglected, in contrast to an exciton formed by an interacting electron and hole (see Sect. 5.3). Band-to-band transitions have not been observed in carbon nanotubes, because the exciton binding energy is large (0.1 eV to 1 eV, much larger than $k_B T$ at room temperature, k_B is the Boltzmann constant) [10,60,160,161]. We, nevertheless, discuss band-to-band transitions since they give a good insight into density-of-states arguments and the optical selection rules for carbon nanotubes. These arguments will remain valid when we later consider excitons.
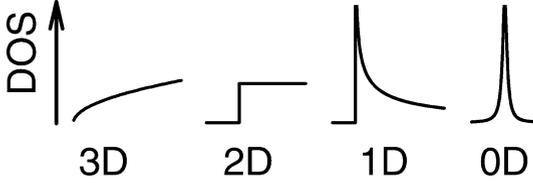
Fig. 24. Density of states in 3, 2, 1, and 0-dimensional systems. For one-dimensional systems the density of states follows a $1/\sqrt{E}$-behavior

In the dipole approximation the imaginary part of the dielectric function $\varepsilon_2(\omega)$ originating from band-to-band transitions is proportional to [134]

$$\varepsilon_2(\omega) = \frac{|M_{\mathrm{cv}}|^2}{\omega^2} \int \frac{dS_{\boldsymbol{k}}}{\nabla_{\boldsymbol{k}}(E_{\mathrm{c}}(\boldsymbol{k}) - E_{\mathrm{v}}(\boldsymbol{k}))} , \qquad (19)$$

where ω is the photon frequency and M_{cv} are optical matrix elements. The integral corresponds to the joint density of electronic states (JDOS) of the valence E_{v} and conduction band E_{c}. Regions in the electronic band structure with parallel bands thus contribute strongly to band-to-band absorption.

For simplicity we assumed that the optical matrix elements M_{cv} are independent of the axial wavevector [87, 154, 162]. Within one pair of electronic subbands this is, in fact, quite accurate. Figure 23a compares a calculated band-to-band absorption spectrum for k-independent matrix elements (thin line) and including the k dependence of M_{cv} (thick). The peaks in the absorption are somewhat more pronounced in the latter, but the differences are small. For transitions between two different pairs of bands or transitions in tubes with different chirality, however, the matrix elements change. Figure 23b shows that the matrix elements depend on the chiral angle. M_{cv} also changes for electronic states originating from the KM (Z2, A2) and the ΓK (Z1, A1) part of the graphene Brillouin zone in the zone-folding approximation. This can be traced back to the optical properties of graphene [87,162].

The electronic density of states and also the joint density depend dramatically on the dimensionality of a system (see Fig. 24). For parabolic bands, found in most semiconductors, it rises as the square root of the energy above the bandgap in the three-dimensional case, exhibits a step-like dependence in two-dimensional solids, diverges as the inverse of a square root in one-dimensional systems, and, finally, is a δ-function in zero dimensions. Close to their minimum and maximum bands can always be approximated as parabolic. We thus expect a $1/\sqrt{E}$-behavior for the density of states in nanotubes. This result can be derived more rigorously using, e.g., the zone-folding approach [20, 153, 163]. The singular square-root dependence of the DOS on energy was observed by scanning tunneling spectroscopy [164, 165].

The second important term determining the strength of the optical absorption is the matrix element. Table 9 lists the selection rules for optical ab-

Table 9. Optical selection rules for carbon nanotubes [20, 87]. The (x, y) polarized transitions are strongly suppressed by the depolarization effect, see Sect. 6.4

Polarization	Representation	Δm	Remarks
z	A_{2u}	0	$\left\{\begin{array}{l} \text{valence and conduction bands lying} \\ \text{symmetrically to } E_\mathrm{F} \end{array}\right.$
(x, y)	E_{1u}	± 1	$\left\{\begin{array}{l} \text{only first pair of } E_\mathrm{v} \text{ and } E_\mathrm{c} \\ \text{in zigzag tubes} \end{array}\right.$
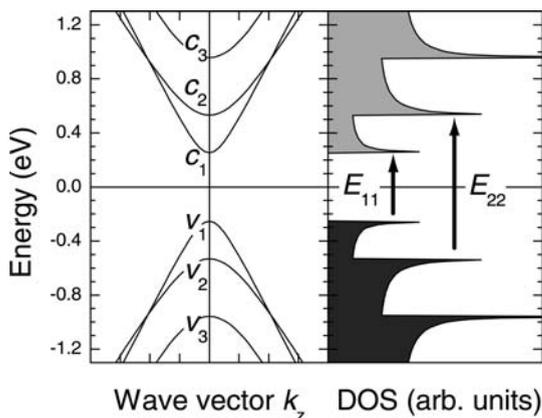
Fig. 25. Band structure and density of states of a zigzag nanotube. The band-to-band transition picture predicts that transitions between symmetrically lying pairs of valence and conduction bands contribute the most to the absorption. The transition energies are labeled E_{ii} where i labels the bands

sorption. For z-polarized light absorption is allowed between electronic bands with the same m, otherwise it is forbidden. Under perpendicular polarization the photon changes the band index by ± 1. In zigzag tubes (x, y) polarized absorption is allowed starting from the first two valence bands only. The perpendicularly polarized transitions are strongly suppressed by the anisotropic polarizability [166]. The tube acts as a Faraday cage for an electric field perpendicular to its axis. This makes carbon nanotubes almost transparent for inplane polarization (see Fig. 39b and the discussion in Sect. 6.4).

The overall picture for explaining the optical properties of carbon nanotubes within the band-to-band model is summarized in Fig. 25. The valence (v_i) and conduction bands (c_i) give rise to square-root singularities in the electronic density of states. Selection rules and the depolarization effect make the transitions for symmetrically lying pairs by far the dominant contribution, e.g., $v_1 \rightarrow c_1$. The absorption probability is particularly large when the density of states is high in the initial (valence) and final (con-
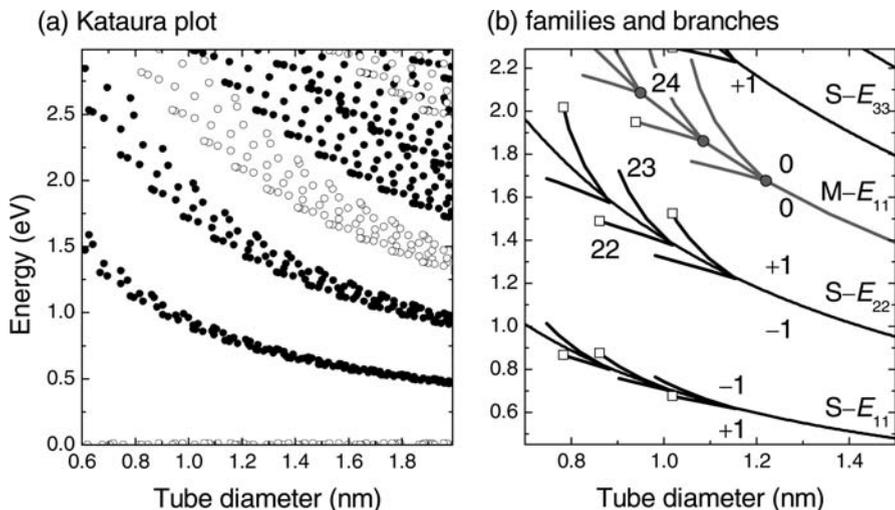
Fig. 26. (**a**) Kataura plot: transition energies of semiconducting (*filled symbols*) and metallic (*open*) nanotubes as a function of tube diameter. They were calculated from the van-Hove singularities in the joint density of states within the third-order tight-binding approximation [6]. (**b**) Expanded view of the Kataura plot highlighting the systematics in (**a**). The optical transition energies are roughly proportional to $1/d$ for semiconducting (*black*) and metallic nanotubes (*gray*). The V-shaped curves connect points from selected branches in (**b**), $\beta = 22, 23$ and 24; see text for details. We indicate whether the $\nu = -1$ or the $+1$ family is below or above the $1/d$ trend. *Squares* (*circles*) are transitions of zigzag (armchair) nanotubes

ducting) state. Thus, the absorption should show peaks corresponding to the transitions from the van-Hove singularity of the first valence band v_1 to the singularity of the first conduction band c_1 at an energy E_{11}, followed by $v_2 \to c_2$ at E_{22} and so forth (see Fig. 25). The absorption spectrum is often further approximated by considering only the van-Hove-related transition energies E_{ii} [167, 168]. Plotting them as a function of diameter one obtains the so-called Kataura plot, which we discuss in the next section.

The band-to-band transition picture was believed to be correct for almost ten years and most interpretations of the Raman and optical spectra relied on it. This view changed fundamentally after *Bachilo* et al. [60] measured photoluminescence and absorption from isolated nanotubes, followed by resonant Raman experiments on similar samples by *Telg* et al. [63] and *Fantini* et al. [64]: The experimental data could only be understood on the basis of excitonic transitions. Therefore, the literature has to be viewed with care because many studies relied on the band-to-band description.

5.2 Kataura Plot: Nanotube Families and Branches

When discussing the electronic band structure of carbon nanotubes we found two dependences on the nanotube chirality through zone folding: The separation between two lines of allowed wavevectors is given by $2/d$. On the other hand, the direction of the allowed lines with respect to the graphene Brillouin zone was connected with the chiral angle Θ (see Sect. 4.1). The optical transition energies depend, consequently, on these two parameters. This can be used to assign the chirality of a tube by Raman scattering and optical spectroscopy (see Sect. 7) [60, 61, 63, 64, 68].

Taking the maxima in the band-to-band absorption probability (the energy separation of the van-Hove singularities in Fig. 25) for an ensemble of nanotubes and plotting them as a function of the tube diameter d, we obtain Fig. 26a. The plot is named after *Hiromichi Kataura*, who first used it in connection with optical spectroscopy [167]. There are a number of systematics in the Kataura plot, which we discuss now. In the infrared and over most of the visible energy range an ensemble of nanotubes has well-separated ranges of transition energies for a given diameter range. The energies follow roughly $1/d$. The deviations from this trend reflect the chiral-angle dependence of the optical spectra. Figure 26b shows a part of the plot on an enlarged scale and concentrates on the systematics. The transition energies of metallic tubes (M–E_{11}, gray lines) are clearly separated from the semiconducting transitions (S–E_{ii}, black). Also, at first sight, semiconducting tubes seem to have more electronic transitions than metallic ones (however, this impression is not correct, in metallic tubes two transitions are always close in energy, see below). The first observation can be understood by the zone-folding approach.

Figure 27a–c shows the allowed wavevector lines of a metallic (a) and two semiconducting tubes (b,c) close to the K point of graphene (see Fig. 18). The electronic energies in the vicinity of this point give rise to transitions in the near infrared and the visible. In the metallic tube of Fig. 27a an allowed line goes through the K point (zero transition energy); the two neighboring lines, which are the origin of the M–E_{11} absorption, are at a distance of $2/d$ from K. In a semiconducting tube the first allowed line is $2/3d$ away from K (S–E_{11}), the next $4/3d$ (S–E_{22}), then $8/3d$ (S–E_{33}), $10/3d$ and so forth (see Fig. 27b). Close to the K point, the graphene band structure is approximately linear with wavevector. Therefore, the ordering of the optical energies will be S–E_{11}, S–E_{22}, M–E_{11}, S–E_{33}, . . ., all of them well separated in energy for a given $d \approx 1$ nm [153, 163].

The systematic deviations of the optical energies from the $1/d$ trend in Fig. 26 reflect the trigonal distortion of the graphene band structure, i.e., the fact that the energies depend on the direction of $(\boldsymbol{k} - \boldsymbol{K})$ [150, 169]. The trigonal distortion is clearly visible in the contours of Figs. 27a–c (see also Fig. 28): Without trigonal distortion the contour lines would be circles. The two M–E_{11} lines in Fig. 27a cross slightly different contours. Therefore,
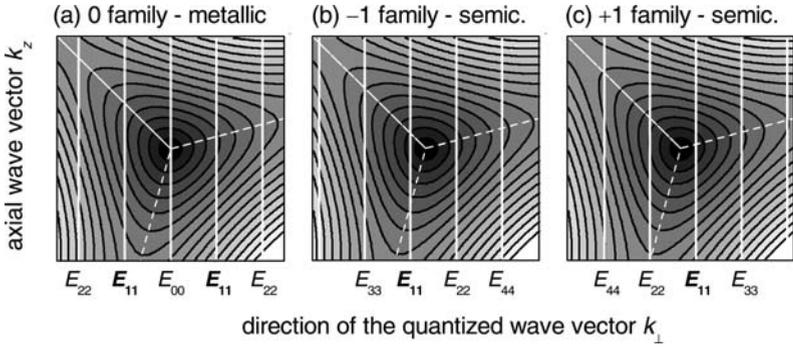
Fig. 27. Lines of allowed wavevectors for the three nanotube families on a gray-scale plot of the electronic band structure of graphene (K point at center). (**a**) Metallic nanotube belonging to the $\nu = 0$ family, (**b**) semiconducting -1 family tube, and (**c**) semiconducting $+1$ family tube. Below the allowed lines, the optical transition energies E_{ii} are indicated. Note how E_{ii} alternates between the left and the right of the K point in the two semiconducting tubes. The assumed chiral angle is $15°$ for all three tubes; the diameter was taken to be the same, i.e., the allowed lines do not correspond to realistic nanotubes. After [150]
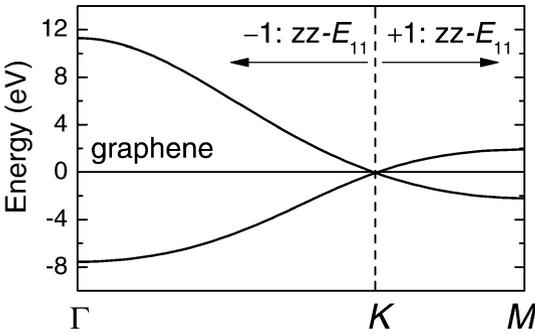
Fig. 28. Electronic band structure of the π and π^* states of graphene along the ΓKM line, which is the confinement direction for zigzag nanotubes. The electronic dispersion between Γ and K is stronger than between K and M. Zigzag tubes from the -1 family have a larger bandgap than those of the $+1$ family; see *arrows*

metallic nanotubes have two close-by transition energies that generate the V-shaped structure in Fig. 26b. A similar systematics applies to semiconducting nanotubes. Here, the splitting does not occur within one tube, but for two groups of semiconducting tubes, known as nanotube families [150].

The first allowed line in Figs. 27b and c are at the same distance from K. However, in Fig. 27b E_{11} is to the left of the K point (between Γ and K), whereas it is to the right in Fig. 27b (between K and M). Since the electronic

dispersion is stronger between Γ and K than between K and M (see Fig. 28), the tube in Fig. 27b has a larger band gap and hence a larger transition energy E_{11} than the tube in Fig. 27c. For E_{22} the situation is reversed, because this transition originates from the opposite side of K. S–E_{33} behaves like S–E_{11}.

Whether S–E_{11} is to the right or to the left of the K point of graphene after the zone-folding scheme, is a function of n_1 and n_2 [150]. A nanotube belongs to the group or "family" in Figs. 27a,b and c if

$$\nu = (n_1 - n_2)\mathrm{mod}3 = \begin{cases} -1 & \text{semiconducting, large bandgap } E_{11}, \text{ part b} \\ 0 & \text{metallic, part a} \\ +1 & \text{semiconducting, small bandgap } E_{11}, \text{ part c.} \end{cases}$$

$$(20)$$

Nanotube families were first suggested by us [150], but picked up only two years later after optical spectroscopy on isolated nanotubes was reported for the first time [59,60]. Optical spectroscopy was the first method sensitive enough to measure the family dependence of carbon nanotubes. The concept proved to be vital for the understanding of carbon nanotubes; many of their properties change with the family index ν. The three nanotube families are also indicated in the chiral-index plot in Fig. 3.

Nanotube families explain why some tubes fall above and some below the $1/d$ trend in Fig. 26. Where, however, does the peculiar V-shaped structure come from? The Vs reflect the "branches" in the Kataura plot. Within a branch β, by definition (Table 1),

$$2n_1 + n_2 = \beta = \text{const.} \tag{21}$$

Using (21) we immediately derive the neighbor rule, which gives the chiral index of a neighboring nanotube (n_1', n_2') with smaller diameter within a branch, i.e., with $\beta = \text{const.}$

$$n_1' = n_1 - 1 \quad \text{and} \quad n_2' = n_2 + 2 \qquad \text{as long as } n_1 \geq n_2. \tag{22}$$

Looking back at Fig. 3 we see that $\beta = \text{const.}$ corresponds to vertical lines in the chiral-index plot. For such a line the diameter of a tube decreases with decreasing chiral angle. At the same time, trigonal warping increases with decreasing chiral angle [150, 169]. An armchair tube with $\Theta = 0°$ shows no splitting related to trigonal warping. Its allowed lines run perpendicular to the base of the triangle in Fig. 27, i.e., the left and the right of K are at the same energy. Armchair tubes are at the centers of the metallic V-shaped curves, see circles in Fig. 26b. In contrast, for zigzag tubes the trigonal distortion is strongest [150]. Their allowed lines touch the tip and the base of the triangle of Fig. 27. Hence, $(n, 0)$ zigzag and $(n_1, 1)$ chiral nanotubes are at the end of the Vs in Fig. 26b; see open squares. A summary of the nanotube classifications presented here is given in Table 2.

Nanotube families and nanotube branches play an important role in the interpretation of experiments. The key point is that the nanotube properties depend systematically on the family and branch they belong to and the position within one branch. The change in bandgap for different families is the most obvious example, further examples in connection with Raman and optical spectroscopy include the Raman, photoluminescence and absorption intensity, the softening of the high-energy phonons, electron–phonon coupling and many other properties [45, 60, 63, 64, 111, 144, 162, 170, 171].

5.3 Excitons

An electron and a hole in a crystal can form a bound state called an exciton [134]. This is mathematically equivalent to the hydrogen problem except for the existence of a center-of-mass k vector because of the translational invariance along the tube (see, e.g., [134]). The exciton binding energy in a three-dimensional solid assuming electron–hole symmetry is given by

$$E_{\mathrm{b}} = \frac{m^*}{2\varepsilon_{\mathrm{cr}}^2}\mathrm{Ry}\,. \tag{23}$$

This is much smaller than the ionization energy of hydrogen $1\,\mathrm{Ry} = 13.6\,\mathrm{eV}$, because the effective mass m^* is only a fraction of the electron mass and the Coulomb interaction is screened by the dielectric constant $\varepsilon_{\mathrm{cr}}$. Inserting typical values for semiconductors into (23) $m^* \approx 0.01$ (in units of the electron mass) and $\varepsilon_{\mathrm{cr}} \approx 4$ we obtain binding energies on the order of a few m eV. In many bulk crystals excitonic effects are only important at low temperature, where the thermal energy $k_{\mathrm{B}}T \lesssim E_{\mathrm{b}}$.

The exciton binding energy, however, depends on the dimension of the solid [172, 173]. For a 2D system E_{b} increases by a factor of four within the hydrogen model compared to 3D crystals. Although nanotubes are one-dimensional systems, a 2D model is most appropriate, since the electron and the hole move on a cylindrical surface [13]. Additionally, screening is less efficient in a low-dimensional solid. Assuming a 2D hydrogen model and no dielectric screening, the exciton binding energy increases to $E_{\mathrm{b}}(2\mathrm{D}) = 4E_{\mathrm{b}}(3\mathrm{D}) = m^*4\,\mathrm{Ry}/2 \approx 300\,\mathrm{meV}$. More sophisticated estimates for the exciton binding energy in carbon nanotubes yield $E_{\mathrm{b}} = 1\,\mathrm{eV}$ to $1.5\,\mathrm{eV}$ for diameters $d \approx 1\,\mathrm{nm}$ and tubes in vacuum [10, 160, 161, 174]. This is much larger than the thermal energy at room temperature $k_{\mathrm{B}}T \approx 25\,\mathrm{meV}$. Excitons in carbon nanotubes are thus observable at room temperature and below.

The particular importance of the excitonic interaction for spectroscopy is that it fundamentally changes the optical excitations. This is illustrated in Fig. 29. Instead of exciting electrons from the valence into the conduction band, as in the band-to-band model (see Fig. 25), the photon excites an exciton from the ground state into the optically active states eh_{ii} formed by

(a)

(b)
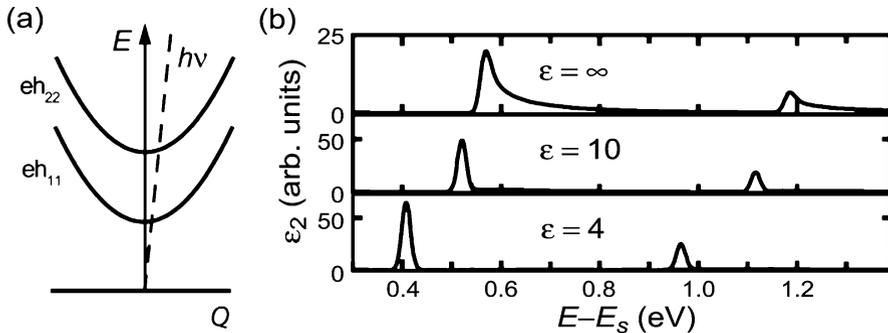
Fig. 29. (a) Schematic dispersion of the first eh_{11} and second eh_{22} subband excitons. Q is the exciton wavevector defined as the center-of-mass wavevector of electron and hole. $h\nu$ indicates the dispersion of photons. Absorption occurs at the crossing of the photonic and excitonic dispersion with a wavevector $Q_{abs} \approx 0$. After [134]. (b) Calculated absorption spectra neglecting electron–hole interaction (band-to-band transitions), $\varepsilon = \infty$ *top panel*, and for decreasing screening, *middle* and *bottom panels*. The shift in the main transition indicates the exciton binding energy as a function of ε. With decreasing screening, more spectral weight is transfered to the exciton. After [160]

electrons and holes in the ith subband (see Fig. 29a). The combined electron–hole wavevector $\boldsymbol{Q} = \boldsymbol{k}_e + \boldsymbol{k}_h$ has to be equal to the wavevector of the photon, $\boldsymbol{Q} \approx 0$ ($\boldsymbol{k}_e$ and $\boldsymbol{k}_h$ are the wavevectors of the electron and the hole, respectively).

Figure 29b shows how the optical absorption spectrum changes when electron–hole interaction is considered. The results were obtained for a (19,0) tube using a tight-binding model to solve the Bethe–Salpeter equation, a two-particle equation, which includes electron–hole interaction [160]. The characteristic $1/\sqrt{E}$ absorption predicted for band-to-band transitions (top panel and Fig. 25) changes into a δ-function when the spectral weight is transferred from the electron–hole continuum to the excitons. ε is the dielectric function of the medium surrounding the tube.

The two peaks in the three panels of Fig. 29b originate from transitions between the first two pairs of valence and conduction bands in the top panel and from exciting the first and second subband exciton in the middle and lower panels. The shift in the peak position gives the exciton binding energies for two dielectric constants ε of the medium surrounding the tube.

From what we discussed up to now, one would expect the experimental optical transitions to be lower in energy than predicted from the single-particle picture, because of the large exciton binding energies. Instead, photoluminescence and Raman spectroscopy found a blueshift of the transitions by some $100\,\mathrm{meV}$ when compared to a single-particle theory [44, 45, 60, 61, 63, 64, 68]. The origin of this shift is the increase of the bandgap due to electron–electron interactions [10,174]. As shown in Fig. 30, electron–electron
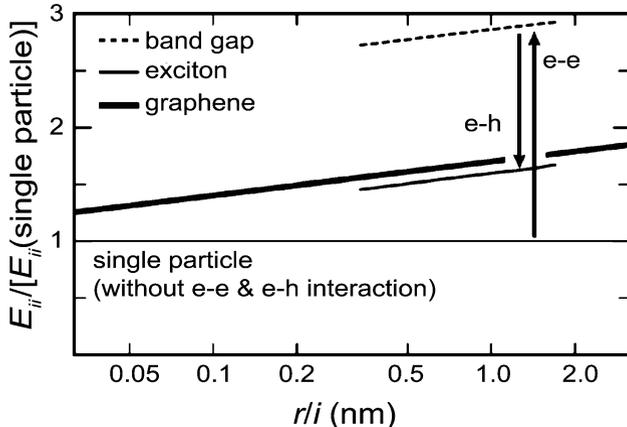
Fig. 30. Electron–electron interaction increases the separation between the ith valence and conduction band (*dashed lines*) by approximately 1.8 eV compared to the single-particle picture (*horizontal full line* at 1). The binding energy due to electron–hole interaction is around 1.3 eV. The excitonic transitions (*full thin lines*) are blueshifted compared to the band-to-band transitions. The *full thick line* was obtained by zone folding (see [174] for details). Note the log scale for x. After [174]

interaction (e–e) increases the electronic gap compared to the single-particle approximation. This increase is almost canceled by the electron–hole interaction (e–h). Nevertheless, the exciton in Fig. 30 is somewhat higher in energy than the single-particle states.

Figure 31 shows an experimental Kataura plot, i.e., the measured optical transition energies as a function of tube diameter. We will explain in Sect. 7 how the transition energies can be assigned to carbon nanotubes experimentally to plot them as in Fig. 31. The figure shows the first two transitions for semiconducting tubes measured by photoluminescence and Raman scattering and the first transition of metallic tubes from Raman spectroscopy [60, 63]. Only the lower parts of the metallic branches were observed experimentally; see Fig. 26. The energies of the optical transitions can be well understood, at least qualitatively, considering the single-particle states, electron–electron and electron–hole interaction, and the curvature of the nanotube walls [74, 160, 170, 174].

The exciton binding energies of single-walled carbon nanotubes were measured by two-photon absorption. These experiments probe the energy of excited excitonic states by the simultaneous absorption of two photons. The binding energy can be estimated from the energy difference between the exciton ground state (one-photon absorption) and the excited state (two-photon absorption). *Wang* et al. [12] and *Maultzsch* et al. [13] reported $E_b \approx 0.4$ eV for nanotubes coated by surfactants. This is in reasonably good agreement with theory when the screening by the surfactant is taken into account.
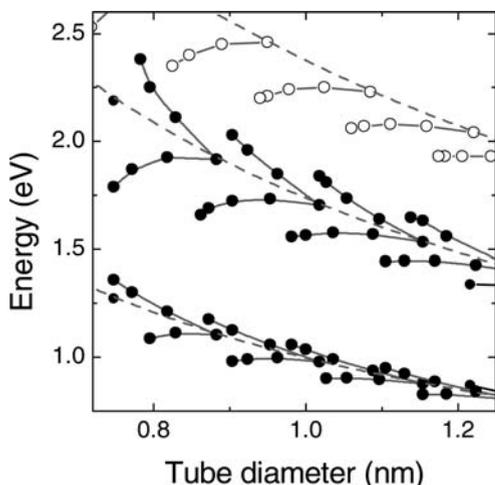
Fig. 31. Experimental Kataura plot for the first two semiconducting (*closed symbols*) and the first metallic (*open symbols*) transition. *Dashed lines* connect the (near-to) armchair tubes; *full lines* connect tubes in a branch, compare Fig. 26 and Table 2. Experimental transition energies were measured with photoluminescence [60] and resonant Raman scattering [63]

Optical spectroscopy of isolated nanotubes has been a rapidly evolving field over the last three years, but many aspects are still not understood. For example, side peaks in the photoluminescence excitation spectra of single-walled carbon nanotubes have been interpreted as phonon side bands of excitons [175, 176], coupled exciton–phonon excitations [11, 177], or excited excitonic states [13]. The variation in the nanotube absorption and emission intensity with chirality has been attributed either to electron–electron [74] or to electron–phonon interaction [75]. Nevertheless, the two-photon absorption experiments proved the optical excitations to be of excitonic character in single-walled carbon nanotubes [12, 13]; prior to the measurement of the exciton binding energy, time-resolved spectroscopy also suggested formation of excitons [178–182]. The band-to-band transition picture is thus not fully appropriate when modeling either photon absorption and emission or Raman scattering. On the other hand, a unified description of the Raman effect including excitonic effects is still missing. In this Chapter we will use mainly the band-to-band transition picture to model Raman scattering in carbon nanotubes pointing out important differences and consequences that should arise when electron–hole interaction is taken into account.
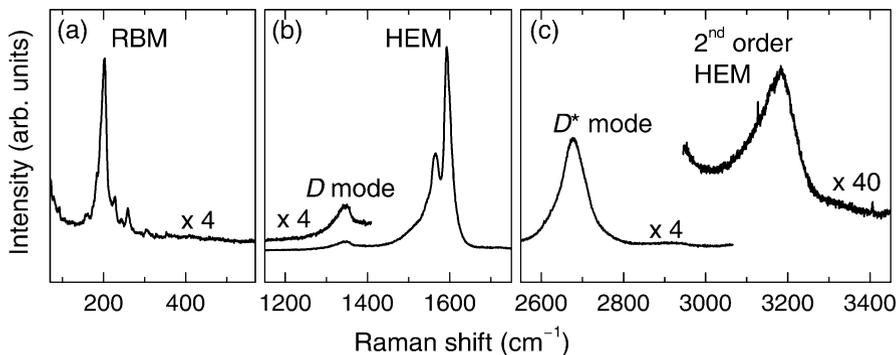
Fig. 32. Raman spectrum of bundles of single-walled carbon nanotubes excited with $\lambda_L = 488$ nm. (**a**) Radial-breathing mode (RBM), (**b**) D mode and high-energy modes (HEM), (**c**) two-phonon Raman spectrum with the D^* (overtone of the D) and the overtone spectrum of the HEM. The spectra were multiplied by the factors given in the panels. From [186]

6 Raman Effect in Carbon Nanotubes

Resonance Raman scattering refers to a technique where one or more transitions participating in the scattering process involve real states. It has been widely used to study electronic states in solids (see other volumes of this series [183], in particular the seminal articles by *Cardona* [184] and by *Martin* and *Falicov* [185]).

After introducing the Raman spectrum of single-walled carbon nanotubes, we show in this section how the enhancement of the Raman-scattering intensity through resonances is involved in all the reported spectra of nanotubes: nonresonant Raman scattering is simply too weak to be observed in this material. Both single and double resonances are observed in carbon nanotubes; they have distinct features and yield different kinds of physical insight into the nanotubes. Double resonances are much more widely present in nanotubes than in 2- or 3-dimensional solids; they are, in fact, the dominant scattering mechanism for the high-energy modes.

6.1 Raman Spectra of Single-Walled Nanotubes

Figure 32 shows the three energy ranges where the most important Raman features of single-walled carbon nanotubes are observed [20, 26, 145, 187–189]. In the low-energy range (Fig. 32a) there are several peaks in nanotube bundles or nanotubes in solutions resulting from the radial-breathing modes of the resonantly excited tubes (see Sect. 3.2). For a single tube, there would be only a single radial-breathing mode peak. Its frequency depends on diameter, these modes are typically found between $100\,\mathrm{cm}^{-1}$ and $400\,\mathrm{cm}^{-1}$. The radial-breathing mode is a vibration characteristic of carbon nanotubes and is often
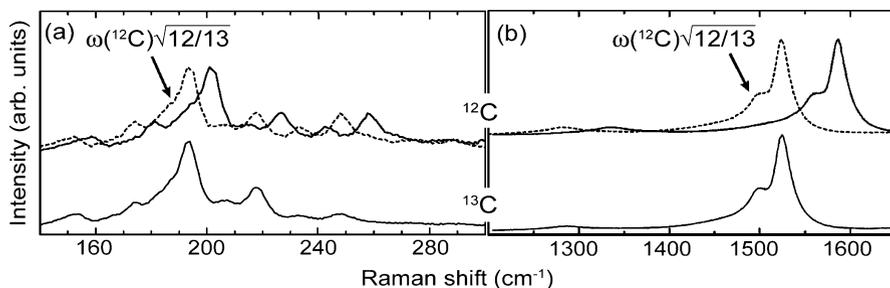
Fig. 33. Low (**a**) and high-energy (**b**) Raman spectra of ^{12}C (*upper traces*, *full lines*) and of ^{13}C (*lower traces*). The *dashed lines* are the ^{12}C spectra with the frequency multiplied by the expected isotope shift ($\sqrt{12/13}$). From [195]

considered as their fingerprint. However, since many materials have vibrational frequencies in this energy range, the presence of single-walled tubes in a sample cannot be surmised from the low-energy spectrum [190–193].

The D mode in Fig. 32b is an intriguing Raman peak that arises from double-resonant Raman scattering [4]. Its frequency depends on the energy of the exciting laser; we discuss this mode in Sect. 10.

The high-energy modes (HEM) of single-walled tubes originate from tangential vibrations of the carbon atoms (Sect. 3.3), i.e., along the nanotube walls [187, 194]. The double-peak structure close to $1600\,\mathrm{cm}^{-1}$ in Fig. 32b is a unique feature of single-walled carbon nanotubes. It is a more reliable Raman signature of single-walled tubes than the RBMs in the low-energy range. Typically, the most intense peak in the high-energy range occurs between $1592\,\mathrm{cm}^{-1}$ and $1596\,\mathrm{cm}^{-1}$ (depending on diameter and excitation energy); it is always higher in frequency than the corresponding peak in graphite ($1589\,\mathrm{cm}^{-1}$ [145]). The smaller peak between $1560\,\mathrm{cm}^{-1}$ to $1590\,\mathrm{cm}^{-1}$ changes dramatically for resonant excitation of metallic tubes (Sect. 8 [168, 188]).

Between the RBM in Fig. 32a and the high-energy range with the D mode and the HEM a number of weak Raman peaks are observed [187, 196]. We will not review this so-called intermediate frequency range but refer the reader to [26].

Figure 32c shows the overtone Raman spectrum of single-walled carbon nanotubes. Note that D^*, the overtone of the D mode, is stronger in intensity than its fundamental. The two-phonon Raman spectrum of carbon nanotubes is similar to that of other sp^2-bonded carbons, but the overtone of the HEM is at lower frequency than in graphite (see Sect. 10).

In Fig. 33 we show Raman spectra of single-walled carbon nanotubes where ^{12}C (98.93 % natural abundance) was replaced by ^{13}C [195]. Phonon frequencies are proportional to $1/\sqrt{m}$ (spring model); hence we expect the frequencies to shift by $\sqrt{12/13} \approx 4\,\%$ when replacing naturally occurring carbon by the pure ^{13}C isotope. The full lines in the upper traces of Fig. 33
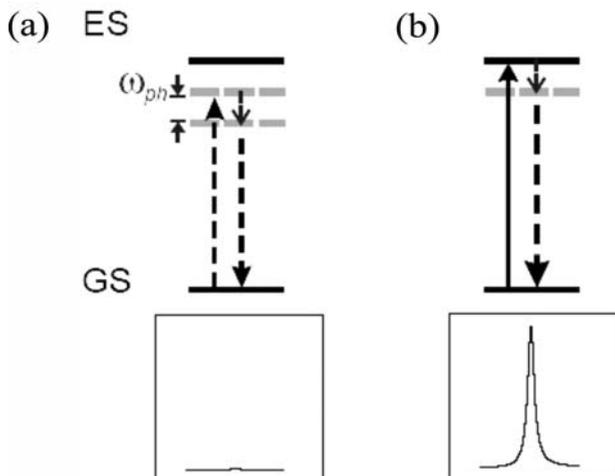
Fig. 34. Schematic of (**a**) nonresonant (Stokes) scattering and (**b**) a single (incoming) resonance. GS (ES) refer to the ground (excited) state of the material investigated and ω_{ph} to the phonon (or other elementary excitation) emitted in the process. The corresponding relative strengths in a Raman spectrum are indicated on the *bottom*

are the as-measured ^{12}C Raman spectra; for the broken lines the frequencies were multiplied by the expected isotope shift. There is excellent agreement with the ^{13}C Raman spectra shown in the lower traces of Fig. 33 [195, 197].

6.2 Single Resonances

The concept of a single resonance is illustrated in Fig. 34. Nonresonant Raman scattering corresponds to the excitation of an electron from the ground state (GS) to a virtual state (gray, dashed line) followed by emission (Stokes scattering) or absorption of a phonon (anti-Stokes, not shown) and subsequent recombination of the electron–hole pair (a). Increasing the excitation energy leads to the excitation of an electron into a real (empty) state (b).

Since the exciting laser light is in resonance, one speaks of an *incoming* resonance. Increasing the excitation energy further leads to an *outgoing* resonance and, finally, again to a nonresonant situation.

Whether incoming or outgoing resonances can be resolved experimentally depends on the width ($\sim$ inverse lifetime) of the excited electronic state. If it is too broad compared to the energy of the phonon (or other elementary excitation), they cannot be resolved. This is the situation for the resonances of the radial-breathing mode (ω_{RBM} in the range $150\,\mathrm{cm}^{-1}$ to $250\,\mathrm{cm}^{-1}$ for typical nanotubes), and an extraction of the precise transition energies from resonance spectra has to take this into account; see Sect. 7. In total, six different time-order diagrams contribute to first-order Raman scattering, of

which we showed in Fig. 34 only one. In general, there are, of course, many excited states that have to be included for proper calculation of the Raman spectra; see, e.g., [185, 198].

The Raman efficiency of a bulk material for Stokes scattering, i.e., the number of photons per incident photon per unit length and solid angle $d\Omega$ is given by [184, 185, 199]

$$\frac{dS}{d\Omega} = \frac{1}{V}\frac{d\sigma}{d\Omega} = \frac{\omega_1\omega_2^3}{4\pi^2}\frac{\eta_1\eta_2^3}{c^4}\frac{V_cN}{(\hbar\omega_1)^2}\sum_f |K_{2f,10}|^2[N(\omega)+1]\,, \tag{24}$$

where $K_{2f,10}$ is the Raman matrix element (see below) with the final state f with frequency ω. $d\sigma/d\Omega$ is called the differential Raman cross section. $V = V_cN$ is the scattering volume and V_c is the volume of the unit cell. In the one-dimensional systems we want to consider here, the scattering volume is equivalent to the scattering length L. ω_1 and $\omega_2 = \omega_1 - \omega$ are the frequencies of the incoming and outgoing light, respectively. η_1 and η_2 are the indizes of refraction at ω_1 and ω_2. $N(\omega) = 1/[\exp(\hbar\omega/k_BT) - 1]$ is the Bose–Einstein occupation factor and c is the speed of light in vacuum.

We can express the resonant process by using the Raman matrix element $K_{2f,10}$ [185]

$$K_{2f,10} =$$
$$\sum_{a,b} \frac{\langle\omega_2, f, i|H_{\mathrm{eR},\rho}|0, f, b\rangle\langle 0, f, b|H_{\mathrm{ep}}|0, 0, a\rangle\langle 0, 0, a|H_{\mathrm{eR},\sigma}|\omega_1, 0, i\rangle}{(E_1 - E_{ai}^e - i\gamma)(E_1 - \hbar\omega - E_{bi}^e - i\gamma)}\,, \tag{25}$$

where $|\omega_1, 0, i$ denotes the state with an incoming photon of energy $E_1 = \hbar\omega_1$, the ground state 0 of the phonon (no phonon excited), and the ground electronic state i; the other states are labeled accordingly. Initial and final electronic states are assumed to be the same, the sum is over all possible intermediate electronic states a and b. The final state is denoted by f. The E_{ai}^e are the energy differences between the electronic states a and i; $\hbar\omega$ is the phonon energy, and the lifetimes of the various excited states are taken to be the same. The three terms in the numerator are the matrix elements for the coupling between electrons (e) and radiation (R, incoming and outgoing photons with polarization σ and ρ, respectively) and the coupling between electrons and phonons (p).

Figure 34b corresponds to the incoming photon of energy E_1 matching the energy of the electronic state E_{ai}^e in (25). As mentioned, Fig. 34b describes an incoming (single) resonance. In the outgoing resonance the photon emitted in the recombination process matches an eigenenergy of the system, $E_1 - \hbar\omega = E_{bi}^e$. The Raman intensity is given by the magnitude squared of $K_{2f,10}$, leading to the strong enhancements in the spectra when the incoming (or outgoing) photon energy matches a transition of the system. By using appropriate energies of tunable lasers the real electronic states of a material
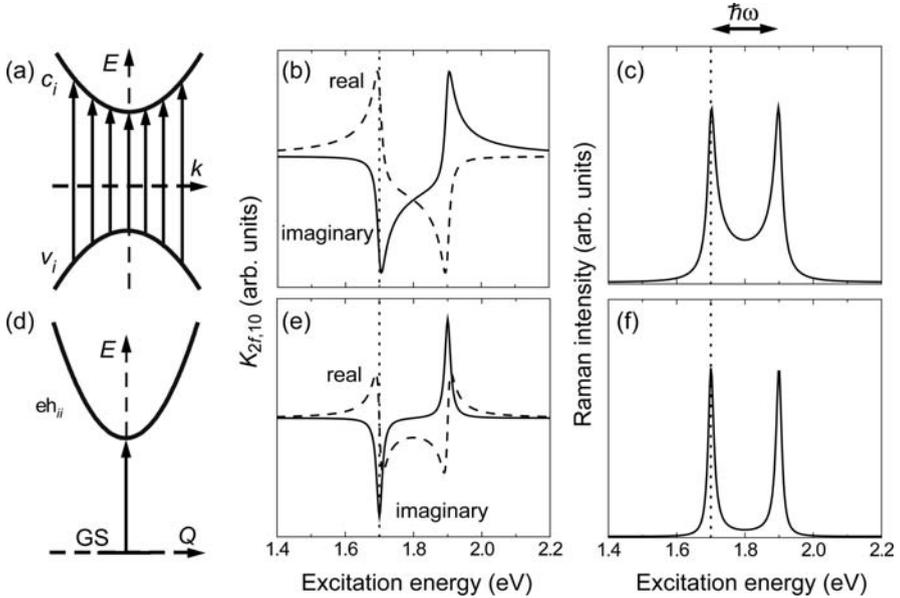
Fig. 35. Raman-scattering efficiency and resonance profiles for band-to-band transitions and excitons in one-dimensional systems. (**a**) Parabolic valence (v_i) and conduction (c_i) band with a gap E_{ii}. Optical excitations (*arrows*) are nearly vertical to conserve momentum. (**b**) Real (*dashed line*) and imaginary (*full*) part of the Raman matrix element $K_{2f,10}$ for band-to-band transitions and $E_{ii} = 1.7$ eV, $\hbar\omega = 0.2$ eV (1600 cm^{-1}), and $\gamma = 0.01$ eV. (**c**) Raman efficiency $\propto |K_{2f,10}|^2$ calculated from (**b**). The profile is symmetric with an incoming and outgoing resonance. (**d**) Parabolic exciton dispersion eh_{ii} over the combined wavevector $Q = k_{\mathrm{e}} + k_{\mathrm{h}}$. Optical excitations (*arrow*) occur at $Q \approx 0$ only. (**e**) same as (**b**) but for excitonic intermediate states in the Raman process [the parameters are the same as in (**b**)]; (**f**) Raman profile calculated from (**e**)

can be studied systematically. The authoritative review article on solid-state systems using this technique is [184].

When calculating the matrix element, it is important to evaluate the sum in (25) *before* taking the absolute square in (24). Physically speaking, this corresponds to taking into account interferences between the different contributions to the scattering amplitudes. The simplification of replacing the sum by a density of states, i.e., ignoring interferences, is only correct if the scattering events are independent, say at very different energies of the elementary excitation, or in different tubes. In general, however, the sum must be evaluated explicitly. Although this is well known (see, e.g., *Martin* and *Falicov* [185]), it is frequently forgotten or ignored in the nanotube literature. *Bussi* and coworkers [200,201] recently calculated the sum in (25) and showed that for typical (RBM) phonon and electronic energies in metallic nanotubes such interference effects are indeed important for the identification of elec-

tronic transition energies (see Sect. 9.2). Because of its importance we show below for parabolic electronic bands and for transitions into excitonic states how the sum is evaluated, following the derivation in [185].

Abbreviating the numerator in (25) by $\mathcal{M}$ and taking the electronic bands to be described by

$$E^e_{ai}(k) = E^e_{bi}(k) = E_{ii} + \hbar^2 k^2 / 2\mu, \tag{26}$$

(see Fig. 35a) where k is the magnitude of the electron wavevector and $1/\mu = 1/m_e + 1/m_h$ is the reduced effective mass, we define

$$\zeta^2_0 = -(E_1 - E_{ii} - i\gamma) \quad \text{and} \quad \zeta^2_1 = -(E_1 - \hbar\omega - E_{ii} - i\gamma). \tag{27}$$

For just one set of valence and conduction bands the sum in (25) can be converted into an integral over k, i.e., over all possible vertical transitions, we obtain

$$K_{2f,10} = \frac{\sqrt{2\mu}}{\hbar} \frac{L}{2\pi} \int_{-\infty}^{\infty} \frac{\mathcal{M} d\zeta}{(\zeta^2 + \zeta^2_0)(\zeta^2 + \zeta^2_1)}, \tag{28}$$

where we have substituted k by $(\sqrt{2\mu}/\hbar)\zeta$, and L is the tube length (or scattering "volume").[5] We obtain for band-to-band transitions in the parabolic approximation

$$K_{2f,10} = \frac{L\sqrt{\mu/2}}{i\hbar^2\omega} \left(\frac{\mathcal{M}}{\sqrt{E_1 - E_{ii} - i\gamma}} - \frac{\mathcal{M}}{\sqrt{E_1 - \hbar\omega - E_{ii} - i\gamma}} \right). \tag{29}$$

The first term in parentheses describes the incoming resonance, the second one the outgoing resonance.

When more than one electronic band is involved, the sum $\sum_{a,b}$ in (25) has to include different bands besides the different wavevectors. This leads to several similar terms in (29) with possibly different electron–phonon and electron–photon coupling strengths $\mathcal{M}'$. We will show an example where interferences between these terms lead to important differences in the determination of resonance energies in Sect. 9.2 [201].

In Fig. 35b we show the real and imaginary part of $K_{2f,10}$ in (29) as a function of the excitation energy E_1. $E_{ii} = 1.7$ eV is indicated by the dashed vertical line and $\hbar\omega = 0.2$ eV (see arrow in Fig. 35c). The imaginary part has the typical square root singularity $|E|/\sqrt{E^2 - E_{ii}^2}$ of the joint density of states in one-dimensional solids [153]. The real part, however, shows a different energy dependence: it is larger for energies below E_{ii} and $E_{ii} + \hbar\omega$. The resulting Raman efficiency, which is proportional to $|K_{2f,10}|^2$, is shown in Fig. 35c. The two maxima arise from the incoming resonance at E_{ii} and

---

[5] The integral in (28) can be solved by making ζ a complex variable and summing over the residues in, say, the upper half of the complex plane [202].

the outgoing resonance $E_{ii} + \hbar\omega$. The Raman profile does not resemble the joint density of electronic states, as erroneously assumed in, e.g., [94].

We now consider excitonic states as the intermediate states a, b in the Raman process. The evaluation of (25) is slightly different from the band-to-band case. For an exciton, the energies in (25) are (see Fig. 35d),

$$E^e_{ai} = E^e_{bi} = \mathrm{eh}_{ii}(Q \approx 0)\,, \tag{30}$$

i.e., there is only one transition, and no integration over the wavevector is needed because the exciton momentum $Q \approx 0$ for optical transitions (Q is the wavevector of the exciton $Q = k_\mathrm{e} + k_\mathrm{h}$, see Sect. 5.3). We obtain from (25) for excitonic transitions

$$K_{2f,10} = -\frac{1}{\hbar\omega}\left(\frac{\mathcal{M}}{E_1 - eh_{ii} - i\gamma} - \frac{\mathcal{M}}{E_1 - \hbar\omega - eh_{ii} - i\gamma}\right)\,. \tag{31}$$

Figure 35e shows the real and imaginary parts of $K_{2f,10}$ for an excitonic intermediate state. Both parts are different from the band-to-band case in Fig. 35b. The measurable quantity, however, the Raman efficiency (or intensity) in Fig. 35f is again a two-peak profile with an incoming resonance at eh_{ii} and an outgoing resonance at $eh_{ii} + \hbar\omega$ (we used $eh_{ii} = 1.7$ eV as for E_{ii} in the band-to-band transitions; in reality the two energies differ, see Sect. 5.3). Comparing Figs. 35c and f we find that the exciton resonance is somewhat sharper than a resonance involving band-to-band transitions ($\gamma = 0.01$ eV in both calculations). Using this difference to experimentally discriminate between the two cases is, however, rather difficult, because γ is not independently known.

As first pointed out by *Canonico* et al. [200] the joint density of states has been incorrectly used for modeling the Raman profile, e.g., in [26, 203–205]. This was recently corrected in a paper by the same group [75] but differences from earlier models and results were not discussed. The asymmetric experimental Raman profile in [203] that probably led to the JDOS-based theoretical model can be explained by interferences in the Raman matrix element as shown in [200, 201]. We also note that our paper [168] is somewhat misleading in deriving the Raman cross section (note that the JDOS in [168] corresponds to an ensemble of different tubes that are indeed independent scatterers). The model used for fitting the experimental data, however, is correct.

Graphite and metallic carbon nanotubes, among other materials, have strongly dispersive electronic bands near the Fermi surface; their bands cross the Fermi level with a nearly linear dispersion, see Sect. 4. This leads to real optical transitions at all energies, i.e., the Raman spectra are resonant regardless of the excitation energy, see Fig. 36.

The emitted phonons (gray dashed arrows) correspond to various possible $q \neq 0$ nonresonant carrier-scattering processes. The recombination between eigenstates occurs again such that quasimomentum is conserved, i.e.,
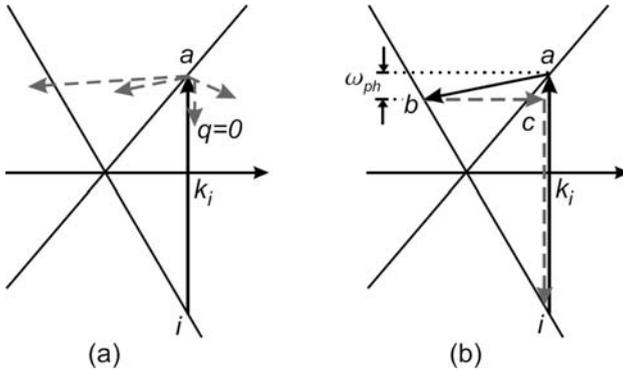
Fig. 36. In graphite the photon in the Raman process is resonant, regardless of the excitation energy. The transitions in both panels are in resonance for the incoming light ($i \rightarrow a$). (**a**) Single resonance: Of all possible phonon emissions (or absorptions) (*gray arrows*) into virtual states only those with ≈ 0 momentum contribute to the Raman-scattering process. There is no second resonant transition. (**b**) Double resonance: the emitted phonon with $q \neq 0$ makes a transition between eigenstates of the system ($a \rightarrow b$), the elastic (defect) scattering ($b \rightarrow c$) and the recombination ($c \rightarrow i$) do not. After [20]

only $q \approx 0$ phonons contribute to a single-resonant process, see Fig. 36a. In general, as long as the phonon emission is not another transition of an electron or hole to an eigenstate of the system, one speaks of a single-resonant Raman process [184]. Compared to nonresonant Raman spectra (Fig. 34a) the only essential new quality of single-resonant spectra (Fig. 34b) is the intensity enhancement due to the vanishing denominator in (25). There are qualitatively different effects in double-resonant Raman scattering that we discuss next.

6.3 Double-Resonant Raman Scattering

Double-resonant scattering processes play an important role in interpreting the Raman spectra of graphite and carbon nanotubes. Double and even triple resonances are known for semiconductors, although they are observed only under special conditions. In the carbon-based materials, though, the double resonance is the dominant process, and its discovery in graphite and carbon nanotubes has led to a big step forward in the understanding of these materials [4, 194, 206, 207].

In analogy to single-resonant scattering one speaks of a double resonance when *two* of the transitions to intermediate states of the system are real (see Fig. 36b). It is clear that both the photon and phonon involved must match quite well the energies in a system for multiple resonances to occur. In semiconductors, a double resonance was observed for a specific setting

of parameters, e.g., by tuning the eigenenergies in a magnetic field or by applying pressure (see [208] or [209]).

Among the many possible nonresonantly emitted phonons in Fig. 36a there are some that scatter the electron from eigenstate a to another eigenstate b. Such a process is depicted in Fig. 36b and adds a second resonance to the Raman process. Note that this process is only allowed for a particular combination of energy and momentum of the phonon that scatters the electron. In this way, phonons with a general quasimomentum q participate in the double-resonant processes. Of course, the overall momentum is conserved in a double resonance as well; the recombination happens (for excitation with visible light) near the point in k-space where the initial absorption occurred. One way of scattering the electron back to k_i is to scatter it elastically off a defect or off a nearby surface. Another possibility is to scatter it inelastically with another phonon. The former process is indicated in Fig. 36b, (process $b \rightarrow c$ runs horizontally, i.e., elastically). The transition $b \rightarrow c$ is nonresonant, as c is not an eigenstate of the system. Recombination occurs from there, conserving quasimomentum. The second possibility, inelastic scattering with another phonon, leads to a Raman signal at twice the phonon energy and does not require a defect to conserve momentum.

The processes described lead to Raman matrix element with an additional resonant denominator as compared to (25) [4, 185, 207].

$$K_{2f,10} = \sum_{a,b,c} \frac{\mathcal{M}_{\text{eR},\rho}\mathcal{M}_{\text{e-defect}}\mathcal{M}_{\text{ep}}\mathcal{M}_{\text{eR},\sigma}}{(E_1 - E_{ai}^e - i\gamma)(E_1 - \hbar\omega_{\text{ph}} - E_{bi}^e - i\gamma)(E_1 - \hbar\omega_{\text{ph}} - E_{ci}^e - i\gamma)}, \quad (32)$$

where we have abbreviated the matrix elements in the numerator by $\mathcal{M}_i$. Specifically, $\mathcal{M}_{\text{e-defect}}$ refers to the elastic interaction of the defect and the scattered electron. Not much is known about this interaction and the assumption that it is elastic and symmetry conserving for the scattered carrier is the simplest but not necessarily the only one. In analogy to the single-resonant term the Raman intensity is strongly enhanced when the denominator vanishes, i.e., when transitions between eigenstates take place in the process. As usual, the processes can occur in different time order and also for the hole instead of the electron. A full description takes all time orders and both carrier types into account.

The fascinating point about the double-resonant process is this: a different incoming photon energy (say, $i' \rightarrow a'$) leads to an excited electron with different momentum. To fulfill the second resonant transition a phonon with different momentum and energy is required for the second resonance. A larger incoming photon energy requires a larger phonon wavevector and – depending on the phonon dispersion – involves a higher or lower phonon energy. Scanning the incident photon energy thus corresponds to scanning the phonon energy in k-space. We will show this explicitly later in Fig. 53, where
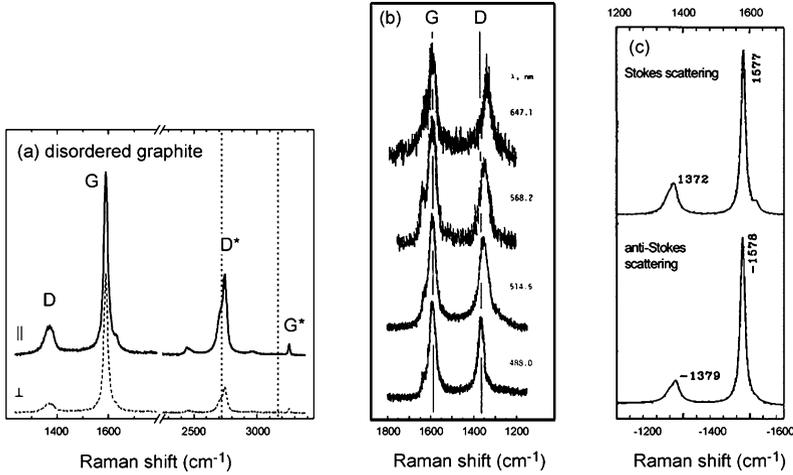
Fig. 37. (**a**) The Raman spectrum of a disordered graphite crystallite in parallel and crossed polarization of incident and scattered light. The defect-induced D mode, the Γ point or G mode, and their overtones D^* and G^*. From [125]. (**b**) Raman spectra excited at different excitation energies in the visible. Clearly seen is the curious shift of the D mode to higher energies for higher excitation energies. The G mode, in this sense, behaves like a "normal" excitation. After [210]. (**c**) Stokes and anti-Stokes spectra of the D and G mode with different frequencies for the D mode. After [211]

an experimental energy scan is compared to a calculated wavevector scan of an isolated nanotube.

The (approximate) phonon wavevector in a double-resonant process is related to the incoming photon energy. Neglecting the phonon energy compared to the much larger laser energy the double-resonant phonon wavevector may be approximated by $q = 2k_i$. This relationship is often used for a quick evaluation of the double-resonance conditions at different laser energies. For linear electronic bands, as is the case for graphite not too far from the Fermi level, (32) can be evaluated analytically, resulting in a linear relation between the incoming photon energy E_1 and phonon wavevector q, see [4]

$$q = \frac{E_1 - \hbar\omega_{\mathrm{ph}}(q)}{v_2} \quad \text{or} \quad \frac{E_1 - \hbar\omega_{\mathrm{ph}}(q)}{-v_1}, \tag{33}$$

where v_i are the Fermi velocities of the linear electronic bands. If the phonon energy is taken to depend on wavevector, (33) may be solved iteratively.

By scanning the incident laser energy it is thus possible to map the phonon frequencies in large parts of the Brillouin zone. Based on the double-resonant Raman interpretation *Reich* and *Thomsen* re-evaluated literature data on graphite and plotted them onto the phonon-dispersion curves [125] (see also Sect. 10.4 and [207]). The phonon dispersion of an isolated nanotube was
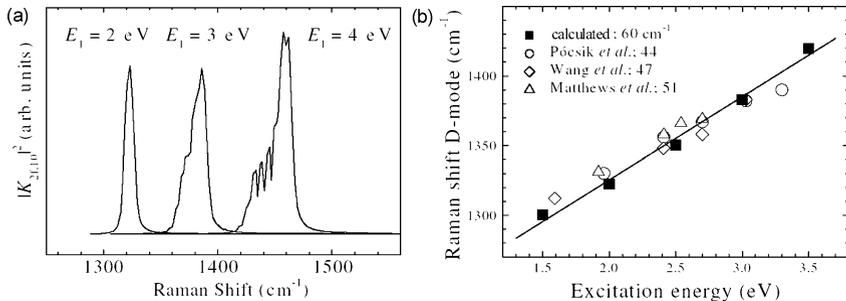
Fig. 38. (**a**) Calculated Raman spectra for the D mode in graphite for three different laser energies. (**b**) Calculated (*full squares*) and measured (*open symbols*) frequencies of the D mode as a function of excitation energy. From [4]; the measurements were taken from [215, 216] and [217]

measured and evaluated using this technique by *Maultzsch* et al. [129] (see Sect. 8.2).

Ge is another material where double resonance could explain an additional, excitation-energy dependent vibrational mode [212]. *Mowbray* et al. [213] invoked scattering by the surface as the process that conserved momentum in the double resonance. The essential evidence for this interpretation was the dependence of the observed Raman-frequency shifts on surface orientation. A detailed investigation of Raman double resonance in Ge was performed more recently by *Mohr* et al. [214].

We turn now to the double-resonant scattering process in graphite, which is closely related to that in carbon nanotubes. *Thomsen* and *Reich* first calculated the Raman spectra of the D mode using the concept of double resonances [4]. Their reason for re-examining the D mode was its curious and unresolved dependence on excitation energy. We show the characteristic features of the Raman spectrum of graphite in Fig. 37. The high-energy part of the spectrum is shown in Fig. 37a. The peak labeled D is a defect-induced mode – as *Tuinstra* and *Koenig* showed in a systematic study of graphite – and D^* its overtone. The shift with excitation energy reported by *Vidano* et al. is shown in Fig. 37b; it amounts to about $50\,\mathrm{cm}^{-1}/\mathrm{eV}$ [210, 215–217]. D^* shifts at twice the rate of D [218]. Finally, the D mode has different Stokes and anti-Stokes frequencies, see Fig. 37c, which is very unusual for Raman spectroscopy. In fact, it is impossible in first-order scattering.

The results of Thomsen and Reich, who based their interpretation on a double-resonant process, are reproduced in Fig. 38a and are the numerical evaluation of the Raman matrix element of (32). It is nicely seen that a Raman line appears by defect-induced resonances and shifts to higher frequencies when the excitation energy is increased. Figure 38b compares the experimental and theoretical frequency slopes showing an excellent agreement. The D^* mode is an overtone of the D peak where the electron is

backscattered by a second phonon instead of a defect. The differences between Stokes and anti-Stokes scattering arise because the double-resonant condition is slightly different for the creation and destruction of a phonon, see also the discussion in Sect. 10 and [125, 219].

There is an alternative approach to understand the appearance of the D mode and its excitation-energy dependence; it is based on the lattice dynamics of small aromatic molecules [220, 221]. In these molecules the D mode has a Raman-active eigenvector; its frequency depends on the actual size and shape of the molecule. The shift with excitation energy results from a resonant selection of a particular molecule by the incoming laser. For defect-induced scattering the solid-state approach presented above and the molecular approach can be shown to be the same. The latter fails, however, in explaining the D^* mode properties in perfect graphite. On the other hand, it has been argued [222] that double-resonant Raman scattering cannot explain why only one phonon branch shows strong double resonances. The selectivity of the process can be understood when considering the matrix elements in the Raman cross section (see [125, 207]).

The frequency difference between Stokes and anti-Stokes scattering was shown in Fig. 37c: the D mode in graphite differs by $\Delta\hbar\omega = 7\,\mathrm{cm}^{-1}$ [211]. In double resonance the resonance conditions differ for the creation and destruction of a phonon [4]. The double-resonance process shown in Fig. 36b is for Stokes scattering. We obtain an anti-Stokes process by inverting all arrows in the picture. This process is also double resonant, but at a different excitation energy $(i \rightarrow a)$ [219, 223]. In general, the Raman cross section for Stokes scattering K_S is the same as the cross section for anti-Stokes scattering K_aS if we interchange the incoming and outgoing photon (time inversion), i.e.,

$$K_\mathrm{aS}[E_2, \hbar\omega_\mathrm{aS}(E_1), E_1] = K_\mathrm{S}[E_1, \hbar\omega_\mathrm{S}(E_2), E_2]$$
$$= K_\mathrm{S}[E_1, \hbar\omega_\mathrm{S}(E_2), E_1 + \hbar\omega_\mathrm{aS}(E_1)]. \qquad (34)$$

In other words $\hbar\omega_\mathrm{aS}(E_1) = \hbar\omega_\mathrm{S}(E_2)$. Since we know the dependence of the Stokes frequency on excitation energy we can calculate the frequency difference

$$\Delta\hbar\omega = \hbar\omega_\mathrm{aS}(E_1) - \hbar\omega_\mathrm{S}(E_1) = \frac{\partial\hbar\omega_\mathrm{S}}{\partial E}\hbar\omega_\mathrm{aS}(E_1). \qquad (35)$$

Tan et al. [211] measured an anti-Stokes frequency of $1379\,\mathrm{cm}^{-1}$ and a D-mode slope of $43\,\mathrm{cm}^{-1}/\,\mathrm{eV}$. We predict $\Delta\hbar\omega = 7.4\,\mathrm{cm}^{-1}$ from (35), which is in excellent agreement with the reported value $(7\,\mathrm{cm}^{-1})$, see Fig. 37c. As discussed in [219] and [223] the frequency difference of Stokes and anti-Stokes scattering for the D^* overtone is predicted to be four times larger than for the D mode, because both the energy difference between E_1 and E_2 and the slope of the Raman peak with laser energy are doubled. This also agrees very well with the experimentally reported differences. In turn, (35) can be used to determine – at least approximately – the slope of a disorder band.
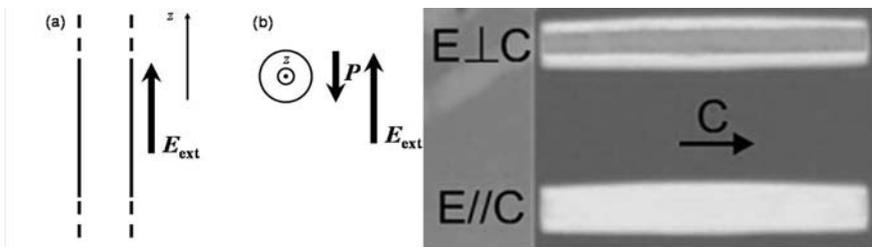
Fig. 39. Schematic of the shape depolarization in a nanotube. (**a**) An external field parallel to the nanotube axis will not induce any charge in a nanotube (except at ∞). (**b**) Fields perpendicular to the axis will induce charges in the walls and hence a perpendicular polarization that will tend to cancel the external field. Absorption is suppressed for $E \perp z$. From [20]. (**c**) Absortion of light polarized perpendicular (*upper*) and parallel (*lower*) to the nanotube axis, here for small tubes grown in the channels of a zeolite crystal. From [46]

6.4 Anisotropic Polarizability

The one-dimensional nature of carbon nanotubes affects their light-absorption properties.[6] Anisotropic polarizabilities in spheres and ellipsoids are treated in advanced textbooks, e.g., in [224], and nanotubes constitute a limiting case of these treatments. The effect of the shape anisotropy has to be taken into account when discussing the optical properties of nanotubes. In the direction parallel to the tube axis there is charge build up only at the ends of a nanotube (at $\pm\infty$). In the static limit this has no effect on the absorption. Perpendicular to the axis, as *Ajiki* and *Ando* pointed out [166], the induced polarization will reduce the external field (see Fig. 39).

The effect of the anisotropic polarizability on light absorption was studied in detail by several authors [166, 225, 226]. The essence is that in one-dimensional systems – like the single-walled carbon nanotubes – there is practically no absorption for polarizations perpendicular to the nanotubes axis. For multiwalled tubes the effect of anisotropic polarizability becomes smaller as the shape of the nanotubes becomes more isotropic. *Benedict* et al. [225] derived the following expression for the diameter dependence of the depolarization effect, i.e., the screened polarizability per unit length of a cylinder is

$$\alpha_\perp(\omega) = \frac{\alpha_{0,\perp}(\omega)}{1 + 8\alpha_{0,\perp}(\omega)/d^2} \,, \tag{36}$$

where d is the diameter of the cylinder, and $\alpha_{0,\perp}$ is the unscreened polarizability. See also *Tasaki* et al. [226] for a description at optical frequencies, or [20] for more details. Figure 39c shows an experimental verification of the depolarization effect in aligned nanotubes (within a zeolite crystal). For light

---

[6] In the carbon nanotube literature this is sometimes called the *antenna effect.*
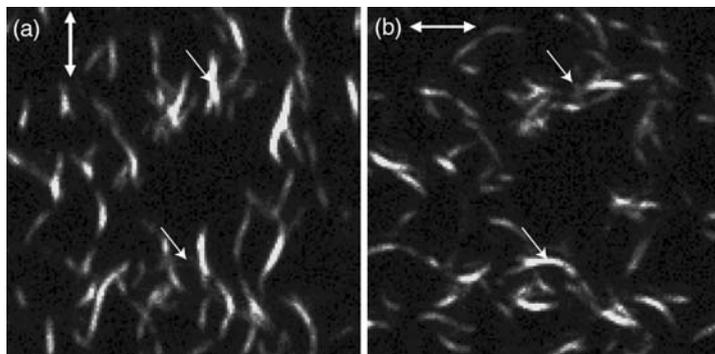
Fig. 40. The depolarization effect in bundles of single-walled nanotubes recorded on an area of $15 \times 15\,\mu$m. The polarizations of incident and scattered light in (**a**) and (**b**) are along the direction of the *double arrow*. The intensity shown is the integrated signal of the D^* mode at 2615 cm, the overtone of a defect-induced mode (Sect. 10.3). The *single arrows* highlight nanotube bundles parallel and perpendicular to the light polarizations. Raman scattering is completely suppressed for light perpendicular to the nanotube axis. From *Hartschuh* et al. [229]

polarized perpendicular to the nanotube's axes the sample is transparent (upper picture); for parallel polarization it is completely black.

The influence of the anisotropic polarizability is seen also in the Raman spectra. Since the absorption and emission of light is nearly zero for perpendicular polarization, only the zz component of the Raman tensor gives rise to scattering. This was observed in many experimental studies [99, 101, 147, 227, 228]. We show a nice confirmation in Fig. 40, where the Raman spectra of several bundles of carbon nanotubes were spatially resolved by a confocal Raman arrangement [229]. Nanotubes aligned with the light polarization are seen as bright short lines in the figure. Part (b) is taken on the same small area of the sample as part (a), but the polarization of the incoming light is rotated by 90°. Now other tubes light up. Tubes at a finite angle to the polarization show up in both panels.

An important consequence of the depolarization effect is that only $A_{1(g)}$ phonons have a reasonably strong Raman signal, because they are the only modes with nonzero zz component in the Raman tensor in the nanotube point groups (see Table 3.1). When modeling the Raman spectrum of single-walled carbon nanotubes, one of the challenges is to explain the complex spectrum on the basis of totally symmetric phonons alone [194, 230].

A nice example of where the Raman depolarization ratio of a spherical molecule is affected by the anisotropic polarizability of the nanotube was shown by *Pfeiffer* et al. [232] in peapods. Peapods are C_{60} molecules embedded in carbon nanotubes, see Sect. 2 for a TEM image and Fig. 41 for a Raman spectrum. The depolarization ratios, the ratio of the Raman intensity of a peak in perpendicular and parallel polarization in ran-
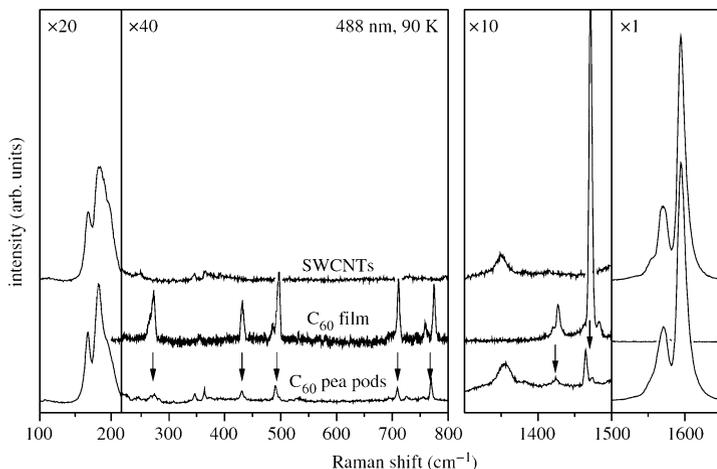
Fig. 41. (*upper*) Raman spectra of single-walled carbon nanotubes, (*middle*) of a C_{60} film, and (*lower*) of C_{60} peapods. The peapods, which are nanotubes containing C_{60} molecules, show a superposition of the spectra of the upper and middle traces. The *arrows* highlight the C_{60}-peak positions in the peapod. After [231]

domly oriented scatterers, is characteristic of the symmetry of a molecule or solid. For example, the two fully symmetric A_{1g} modes of polycrystalline C_{60} at $494\,cm^{-1}$ and $1469\,cm^{-1}$ have depolarization ratios of ≈ 0.1 at room temperature [232, 233]. For $\alpha_{xx} = \alpha_{yy} = \alpha_{zz} \neq 0$ and all other $\alpha_{ij} = 0$, the depolarization ratio should be zero. In a peapod, however, only the z component of the incident light "sees" the C_{60} molecule (z is along the nanotube axis). The other components are completely screened. For the Raman-scattering tensors of C_{60} this implies that only the zz components are effectively nonzero. The depolarization ratio of an A_{1g} tensor with only $\alpha_{zz} \neq 0$ is equal to 1/3. A depolarization ratio of 1/3 was indeed observed experimentally for the peapods [232], confirming the importance of the anisotropy of the polarizability. See, e.g., the books by *Hayes* and *Loudon* [234] or *Reich* et al. [20] how to obtain depolarization ratios for a given Raman tensor.

The depolarization effect was recently found in nanotubes of WS_2 (see Fig. 42 [235]). The intensity of the observed Raman signal of WS_2 is plotted as a function of angle in the polar plot Fig. 42b. The observed Raman frequencies in the nanotube were the same as in bulk WS_2 to within experimental error because the nanotubes were rather thick (compared to the usual carbon nanotubes), $d(WS_2) \approx 20\,nm$. However, the Raman intensities of both the mode at $351\,cm^{-1}$ and $417\,cm^{-1}$ followed the expected angular dependence for the anisotropic polarizability in nanotubes. For light polarized along the tube axis, the modes were strong, perpendicular to it they nearly disappeared, see Fig. 42b, where we plot the intensity as a function of angle between the polarization and the WS_2 nanotube axis.
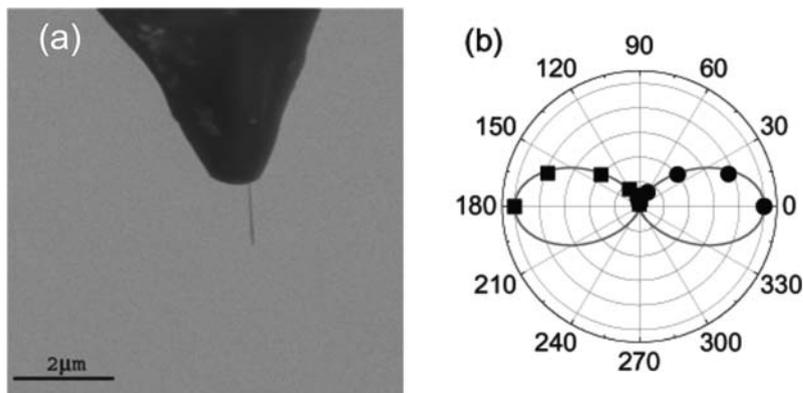
Fig. 42. (**a**) A free-standing WS_2 nanotube mounted on an AFM tip. (**b**) The anisotropic polarizability of the nanotube is observed in the intensity of the two Raman modes at $351\,\mathrm{cm}^{-1}$ (*circles*) and $417\,\mathrm{cm}^{-1}$ (*squares*) of the nanotube in (**a**). For clarity, the two modes are plotted in different quadrants; $0°$ and $180°$ correspond to light polarized parallel to the axis of the nanotube. After [235]

7 Assignment

Identifying the chirality of a particular nanotube or set of nanotubes has been an issue in the literature ever since the discovery of nanotubes. While it is possible to do so with electron microscopy and with scanning tunneling spectroscopy [164, 165] both techniques are rather time consuming and difficult to do without major sample manipulation. Using Raman spectroscopy, and the radial-breathing mode in particular, there have been many attempts to use the relationship between inverse diameter and the breathing-mode frequency (5) to determine the chiral index of a tube [47, 115, 236]. First, the ω_{RBM} is measured with high accuracy and then, taking your favourite constants c_1 and c_2, the diameter of a nanotube is calculated. The difficulties with this procedure lie in considerable uncertainties in c_1 and c_2 and the comparatively many different chiralities in even a small diameter range of a typical sample. Attempts to correlate the radial-breathing mode frequencies with the Raman excitation energy, in principle, improved the quality of such an assignment [236]. However, using the simple tight-binding expression for the electronic energies, as was done, e.g., in [115, 236], is not sufficient to identify a particular nanotube, in spite of persistent attempts to do so in the literature. We consider such assignments unreliable because they imply an unrealistic absolute accuracy of the calculated electronic energies [115, 116, 205, 236, 237].

Substantial progress in a Raman-based chirality assignment was only made after *Bachilo* et al. published their two-dimensional plot of excitation vs. luminescence energy of nanotubes. The tubes were wrapped by sodium dodecyl sulfate (SDS) molecules and thus unbundled in the solution [59]. *Bachilo* et al. were the first to observe luminescence from many nanotubes,
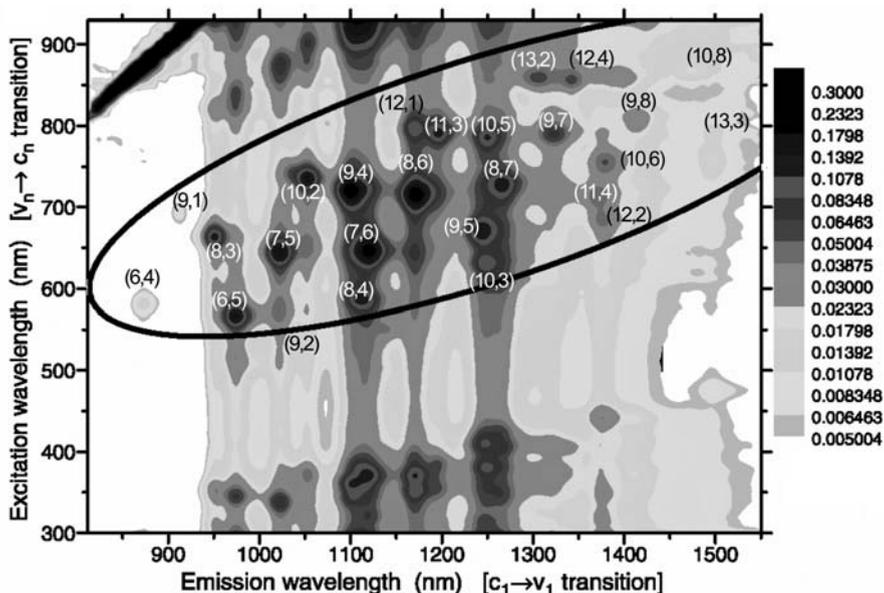
Fig. 43. Two-dimensional plot of the luminescence intensity (x-axis) of individual carbon nanotubes in solution as a function of excitation energy (y-axis). A cut parallel to x is a single luminescence spectrum, one parallel to y is a photoluminescence excitation or absorption spectrum. Every chirality corresponds to a single point in this plot. The assignment is indicated by (n_1, n_2). After [60]

and they showed that from the luminescence maxima observed in such a plot, a pattern related to the Kataura plot could be identified [60]. They still needed a least-square fit to "anchor" their experiment to theory and could not investigate metallic nanotubes, but the essential path to identifying individual chiral indices was found.

In the two-dimensional plot of *Bachilo* et al. (Fig. 43) it became possible to investigate simultaneously the second (or higher) optical transition of carbon nanotubes and their lowest excitation above the ground state.[7] The excitation energy is plotted on the y-axis and a horizontal line corresponds to a luminescence spectrum excited at one particular excitation energy. Maxima along the y-direction of the plot occur at energies where the absorption – as given by the intensity of the photoluminescence – is maximal. In addition to seeing the luminescence from individual nanotubes the result prompted a discussion about the ratio of E_{22} to E_{11} (or eh_{22} to eh_{11}), which turned out to be $\neq 2$ in the large-diameter limit as one expects for uncorrelated

---

[7] These transitions were generally identified as energies between the van-Hove singularities E_{ii}. In view of the experimental and theoretical progress concerning the importance of excitonic energies these should be rather referred to eh_{ii}, see Sect. 5.3.
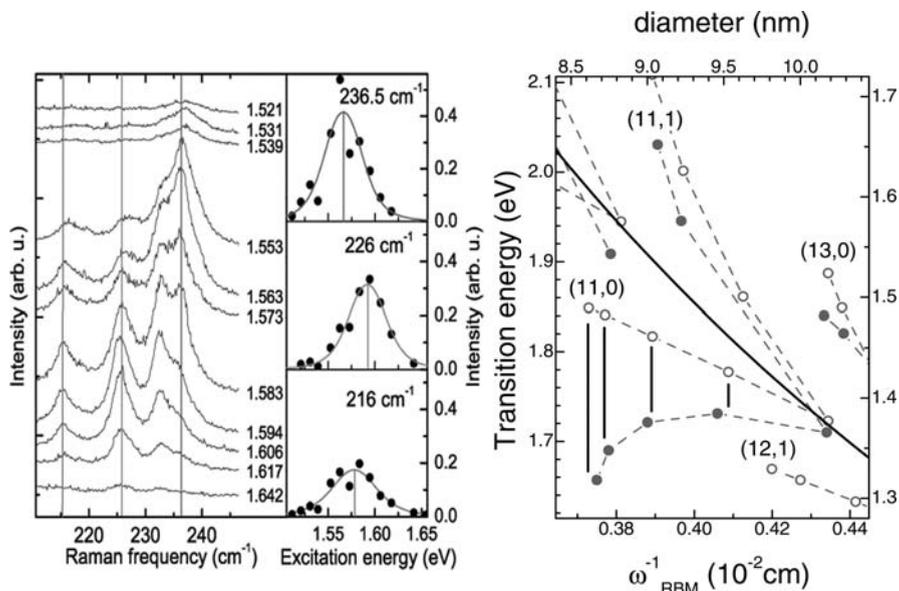
Fig. 44. (*left*) Resonant Raman spectra of a solution of sodium dodecyl sulfate wrapped around carbon nanotubes. Shown is a narrow interval of excitation energies with several radial-breathing mode peaks going in and out of resonance. Resonance profiles extracted along the *vertical lines* on the *left*; the maxima occur at different energies. (*right*) Resonance energies of the (11,0) branch, experimental (*closed symbols*) and theory (*open*). The vertical alignment, i.e., the diameter to ω_{RBM} relationship is nearly perfectly matched. For a larger range of diameters, see Fig. 46. After [242]

electrons and holes (band-to-band transitions). The so-called *ratio problem* was discussed by a number of authors, see, e.g., [20, 60, 74, 161, 174, 238, 239], and we refer the reader to the literature about this topic.

A step beyond the two-dimensional luminescence graph was made by plotting the Raman spectra as a function of excitation energy [63–65, 111, 240–242]. The y-axis corresponds again to the transition energies. However, instead of plotting the Raman spectra straight along the x-axis, ω_{RBM} is converted to nanotube diameter using (5). Now the data are in the form of the well-known Kataura plot (Fig. 26). The essence of the two-dimensional Raman plot lies in the fact that both electronic transitions (through Raman resonances E_{ii}) and vibrational properties (through the radial-breathing mode frequency ω_{RBM}) depend on chirality and are measured simultaneously. An assignment of chiralities may be obtained from such a plot without any prior assumptions about c_1 and c_2, as we will show in the following. Such a plot is obtained by using a variety of discrete and tunable laser sources with energies separated by less than the width of a typical excitation, say about $10\,\mathrm{meV}$.
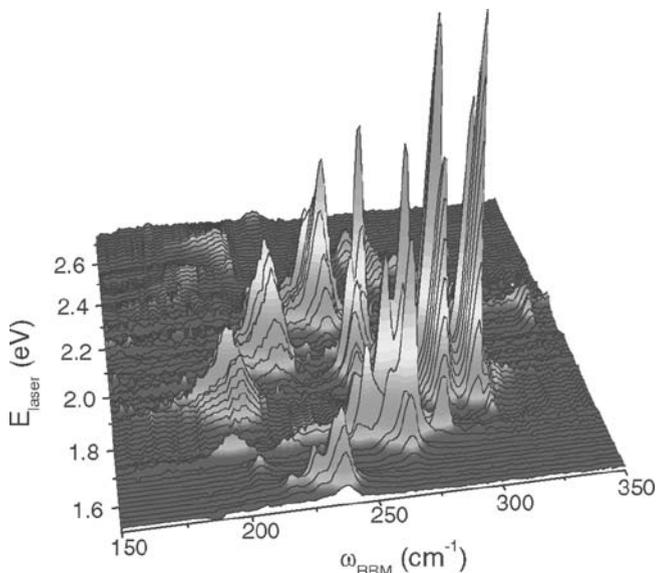
Fig. 45. Two-dimensional plot of the radial-breathing-mode range vs. laser excitation energy. Note the various la-ola-like resonance enhancements, from which we can determine both the optical transition energies and the approximate diameter of the nanotubes. The spectra were each calibrated against the Raman spectrum of CCl_4. From [64]

In Fig. 44 (left) we show the resonance profiles of several nanotubes with nearby resonance maxima. The largest intensity is seen to move through the peaks forming what looks like a *la-ola* wave [243]. There are several such la-ola-type resonances when exciting the nanotubes with different laser lines, each occurring over a fairly narrow energy and ω_{RBM} range. As we will see, each la-ola series of resonances corresponds to a particular branch in the Kataura plot of transition energies versus diameter. Within each branch the fixed relationship between the indices – n_1 decreases by one and n_2 increases by 2 as long as $n_1 > n_2$ – gives a fixed assignment once a particular branch is identified (see Table 2 for the definition of a branch). The tube with a smallest diameter in a branch is always a zigzag or near-zigzag tube, the one with the largest diameter an armchair or near-armchair one. (See Sects. 2 and 5.2 for more details.)

Figure 45 shows the two-dimensional resonance Raman plot where many of the branches can be seen, their intensity is plotted in the third direction. (Here, ω_{RBM} and not $1/d$ is plotted.) Each small group of peaks corresponds to one branch of the Kataura plot (Figs. 26 and 44).

We are now able to perform an (n_1, n_2) assignment. This is done by stretching and shifting the theoretical Kataura plot with respect to the experimental one [63, 242].
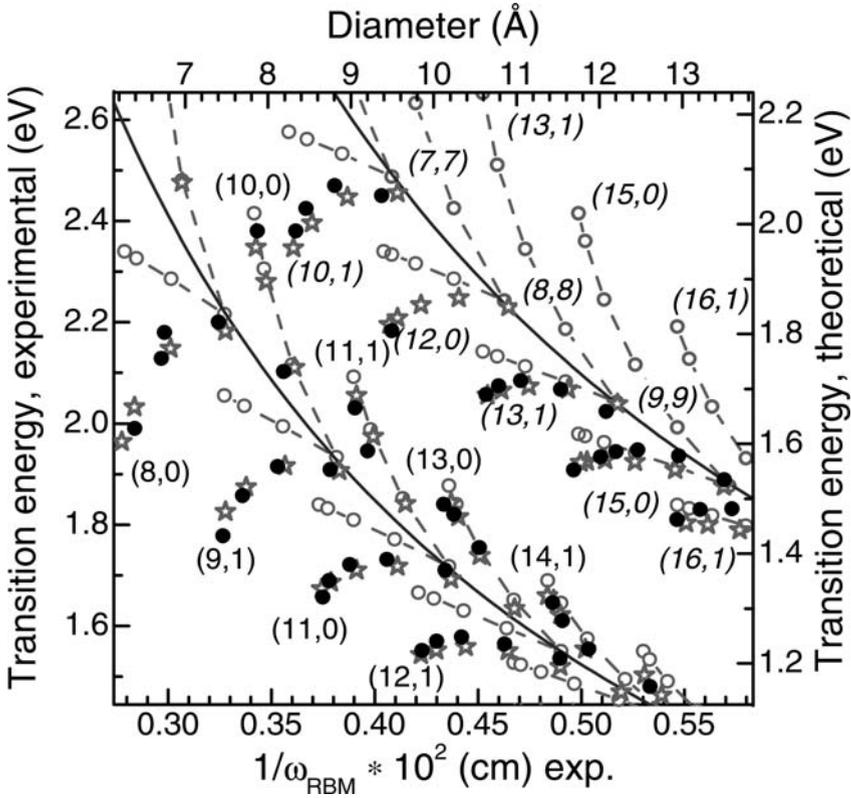
Fig. 46. Experimental Kataura plot. Shown is the part of the full plot (Fig. 26) where experimental data are available from a sample with isolated, SDS-wrapped nanotubes in solution. The two *solid* $1/d$ *lines* are the E_{22}^S and E_{11}^M average diameter dependence (isotropic approximation of the graphite band structure). The *open symbols* are calculated transition energies from a tight-binding approximation [6] (*circles*) and the empirical expressions (38) and (39) (*stars*) [242], which describe the transition energies rather well. *Closed circles* refer to experimental data points. The chiral index labels refer to the tube with largest chiral angle within a branch (zigzag or near-zigzag tubes). The index of neighboring tubes may be obtained from the $(n'_1, n'_2) = (n_1 - 1, n_2 + 2)$ rule (22), the branch index is obtained from $\beta = 2n_1 + n_2$ (21); armchair tubes lie on the $1/d$ line and are labeled as well. See also Table 2. Note that the branch index is the same in the upper and lower branches of the metallic tubes, whereas it differs in semiconducting tubes. Metallic nanotubes thus have two close-by optical transitions [150]. The region of the (11,0) branch is enlarged in Fig. 44 (*right*). After *Telg* et al. [63]

What is the physical meaning of such stretching and shifting? Along the
x-axis it means changing the constants c_1 and c_2, respectively, as can be seen
in (5). Along the y-axis it means adjusting the electronic energies between
experiment and theory, a simple shift corresponds to a scissors operator. It
is important to note that bringing theory and experiment into coincidence
is not a fit of experiment to theory in the usual sense. Instead the best
match relies on recognizing the patterns of the branches and families in such
a plot. The stringent criterion is that in the vertical direction there is a full
correspondence between theory and experiment as in Fig. 44 (right). We
mean by this, e.g., that the x-axis cannot be shifted by just a little, say one
diameter difference of neighboring tubes. For example, were we to shift the
assignment such that the experimental (11,0) branch in Fig. 44 (right) were
to lie a little more to the left, the outermost tube [the (11,0)] would no longer
have a theoretical counterpart. Such a small shift corresponds to a change
of $\Delta c_1 \approx 2.5\,\mathrm{cm}^{-1} \cdot \mathrm{nm}$ in (5). As the theoretical Kataura plot, however, is
exhaustive (all possible combinations of n_1 and n_2 are contained in the plot)
such a shift invalidates the overall pattern and is impossible [63, 242].

What about shifting the experiment by one entire branch? Take, e.g.,
all experimental values to smaller diameters so that the (11,0) ends up at
a diameter of 7.5 Å, the value of the (9,1) in Fig. 46. Then one would find
for the (9,1) branch more observed chiral indices, namely five, than exist for
this branch, namely four [242] (see also Fig. 3). Again this is impossible, and
so is this assignment, which corresponds to $\Delta c_1 \approx 30\,\mathrm{cm}^{-1} \cdot \mathrm{nm}$, i.e., a 15 %
decrease in c_1.

Note also that the diameter difference between neighboring tubes is not
constant. For instance, $d[(11,0)] = 8.6$ Å and $d[(10,2)] = 8.7$ Å, whereas the
next tube in the same branch is at a larger separation, $d[(9,4)] = 9.0$ Å.
These subtle differences are observed in the experiment as well. In fact, for
the four branches with the smallest tubes (10,1), (11,0), (12,1) and (13,1) we
observed all possible nanotubes and diameter–distance irregularities putting
our assignment on firm ground [63, 242]. In Table 10 we list, for about 50 nano-
tubes, the RBM frequencies and optical transition energies together with d,
Θ, the family ν, the branch index β, and the magnitude squared of the ex-
perimental Raman susceptibility of a set of HiPCo-grown nanotubes. The
susceptibility values were obtained by correcting the Raman intensity for
the spectrometer response and ω^4 but not for the distribution of nanotube
chiralities in the sample.

Table 10: RBM frequency ω_{RBM} and optical transition energies E_{ii} for 47 single-walled carbon nanotubes. The table lists, additionally, the tube diameter d, the chiral angle Θ, the nanotube family $\nu = (n_1 - n_2)$ mod 3, and the Kataura branch $\beta = 2n_1 + n_2$ of each nanotube. The last column gives the square of the Raman susceptibility of a HiPCo-grown sample in arbitrary units (RS^2). The transition energies E_{ii} are the second transition for semi-conducting tubes S–E_{22} ($\nu = \pm 1$) and the first transition for metallic ($\nu = 0$) tubes M–E_{11} (see Fig. 26). Data from [63, 242]

Tube	ω_{RBM} (cm^{-1})	E_{ii} (eV)	d (Å)	Θ (°)	ν	β	RS^2
$(14, 5)$	174.5	1.83	13.36	14.7	0	33	1.9
$(10, 10)$	175.7	1.889	13.57	30.0	0	30	0.9
$(15, 3)$	179.0	1.83	13.08	8.9	0	33	1.8
$(16, 1)$	182.0	1.81	12.94	3.0	0	33	0.5
$(11, 8)$	182.7	1.936	12.94	24.8	0	30	1.9
$(12, 6)$	189.6	1.948	12.44	19.1	0	30	1.9
$(13, 4)$	195.3	1.944	12.06	13.0	0	30	2.5
$(9, 9)$	195.3	2.02	12.21	30.0	0	27	0.5
$(14, 2)$	196.3	1.934	11.83	6.6	-1	29	3.6
$(12, 5)$	198.5	1.554	11.85	16.6	-1	29	0.1
$(15, 0)$	201.5	1.908	11.75	0.0	0	30	0.7
$(13, 3)$	203.3	1.610	11.54	10.2	-1	29	0.6
$(10, 7)$	204.0	2.067	11.59	24.2	0	27	0.9
$(9, 8)$	204.0	1.535	11.54	28.1	$+1$	26	0.5
$(14, 1)$	205.8	1.646	11.38	3.4	-1	29	0.3
$(11, 5)$	212.4	2.084	11.11	17.8	0	27	1.7
$(9, 7)$	216.0	1.564	10.88	25.9	-1	25	1.3
$(12, 3)$	217.4	2.075	10.77	10.9	0	27	2.6
$(13, 1)$	220.3	2.057	10.60	3.7	0	27	1.5
$(11, 4)$	221.8	1.76	10.54	14.9	$+1$	26	
$(10, 5)$	226.1	1.578	10.36	19.1	-1	25	2.3
$(12, 2)$	228.1	1.82	10.27	7.6	$+1$	26	12.2
$(8, 7)$	230.4	1.710	10.18	27.8	$+1$	23	0.4
$(13, 0)$	230.8	1.84	10.18	0.0	$+1$	26	0.2
$(11, 3)$	232.6	1.570	10.00	11.7	-1	25	2.0
$(12, 1)$	236.4	1.551	9.82	4.0	-1	25	4.1
$(12, 0)$	244.9	2.18	9.40	0.0	0	24	

Table 10: continued

Tube	ω_{RBM} (cm^{-1})	E_{ii} (eV)	d (Å)	Θ (°)	ν	β	RS^2
$(8,6)$	246.4	1.73	9.53	25.3	-1	22	1.4
$(7,7)$	247.8	2.45	9.50	30	0	21	
$(10,3)$	252.1	1.945	9.24	12.7	$+1$	23	3.6
$(11,1)$	256.0	2.031	9.03	4.3	$+1$	23	9.8
$(9,4)$	257.5	1.72	9.03	17.5	-1	22	2.5
$(8,5)$	262.7	2.47	8.90	22.4	0	21	
$(7,6)$	264.2	1.909	8.83	27.5	$+1$	20	2.6
$(10,2)$	264.6	1.690	8.72	8.9	-1	22	2.3
$(11,0)$	266.7	1.657	8.62	0.0	-1	22	1.7
$(9,3)$	272.7	2.43	8.47	13.9	0	21	
$(10,1)$	276.3	2.38	8.25	4.7	0	21	
$(8,4)$	280.9	2.10	8.29	19.1	$+1$	20	0.3
$(7,5)$	283.3	1.915	8.18	24.5	-1	19	18.3
$(10,0)$	291.4	2.38	7.83	0.0	$+1$	20	
$(8,3)$	297.5	1.857	7.72	15.3	-1	19	35.8
$(7,4)$	305.4	2.63	7.55	21.1	0	18	
$(9,1)$	306.2	1.78	7.47	5.2	-1	19	9.1
$(6,5)$	308.6	2.20	7.47	27.0	$+1$	17	
$(8,2)$	315.5	2.52	7.18	10.9	0	18	
$(8,0)$	352.2	1.99	6.27	0.0	-1	16	0.1

From a least-square fit of our so-assigned nanotubes it is possible to find an experimental value for the constants c_1 and c_2 in (5)

$$\omega_{\mathrm{RBM}} = \frac{(215 \pm 2)\,\mathrm{cm}^{-1} \cdot \mathrm{nm}}{d} + 18\,\mathrm{cm}^{-1}. \tag{37}$$

We stress, however, that the precise values of these constants are not critically important in view of the concept of families and, in particular, branches introduced. Nanotubes within the same branch have similar physical properties. Small variations, e.g., in c_2 due to environmental effects on the nanotubes, may be sample specific. *Fantini* et al. [64], who performed a related study fitted separately metallic ($c_1 = 218\,\mathrm{cm}^{-1} \cdot \mathrm{nm}$, $c_2 = 10\,\mathrm{cm}^{-1}$) and semiconducting ($223\,\mathrm{cm}^{-1} \cdot \mathrm{nm}$, $17\,\mathrm{cm}^{-1}$) tubes to (5), which is slightly different from the values in (37). Nevertheless, their most recent assignment of RBM peaks to nanotube chiralities agrees with the one presented here. Note also that we
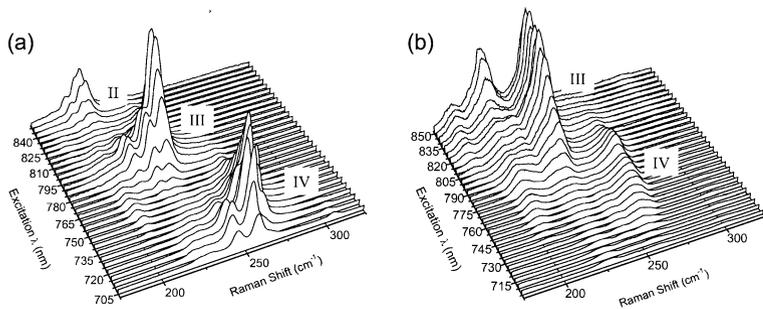
Fig. 47. Raman spectra of (**a**) individual nanotubes in solution and (**b**) ropes of nanotubes. From *O'Connell* et al. [245]

directly assigned a Raman peak to a nanotube chirality (n_1, n_2). We did not make use of (37) or similar relations to find the assignment in Table 10.

The typical bundling of nanotubes presents a form of environmental influence on the RBM spectra. Both transition energies and radial-breathing mode frequencies are shifted by the van-der-Waals interaction [244]. Predictions by *Reich* et al. based on ab-initio calculations of bundles showed that we should expect a shift of the electronic energies and observe a dispersion perpendicular to the nanotube axis [9]. With data based on the idea of an experimental Kataura plot, *O'Connell* et al. [245] recently showed that this is indeed the case. In Fig. 47 we reproduce part of their data. Figure 47a shows a sample of carbon nanotubes in solution, and three sets of la-ola (labeled II, III, and IV) are easily identified. For the same sample in bundled form, Fig. 47b shows the corresponding spectra. All three resonances have shifted down in transition energy upon bundling, their ω_{RBM} stay approximately the same. This is consistent with the prediction of *Reich* et al. [9] and confirms the concept and importance of the experimental Kataura plot.

While the experimental radial-breathing frequencies in Fig. 46 match theory nearly perfectly, there are systematic deviations of the transition energies from the tight-binding transition energies, see also right panel in Fig. 44. Within each branch – in particular for the -1 branch of E_{22} – the energies fall below the theoretical ones, the more so the smaller the chiral angle. In other words, the more "zigzag"-type the nanotube is, the less its electronic transition energies are described by zone folding the graphite ab-initio band structure, which is the basis for the theoretical points in Fig. 46. Furthermore, the more the (near-) zigzag nanotubes drop from the theoretical values, the smaller their diameter. Apparently, this is an effect of the increasing curvature on the band structure, which also affects the excitonic energies increasingly. Several authors have attempted to describe the curvature effect by empirical formulas [7, 60, 65, 111, 242, 246, 247]. They essentially agree in that they include a chirality-dependent correction, which increases with smaller diameter.

We show here an empirical formula parameterized by a fit to the data in Fig. 46 by *Maultzsch* et al. [242]. These are for the E_{22}^S transition of semi-conducting tubes

$$E_{22}^S = 4\gamma_0 \frac{a_{C-C}}{d} \left(1 + \gamma_1 \frac{a_{C-C}}{4d}\right) + \nu\gamma_2 \frac{a_{C-C}^2}{d^2} \cos 3\Theta \,, \tag{38}$$

with the parameters $\gamma_0 = 3.53$ eV, $\gamma_1 = -4.32$, $\gamma_2 = 8.81$ eV, the family index ν, the diameter d of the nanotube, and the carbon–carbon distance of graphene $a_{C-C} = \sqrt{3}a_0 = 1.421$ Å. For the first set of metallic E_{11}^M transitions

$$E_{11}^M = 6\gamma_0 \frac{a_{C-C}}{d} \left(1 + \gamma_1 \frac{a_{C-C}}{6d}\right) - \gamma_2 \frac{a_{C-C}^2}{d^2} \cos 3\Theta \,, \tag{39}$$

with the parameters $\gamma_0 = 3.60$ eV, $\gamma_1 = -9.65$, and $\gamma_2 = 11.7$ eV. When applying the empirical expressions to find the transition energy of a particular nanotube, d, ν, and Θ are computed from the chiral index of the nanotube (see Table 2).

Expressions (38) and (39) are quite useful; together with (37) they describe the position of a large number of nanotubes in the Kataura plot. Conversely, if ω_{RBM} and the approximate transition energy are known from a Raman measurement, the branch and the chiral index of a nanotube can be easily identified.

We describe now how one can, without an indepth understanding of the physics behind the idea, identify the chiral index of a nanotube or a set of nanotubes by going through the following steps.

– Identify the average diameter range of nanotubes you have; often this will depend on the method used to grow your tubes.
– Draw a vertical line in the experimental Kataura plot at your average diameter. You may take an existing plot like the one in Fig. 46, or generate one with an empirical formula, e.g., (38) and (39).
– Take a Raman spectrum with an excitation energy that runs through a branch with nanotubes that have your average diameter. This may be a branch belonging to any E_{ii}; choose one where you have a laser energy for excitation available in your lab.
– In your spectra, look at the region of expected ω_{RBM} and identify the branch, which may look like the resonance in Fig. 44 or like the one in Fig. 48. Several branches of tubes may appear in the spectra.
– Identify the maxima and use either Table 10 directly, or identify the highest ω_{RBM} within the la-ola and, using the simple $(n_1 - 1, n_2 + 2)$ rule (22), find the index for the peaks in the la-ola. (See also Sects. 2 and 5.2.)
– If in doubt, take a second laser line slightly shifted from your first. From the relative changes in intensity try to find out on which side of the la-ola you are on. This will give you additional confidence in your assignment.
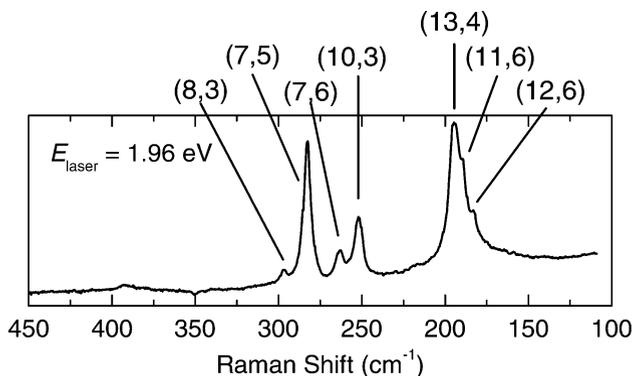
Fig. 48. Raman spectrum at E_{exc} = 1.96 eV, an energy chosen specifically to identify the chirality of individual nanotubes; see text for details. After *Maultzsch* et al. [242]

In principle, if your tubes are in a different environment (different solution, wrapping, substrate, etc.) the Kataura plot may be shifted slightly as a whole. This concerns both Kataura axes, i.e., the constants c_1 and c_2 may change or the precise position of the electronic transition energies and the plot could shift up or down slightly. We can get an idea of how little the transition energies shift from studies using either sodium dodecyl sulfate (SDS) or sodium dodecylbenzene sulfonate (SDBS) surfactants as solvent for the same type of tubes [242], where the maximal shift observed was about 10 meV. The frequency of the radial-breathing modes did not change within the experimental error. We emphasize that for the assigment these effects are expected to play a minor role, only. Once an entire branch is identified, the highest ω_{RBM} frequency is the one closest to the zigzag direction (see Sect. 5.2). Identifying a branch can be accomplished with a single suitably chosen excitation energy.

8 Metallic and Semiconducting Nanotubes

Metallic nanotubes – one third of all nanotubes in a random ensemble of nanotubes – are of special interest for applications as thin wires. They are not detectable by luminescence, and identifying them poses a challenge to Raman spectroscopy. To the extent that a full experimental Kataura map for a set of samples has become available (Sect. 7), the identification of metallic nanotubes, of course, is not an issue any longer. Given n_1 and n_2, if their difference is divisible by 3, a nanotube is metallic (see Sect. 2). Or, in other words, for one laser excitation energy metallic tubes have different diameters from semiconducting tubes. Based on the frequency of the radial-breathing mode a distinction becomes easily possible.
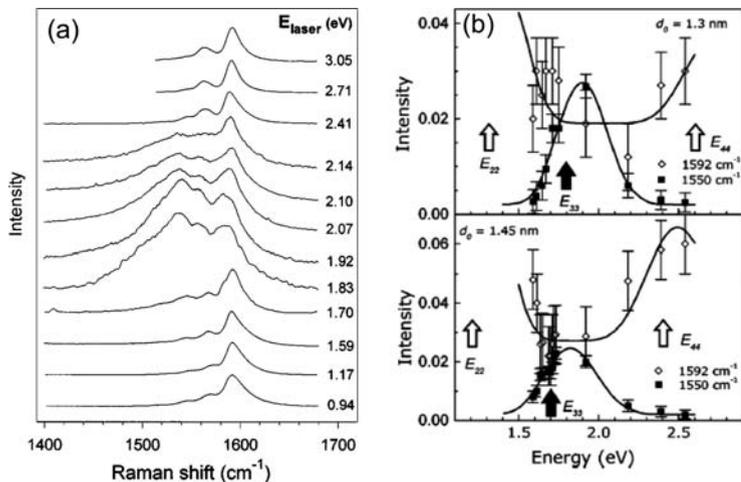
Fig. 49. (**a**) Resonant Raman spectra of the high-energy mode between 1 eV and 3 eV excitation energy. The strong enhancement of the mode at $\approx 1540\,\mathrm{cm}^{-1}$ at an excitation energy near 2 eV is clearly seen. After [188]. (**b**) Resonant Raman-excitation profiles from metallic (*open symbols*) and semiconducting (*closed symbols*) nanotubes. The *lines* are fits to (40). The *upper panel* refers to smaller-diameter nanotubes, the *lower* one to tubes with larger diameter. After [168]

8.1 Phonon–Plasmon Coupled Modes

Before the availability of isolated single-walled carbon nanotubes, one focus of Raman spectroscopy has been the shape of the high-energy mode, which appears very different in metallic and semiconducting nanotubes. The essential observation was that the shape of the high-energy peak changed at an excitation energy believed to match optical transitions in metallic nanotubes, enhancing those tubes systematically [188]. We show in Fig. 49 how a peak at $\approx 1540\,\mathrm{cm}^{-1}$ dominates the spectra at an excitation energy of 1.8 eV to 1.9 eV, while it nearly disappears at higher and at lower excitation energies. This peak, which had already been seen in an earlier paper [187], was interpreted as being due to an enhancement of optical transitions in the region of metallic tubes [188]. Because of the $1/d$ dependence of the electronic transition energies this "metallic resonance" should depend on the average diameter of the nanotube. Indeed it was shown that the resonance energies E_{ii} shift to larger energies for smaller nanotubes [168], see Fig. 49b. This analysis takes into account the average diameter d_0, the diameter distribution σ, considers δ-functions for the resonant transitions in every distinct nanotube chirality, and assumes constant Raman matrix elements when calculating the
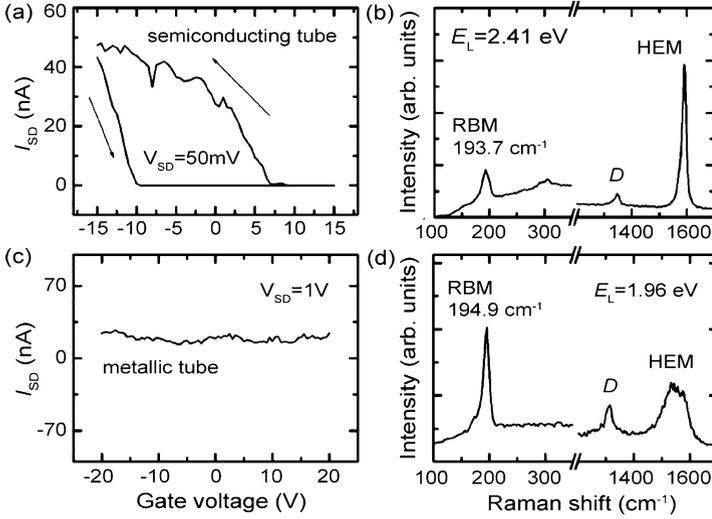
Fig. 50. Combined electric transport and Raman measurements on a single tube. (**a**) Transport characteristic of a semiconducting nanotube; (**b**) Raman spectrum of the tube in (**a**) showing the RBM, a weak D mode and a sharp Lorentzian-like high-energy mode. (**c**) Transport characteristic of a metallic nanotube; (**d**) Raman spectrum of the tube in (**c**) showing the RBM, a stronger D mode and a broadened asymmetric high-energy mode. This is the characteristic spectrum of a metallic tube. We thank R. Krupke for providing this figure

Raman intensity I as a function of the laser excitation energy $\hbar\omega_{\mathrm{exc}}$ according to

$$I(\hbar\omega_{\mathrm{exc}}) = \sum_d \frac{1}{d^2} \frac{Ae^{-\frac{1}{2}[(d-d_0)/\sigma)]^2}}{[(E_{ii} - \hbar\omega_{\mathrm{exc}})^2 + \hbar^2\gamma^2][(E_{ii} - \hbar\omega_{\mathrm{exc}} + \hbar\omega_{\mathrm{ph}})^2 + \hbar^2\gamma^2]}.$$

(40)

The phonon energy used in the fit to data presented in Fig. 49b was 0.199 eV (semiconducting) and 0.196 eV (metallic nanotubes), resulting in energies of 1.2 eV and 1.3 eV for the second semiconducting transition and 2.4 eV and 2.6 eV for the third semiconducting transition. The transition energies for metallic nanotubes were at 1.8 eV and 1.9 eV in the two sets of tubes. The first value refers to the nanotubes with larger average diameter ($d_0 = 1.45\,\mathrm{nm}$), the second to those with smaller diameter ($1.3\,\mathrm{nm}$) [168]. Note that this analysis did not take into account excitonic effects, which are less important for nanotube bundles.

An independent proof of the connection of the semiconducting or metallic nature of a nanotube with the broadening of the high-energy Raman mode was given by *Krupke* et al. [248]. Their measurements of the transport properties and the Raman-scattering signal on the same tube specimen is shown
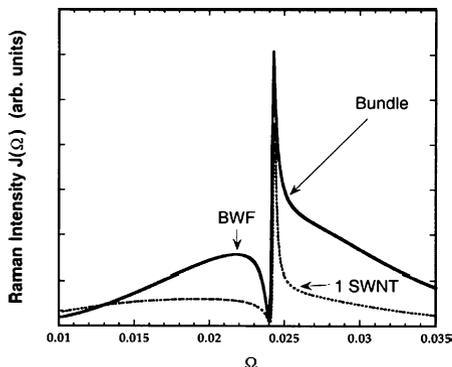
Fig. 51. Calculated lineshapes of the high-energy mode in nanotubes. An isolated nanotube, because of the small *q*-vector involved in light scattering, shows only a weak Fano resonance. Bundles of nanotubes have a much more prominent resonance. See also Fig. 52. From [132]

in Fig. 50. In the upper half of the figure a semiconducting nanotube was measured, the lower half shows the behavior of a metallic nanotube. The excitation energies, 2.41 eV and 1.96 eV corroborate the finding in Fig. 49 and the generally accepted treatment of nanotubes excited around 1.8 eV to 1.9 eV as predominantly metallic tubes.

Kempa [132] studied theoretically the origin of the broad line below the highest mode in the Raman spectrum. He worked out the proposal by *Brown* et al. [131] that the coupling of the tangential modes to the electronic continuum present in metallic nanotubes is the origin of the broad Raman line in the spectra. Semiconducting nanotubes, on the other hand, were responsible for uncoupled, Lorentzian-like peaks in the spectra. The plasmons in metallic tubes, according to Kempa, couple to the optical phonons and appear as phonon–plasmon coupled modes in the spectra. The small wavevector of the Raman excitation, however, produces only a narrow peak, see Fig. 51, for a single nanotube. Kempa invoked defects to incorporate phonon–plasmon scattering with larger *q*-vectors. Alternatively, bundles of nanotubes form a plasmon continuum, similarly as electronic bands in a solid form from the discrete states of atoms. The calculated phonon–plasmon coupled lineshape for bundles is also shown in Fig. 51 and displays a broad Fano lineshape, more similar to experiment.

An alternative explanation for the low frequency of one of the tangential modes in metallic nanotubes was put forward by *Dubay* et al. [133]. They found from first-principles calculations that in metallic tubes the Γ-point frequency of the longitudinal optical phonon is softened by what is called a Peierls-like mechanism (it is a Kohn anomaly of the axial transversal branch). In Fig. 52a their calculated optical-phonon frequencies of armchair, zig-zag, and one chiral tube are shown as a function of tube diame-
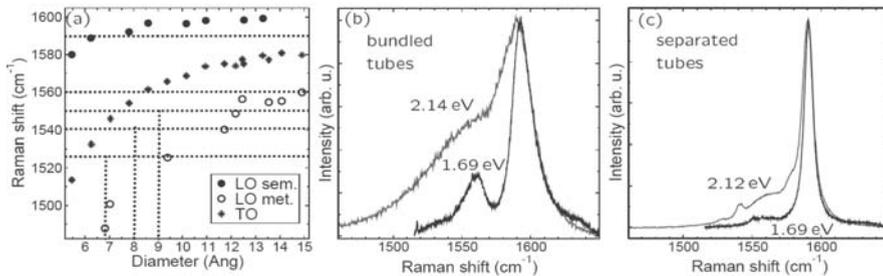
Fig. 52. (**a**) Ab-initio calculated frequencies of the high-energy optically active modes in nanotubes. Compared to semiconducting nanotubes the axial phonon in metallic tubes shows a large softening with decreasing diameter [133]. (**b**) The (softened) $1540\,\mathrm{cm}^{-1}$ mode in nanotube bundles is very broad. The origin of the larger half-width in bundled than in isolated nanotubes needs to be fully clarified [132, 250]. (**c**) In separated tubes, where the tubes are known from the experimental Kataura plot to belong to the metallic (13,1) branch, the metallic lineshape, although considerably smaller, is still visible in the spectra. From [251]

ter. With decreasing diameter, the phonon frequencies decrease, which was qualitatively found in force-constant calculations as well, although not for all optical modes [85, 103, 249]. The longitudinal and transverse modes in semiconducting nanotubes roughly follow the diameter dependence. However, the axial frequency of metallic nanotubes drops substantially below the other high-energy modes (see Fig. 52a). *Dubay* et al. [133] showed that this phonon periodically opens a gap at the Fermi level, which results in a strong electron–phonon coupling and softens the axial force constants (see Sects. 3.3 and 9.3).

We compare the high-energy mode of bundled and isolated nanotubes by *Telg* et al. [251] in Figs. 52b and c. The phonon frequencies, which are lower in the metallic nanotubes, explain the lower frequencies observed for peaks excited in resonance with transitions in metallic tubes. In semiconducting tubes, the curvature of the nanotube wall causes only a small decrease in frequency (see Fig. 52a). In Figs. 52b and c bundled tubes are compared to separated tubes at the same excitation energies. The latter were identified to belong to the (13,1) branch, i.e., to tubes with the chiralities (13,1), (12,3), (11,5), (10,7) and (9,9). The resonance of the metallic tubes is apparently much weaker in the isolated tubes compared to the bundled ones. The observations in Fig. 52 seem consistent with *Kempa*'s [132] suggestions, although the presence of a small Fano peak in separated tubes has remained controversial [252, 253]. In his model, however, the plasmon couples to the *circumferential* vibration, whereas *Dubay* and other groups predict a strong softening of the *axial* mode in metallic nanotubes [118, 140–142]. The two models are thus not compatible. This issue needs to be resolved by further experimental and theoretical work.
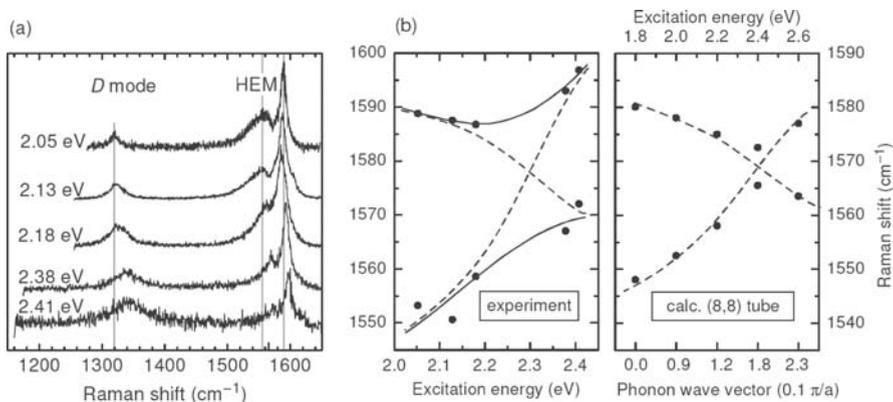
Fig. 53. (**a**) Raman spectra of an individual carbon nanotube at various excitation energies. Note the shift of both the *D* mode and the smaller of the high-energy modes. The *vertical lines* mark the peak frequencies in the uppermost trace. (**b**) Phonon frequencies from the two high-energy modes on the *left*, plotted against the energy of the exciting laser (experiment). The *right panel* shows a plot of the phonon frequencies taken from a model dispersion relation as corresponds to the excitation energies in the double-resonance model used to describe the Raman spectra in carbon nanotubes (calc. (8,8) tube). From [129]

8.2 Dispersion of Nanotube Phonons

The analysis of the high-energy phonons was pushed forward in a study of an individual metallic nanotube by *Maultzsch* et al. [129]. Take the uppermost trace in Fig. 53, where an (8,5) nanotube – as identified by its ω_{RBM} and its excitation energy in an experimental Kataura plot – is excited in optical resonance. The mode at $\approx 1560\,\text{cm}^{-1}$ is broad and softened, similarly to that of the metallic tube in Fig. 52c. Experimentally, the difference is that in Fig. 53 *an individual* tube or a very thin isolated bundle with $\approx$ 3–5 tubes deposited on a silicon substrate was studied with several different excitation energies. As the excitation energy is increased beyond the resonance energy to 2.41 eV the signal becomes weaker by over one order of magnitude, the metallic resonance disappears, and the smaller of the two high-energy peaks moves up in frequency. In fact, for higher excitation energies the spectrum begins to look like that of a semiconducting nanotube. This is a characteristic of the double-resonance process, which dominates the Raman spectra of carbon nanotubes [194].

The details of the lineshape have been calculated within the double-resonance model and agree with the results in Fig. 53a [129]. Essentially, changing the excitation energy corresponds to changing the wavevector along the nanotube axis and mapping the phonon dispersion within the Brillouin zone of the nanotube. The phonon branch derived from the measurement is compared to a calculated branch of an (8,8) nanotube in Fig. 53b. The ax-

ial and circumferential modes are seen to cross in the achiral (8,8) armchair tube, where they have different symmetries (right panel). In the experiment (left panel) the two branches anticross, as expected for the lower-symmetry (8,5) chiral nanotube. We find a good agreement of these two dispersion curves.

An interesting effect follows from the interpretation within the double-resonance model and that cannot be neglected when using the appearance of the high-energy mode for the identification of metallic nanotubes. The broad peak due to the softened phonon branch in Fig. 52a becomes narrower when moving to larger phonon wavevectors. Larger wavevectors dominate the scattering at energies above the Γ-point resonance, see Fig. 53b. Consequently, the lineshape of the same individual nanotube changes continuously from metallic-like to semiconducting-like, see Fig. 53a. An identification of a metallic tube from the shape of its high-energy mode must therefore be performed in resonance. In other words, a broadened metallic-like high-energy peak is always evidence of a metallic nanotube. A narrower semiconducting-like one may be either semiconducting or, if excited above resonance, may also be a metallic nanotube. Note that the interpretation developed in [129] relied on band-to-band transitions. For excitation above the excitonic transition an outgoing resonance can be similarly double resonant for excitonic transitions if k conservation is relaxed by defects, see [254]. Screening by the substrate and other tubes in the bundle might also reduce the importance of excitonic effects.

8.3 Electrochemical Doping of Carbon Nanotubes

The excellent chemical stability and their large surface-to-volume ratio suggest the application of single-walled carbon nanotubes as supercapacitors [255], batteries [256], actuators [19], and other electronic devices. The change in resistivity of a semiconducting nanotube by many orders of magnitude upon electrostatic gating or gas absorption has a potential for applications such as nanotube field-effect transistors [257] or electrochemical sensors [258].

As all of these applications are based on the ability to dope nanotubes, it becomes of interest to examine the effect of charge transfer or doping on the Raman spectra. The effects of intercalation of ions, say alkali metals, iodine or bromine, on the optical and Raman spectra have been discussed in [259–264]. An alternative method with different applications is electrochemical doping of carbon nanotubes, which we do not intend to review here (see, e.g., [19, 265–268]). We focus on an aspect of spectroelectrochemistry related to the high-energy Raman mode in metallic nanotubes.

The electronic structure of bundled single-walled nanotubes can be changed electrochemically by varying the potential at their interface with an electrolytic solution [19, 265]. Although the achievable doping level is lower, because the electrolyte ions form a charged double layer only with the external

surface of the ropes or bundles [269–272], it is possible to obtain quantitative information about the doping-induced strain. The strain is related to the transfered charge, which in the double-layer model can be calculated from the applied voltage. The result of such an experiment is independent of the electrolyte used and the basis for applying a linear relationship of the phonon frequency with applied voltage [269, 271]. In turn, this makes Raman spectroscopy a useful tool for analysis in spectroelectrochemical doping processes.

How much doping can be achieved by electrochemical doping? Given that one is certain to be in the double-layer charging regime, i.e., that there is no intercalation of ions from the electrolytic solution, the doping level f may be estimated from [267, 269]

$$f = \frac{M_{\mathrm{C}} C U}{F} , \tag{41}$$

where M_{C} is the atomic weight of carbon, $C \approx 35\,\mathrm{F/g}$ is the capacitance of the working electrode as determined by cyclic voltammetry, U is the applied potential, and F is the Faraday constant, the amount of charge of one mole of electrons ($F \approx 9.6 \times 10^4\,\mathrm{C/\,mol}$). In the experiment described here a mat of randomly interwoven nanotubes, so-called "buckypaper", was used as the working electrode. Intercalation effects were further reduced by using electrolytes with larger size ions, e.g., NH_4Cl, where the entire stability range of water can be explored ($\pm 1\,\mathrm{V}$). Under these conditions (41) yields a fraction not larger than $0.005 e^-(\mathrm{holes})/(\mathrm{C\text{-}atom} \cdot \mathrm{V})$. Note that this is considerably smaller than what can be achieved by intercalation. In particular, the Fermi level in nanotubes of typical diameters cannot be shifted across one or several density-of-states singularities by electrochemical doping.

In Fig. 54 we show what happens when a voltage is applied to the electrode at an excitation energy of $E_{\mathrm{exc}} = 1.95$ eV. As expected from the strong phonon–plasmon coupled modes (Sect. 8.1) there is a broad peak at $\approx 1540\,\mathrm{nm}^{-1}$ at zero applied voltage, the spectrum looks "metallic". However, with both a positive and a negative voltage applied to the nanotube electrode, there is a qualitative change in the spectra. The characteristic broadening is reduced until near 1 V the spectra resemble much more semiconducting-like spectra. In fact, phenomenologically speaking, the upper- and lower-most traces in Fig. 54 are very similar to the corresponding ones in Fig. 49a. In other words, changing the excitation energy (within a certain range) appears to have the same effect as applying an electrochemical potential.

In order to understand how this can happen, let us analyze the electrochemical Raman spectra in more detail. Figure 54b shows the frequency of the largest peak in the high-energy region as a function of applied potential. For small applied voltages it shifts linearly with a rate of $1\,\mathrm{cm}^{-1}/\mathrm{V}$ to $1.5\,\mathrm{cm}^{-1}/\mathrm{V}$ and follows the sign of the applied voltage. For larger voltages the frequency becomes $\sim V^3$. The linear shift with applied voltage, which is largely independent of excitation energy, is a well-known property of the high-energy mode [273]. The behavior of the metallic modes P3 and P4 is quite
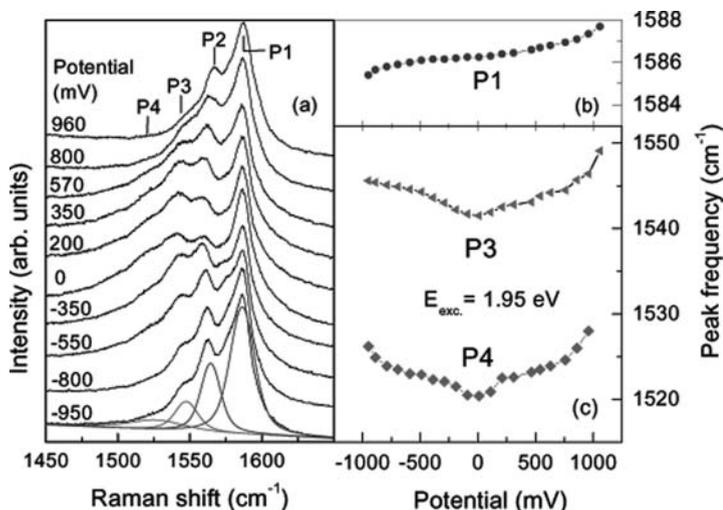
Fig. 54. (**a**) Raman spectra of a mat of single-walled nanotubes (buckypaper) at various electrochemical doping levels and an excitation energy of 1.95 eV, where metallic nanotubes are enhanced. While the 0 V potential indeed looks like the Raman spectrum of metallic tubes, see Fig. 49, the application of up to 1 V to the nanotube electrode in 1M NH_4Cl aqueous solution changes the lineshape drastically towards one that is semiconducting-like. (**b**) The frequency of the main peak, labeled P1 in (**a**), as a function of applied voltage. (**c**) Same as (**b**) but for the peaks labeled P3 (*triangles*) and P4 (*diamonds*). From [267]

different, however, see Fig. 54c. Both frequencies are $\sim V^2$, and for either sign of applied voltage they shift nonlinearly by up to $6\,\mathrm{cm}^{-1}/\mathrm{V}$ to $8\,\mathrm{cm}^{-1}/\mathrm{V}$ for the range of voltages applied (note the different frequency scales in b and c). Compared to the main peak P1 their intensity decreases drastically with applied voltage, causing the change in appearance of the high-energy mode in the Raman spectra.

An explanation offered by the authors of [274], who observed similar effects, is that the Fermi level, upon chemical doping, shifts beyond the next first valence- or conduction-band van-Hove singularity, like in intercalation experiments. As (41) shows, the electrochemically induced doping is far too small to shift the Fermi-level to the next singularity. From studies of the Fermi-level shift for various doping levels we conclude that the Fermi-level shift at $|f| = 0.005$ amounts to between 0.3 eV and 0.6 eV. However, the first metallic van-Hove singularity (≈ 0.9 eV) is not depleted below $U = 1$ V for the vast majority of metallic SWNTs in the sample of buckypaper. For applied potentials between 300 mV and 500 mV, where the metallic modes in the Raman spectra in Fig. 54a have already changed considerably, we estimate ΔE_F to be between 0.1 eV and 0.2 eV [260, 265, 269, 275]. There must be another reason for this change for small Fermi-level shifts $\Delta(E_F) < (E_{11} - E_F)$.

Let us see what follows from the interpretation within the double-resonance model [194] of Sect. 8.1 and the effect of electron–phonon coupling (Sect. 9.3). At an excitation energy of 1.95 eV in the spectra of Fig. 54a the metallic nanotubes are excited near or slightly above the first metallic resonance. Within the double-resonance model this implies a phonon wavevector near the Γ point, and the softening of the phonon branches due to the Peierls transition [133] is apparent in the low frequencies ($\approx 1540\,\mathrm{cm}^{-1}$), see also Fig. 52a. The physical reason for the softening of the phonon is a strong coupling of this mode to the electronic system, when the Fermi level lies where conduction and valence cross, i.e., at half-filling of the bands (Peierls-like softening, see Sect. 9.3). As the electrochemical doping sets in, the Fermi level moves away from the crossing point of the bands. The gap opening is reduced and disappears for large enough energies. At the same time, the phonon wavevector fulfilling the double-resonance condition increases, shifting the phonon frequency up, as in Fig. 53 for increasing excitation energies. The Peierls instability is thus switched off by applying a potential, regardless of the sign of the potential [267].

9 Electron–Phonon Interaction

Electron–phonon coupling enters critically many solid-state phenomena – the temperature dependence of the bandgap, thermalization of excited carriers, superconductivity, thermal and electrical transport among others [134, 276]. The interaction between electrons and phonons is also one step in the Raman process and thus determines the scattering cross section or Raman intensity. In turn, Raman scattering can measure the strength of the corresponding electron–phonon coupling given the optical properties of a material are known (see *Cardona* [184] and [277–279] for reviews and examples). On the other hand, electron–phonon coupling can also affect the phonon frequencies and drive structural phase transitions in solids.

In this section we first review electron–phonon coupling in carbon nanotubes and its effect on the radial-breathing mode Raman spectrum. We then discuss the Kohn anomaly (also called Peierls-like phonon softening) in metallic tubes.

9.1 Electron–Phonon Coupling of the Radial-Breathing Mode

An RBM Raman spectrum of ensembles of single-walled carbon nanotubes (bundled tubes or nanotubes in solution) typically shows several close-by peaks for a given excitation energy. We showed several examples throughout this work, in particular, in Sect. 7 (Fig. 44 on page 179). Figure 55 is another experimental spectrum (full line) obtained on nanotubes in solution [241]. The peaks within one la-ola group have different intensities. This reflects possibly a nonhomogeneous chirality distribution in the samples and the varying
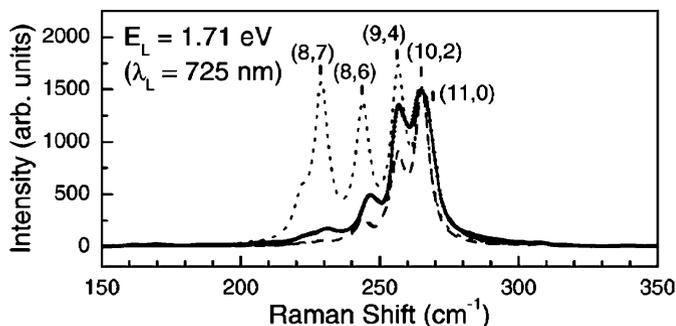
Fig. 55. Measured and calculated Raman spectra. *Full line*: Raman spectrum of isolated HiPCo tubes in solution excited with a laser energy E_L = 1.71 eV. The chiral indices of the nanotubes are indicated. *Dotted*: Calculated spectrum assuming *constant* electron–phonon coupling for tubes of different chirality. *Dashed*: Calculated spectrum including the electron–phonon matrix elements as obtained from nonorthogonal tight binding. After [170]; experimental data from [241]

resonance enhancement for an excitation energy due to the differences in the optical transition energies. It can further be due to the differences in the optical properties and in electron–phonon coupling of specific nanotube chiralities.

Popov et al. [170] calculated the Raman spectra of ensembles of tubes within a tight-binding approximation (single-electron picture) to model electron–photon and electron–phonon interaction. Using an expression similar to (25) (p. 165) with *constant* electron–photon and electron–phonon matrix elements, they obtained the theoretical spectrum shown by the dotted lines in Fig. 55. This approximation describes rather poorly the experimental spectrum, although it accounts for the chirality distribution and the varying resonance energy for different chiralities. The dashed line in Fig. 55 was calculated including the tight-binding matrix elements in the Raman cross section. As can be seen, the experimental data are very well described by this approach, thus emphasizing the importance of the matrix elements in such an evaluation [144, 170, 280].

Figure 56 summarizes the maximum resonant Raman intensities observed on single-walled nanotubes in an experimental Kataura plot. Similar to what is seen in the experimental spectrum of Fig. 55 the Raman intensity is usually highest for tubes close to the zigzag direction (first or second outermost point in the V shapes branches). There is also a family dependence. +1 semiconducting tubes such as the (11,1) branch are weaker in intensity than −1 semiconducting tubes such as the (9,1) branch. Finally, the Raman intensity within one family decreases with increasing tube diameter [63–65, 111, 241, 242].

Machón et al. [144] calculated the electron–phonon matrix element of the RBM $\mathcal{M}_{ep}$ using a frozen-phonon approximation and ab-initio techniques for
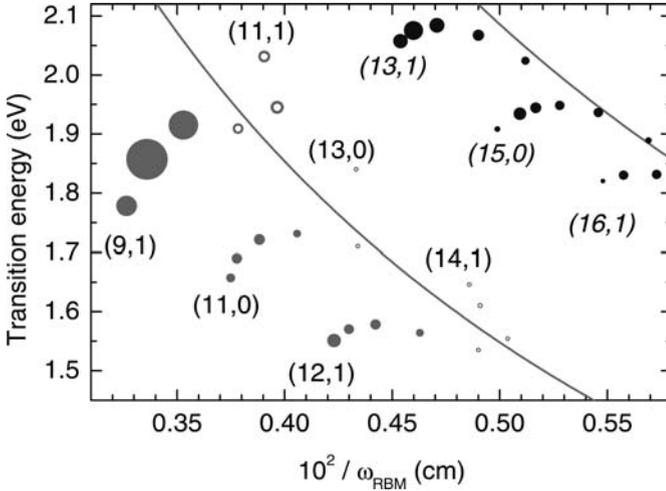
Fig. 56. Resonant Raman intensity of single-walled carbon nanotubes in a Kataura plot. The size of the symbols is proportional to the experimentally observed intensities (in arbitrary units). Intensities were obtained from the spectra normalized to the scattering intensity of BaF_2. The chiral indices indicate the branches. *Full lines* are proportional to $1/d$. The transition energies correspond to the second transition in semiconducting and the first transition in metallic tubes. The tubes were HiPCo tubes in solution (SDS coating). From [242]

the electronic structure [281]. Within this approach, the diagonal elements of the electron–phonon coupling Hamiltonian are found by imposing a deformation that mimics the phonon eigenvector and finding the shift this introduces in the electronic structure

$$\mathcal{M}_{\mathrm{ep}} = \sqrt{\frac{\hbar}{2MN\omega_{\mathrm{RBM}}}} \sum_a \boldsymbol{\epsilon}_a \frac{\partial E_{\mathrm{b}}(\boldsymbol{k})}{\partial \boldsymbol{u}_{\mathrm{a}}} , \tag{42}$$

where M is the atomic mass, N the number of unit cells, ω_{RBM} the RBM frequency, and a indexes the atoms in the unit cell of the tube. $\boldsymbol{\epsilon}_a$ is the normalized phonon eigenvector and $\partial E_{\mathrm{b}}(\boldsymbol{k})/\partial \boldsymbol{u}_{\mathrm{a}}$ describes the change in the electronic eigenenergies E_{b} due to the atomic displacement $\boldsymbol{u}_{\mathrm{a}}$. *Machón* et al. [144] showed that the electron–phonon coupling in carbon nanotubes depends on chirality through $\partial E_{\mathrm{b}}(\boldsymbol{k})/\partial \boldsymbol{u}_{\mathrm{a}}$ in four ways: 1. a diameter dependence $1/d$, 2. a dependence on chiral angle, 3. a dependence on the nanotube family, and 4. a dependence on the optical band-to-band transition E_{ii} (related to eh_{ii} for excitons).

Table 11 summarizes $\mathcal{M}_{\mathrm{ep}}$ for six zigzag nanotubes found from first principles.[8] Concentrating on the first transition, electron–phonon coupling de-

---

[8] The relative sign of the optical matrix elements will be important in the following. We therefore define $\mathcal{M}_{11}$ of the (10,0) tube as negative to facilitate the discussion.

Table 11. Electron–phonon coupling in zigzag carbon nanotubes. The table lists the matrix elements $\mathcal{M}_{ii}$ for the first three band-to-band transitions together with the transition energies E_{ii}. ν is the family index (see Table 2), d the tube diameter and ω_{RBM} the RBM frequency. Note the alternating signs between $\mathcal{M}_{11}$ and $\mathcal{M}_{22}$ as well as for one and the same transition i between $+1$ and -1 tubes. From [144]

Tube	ν	d Å	ω_{RBM} cm^{-1}	$\mathcal{M}_{11}$ meV	E_{11} eV	$\mathcal{M}_{22}$ meV	E_{22} eV	$\mathcal{M}_{33}$ meV	E_{33} eV
(10,0)	+1	7.9	287	−28	0.8	17	2.0	−30	2.4
(11,0)	−1	8.7	257	21	0.9	-28	1.3	−28	2.6
(14,0)	−1	11.0	203	16	0.7	-20	1.1	−21	2.4
(16,0)	+1	12.6	179	−17	0.6	13	1.2	−18	1.9
(17,0)	−1	13.4	170	14	0.6	-16	1.0	−17	2.1
(19,0)	+1	15.0	149	−15	0.5	12	1.0	−16	1.6

pends roughly on $1/d$ and is negative in $+1$ tubes, but positive in -1 tubes. At the same time, the absolute magnitude of $\mathcal{M}_{11}$ is larger in $+1$ tubes with $\mathcal{M}_{11}d = (220 \pm 4)$ eVÅ (root mean square deviations) than in -1 tubes (182 ± 5) eVÅ. For the second transition energy the family dependence is reversed, see Table 11; -1 tubes have a larger $\mathcal{M}_{22}$ with a negative sign, in $+1$ tubes $\mathcal{M}_{22}$ is smaller and positive. The relative magnitude of the squared matrix elements matches qualitatively the RBM intensity measurements in Fig. 56. The branches below the $1/d$ line (-1 tubes for eh_{22}) are stronger in intensity than the branches above $1/d$ ($+1$ tubes).

All four dependences can be explained on the basis of zone folding. As an example we discuss here the changes in electron–phonon coupling with nanotube family ν and transition index i in semiconducting zigzag tubes. Further details were given in [144], see also [170, 201, 280, 282].

To understand the dependence of $\mathcal{M}_{\mathrm{ep}}$ on family and transition index, we turn to Fig. 57. Here, the electron–phonon matrix elements are modeled by zone folding (see Sect. 4.1). Figure 57a shows the allowed lines of a (19,0) tube in the graphene Brillouin zone. In a zigzag tube the allowed lines run parallel to ΓM; the Γ point of the tube corresponds to the equidistant points along the ΓKM line. These are the wavevectors that contribute most to the optical spectra and hence Raman intensity in zigzag tubes; they give rise to the minima and maxima in the electronic band structure [20]. The full lines in Fig. 57b show the π band structure of graphene along ΓKM.

In the spirit of the frozen-phonon approximation to calculate $\mathcal{M}_{\mathrm{ep}}$ (42) and the zone-folding approach (Sect. 4.1) we now want to know how the π-band structure changes when imposing an RBM phonon eigenvector of a (19,0) tube [144]. For an unwrapped piece of graphene corresponding to the (19,0) tube, the RBM motion is a periodically alternating stress along $\boldsymbol{c}$, i.e., a uniaxial stress along $\boldsymbol{a}_1$ for $(n,0)$ zigzag tubes. Figure 57b shows the
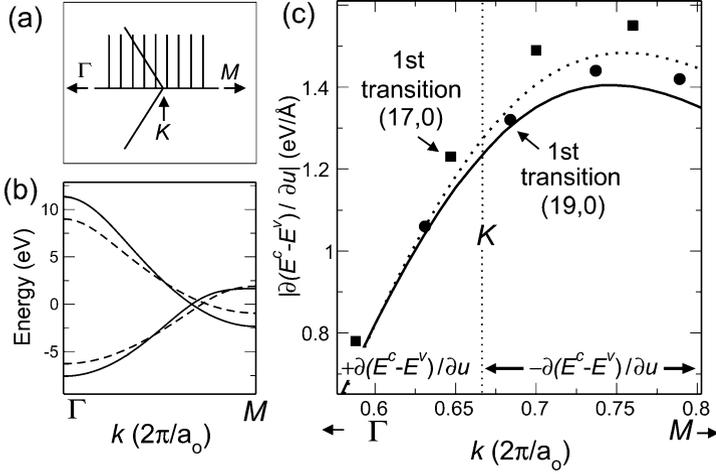
Fig. 57. Comparison between electron–phonon coupling of the RBM from ab-initio calculations and using zone folding. (**a**) Allowed k vectors of a (19,0) nanotube inside the graphene Brillouin zone. (**b**) Electronic band structure of graphene in equilibrium (*full lines*) and under the distortion that is equivalent to the RBM of a (19,0) nanotube (*dashed*). Only the π bands are shown for simplicity. (**c**) The *full line* and the *circles* give the electron–phonon coupling of the RBM in a (19,0) tube from zone folding and first principles, respectively. The *dashed line* and the *squares* are the corresponding data for a (17,0) tube. From [144]

π bands under a uniaxial stress along $\boldsymbol{a}_1$. The crossing point between the valence and conduction band (K point in unstressed graphene) moves along the $\Gamma K M$ line. Let us first concentrate on the sign of ΔE_b of the conduction bands, i.e., the band above E_F regardless of the k vector. ΔE_b is negative at Γ (the dashed line is below the full line), goes through zero at roughly $1/2\Gamma M$ and is positive between the node and the valence and conduction-band crossing in the strained structure (dashed line above the full line). Then, at the crossing between the two dashed bands, ΔE_b changes discontinuously to negative. Finally, at $M \Delta E_\mathrm{b} = 0$.

How will the change in sign of ΔE_b at $\approx K$ affect the electron–phonon matrix elements in zigzag tubes? In Sect. 4.1 we showed that the first optical transition of $+1$ tubes originates from the KM line of the graphene Brillouin zone after zone folding. From Fig. 57b we expect $\mathcal{M}_{11}$ to be negative, because $\partial E/\partial u$ is negative. For -1 tubes we expect a positive sign, since the transition comes from the part between ΓK, where $\partial E/\partial u$ is positive. This is in excellent agreement with the ab-initio matrix elements in Table 11. For the second transition energy the signs are reversed. The second transition always comes from the opposite side of K to the first transition, hence the change in sign. The $\mathcal{M}_{33}$ are all negative, because the electronic dispersion is smaller between KM than between ΓK. Enumerating the transition energies

by increasing energy (as we did in Table 11) E_{33} always originates from the KM line for the tubes given in the table.

After discussing the sign, let us turn to the magnitude of $\mathcal{M}_{\mathrm{ep}}$. The full line in Fig. 57c is the absolute value of the combined energy derivative of the valence and conduction band $|\partial(E^{\mathrm{c}} - E^{\mathrm{v}})/\partial u|$. We indicated the change in sign when crossing the K point close to the x-axis of the figure. Starting from the left the absolute energy derivative first increases (starting from zero at $1/2\Gamma M$, see Fig. 57b), reaches a maximum at $1/2KM$ and then decreases due to the vanishing coupling of the conduction band at M. Thus, the first two transitions of the (19,0) $\nu = +1$ tube are predicted as $|\mathcal{M}_{11}| > |\mathcal{M}_{22}|$ in excellent agreement with Table 11. The quantitative agreement between $\mathcal{M}_{ii}$ within zone folding (full line in Fig. 57c) and the ab-initio calculations (closed symbols) is also very good. The ab-initio results are slightly larger than those predicted from zone folding, because the RBM has a small nonradial component (Sect. 3.2), whereas the stress in the zone-folding calculation is uniaxial (purely radial RBM for the tube).

The squares in Fig. 57c show the ab-initio energy derivatives for the (17,0) -1 nanotube; the dashed line is the zone-folding result. Again, there is excellent agreement between the two calculations. Note also the change in sign and magnitude between $\mathcal{M}_{11}$ for the (19,0) and (17,0) tube (arrows) as explained before.

Within the zone-folding scheme we can also understand why $\mathcal{M}_{ii}$ depends on $1/d$. There are two reasons for this. First, for increasing diameter the same radial displacement of an atom corresponds to a smaller stress within zone folding (there are simply more bonds around the circumference). This explains why the full line in Fig. 57c is below the dashed line, $d(19,0) > d(17,0)$. Second, with increasing diameter the allowed k points for nanotubes move towards K. Considered alone, this second effect will decrease $\partial E/\partial u$ for the first transition in $+1$ zigzag tubes and increase it for the first transition in -1 tubes, see Fig. 57c. In $+1$ tubes (first transition) the two effects thus add up, whereas they have opposite signs in -1 tubes (the first effect dominates). Therefore, $\mathcal{M}_{11}d$ was larger in $+1$ tubes (220 eV · Å) than in -1 tubes (180 eV · Å).

The systematics in the electron–phonon coupling are quite interesting, because they potentially allow us to distinguish tube families based on their relative Raman intensities. Presently, we are not yet in a position to do this straightforwardly, because the optical part of the Raman process is poorly understood. A systematic confirmation of the alternating magnitude and sign of $\mathcal{M}_{ii}$ for one and the same nanotube, but different optical transitions, is still missing. *Reich* et al. [74] recently predicted other interesting differences between the Raman spectra in resonance with the first and second subband. They originate from the optical matrix elements in the expression for the Raman cross section and, in fact, enhance the expected differences between $+1$ and -1 tubes for eh_{11} resonant scattering as compared to eh_{22} (see [74] for details).
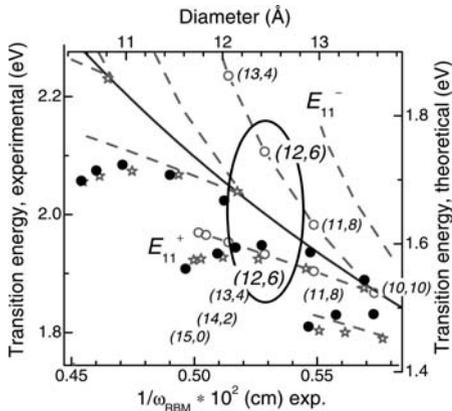
Fig. 58. Enlarged region of the experimental Kataura plot in Fig. 46. Highlighted is the (12,6) metallic nanotube, which like all metallic nanotubes, has two close-by optical transition energies. When calculating Raman matrix elements, interferences from these two transitions have to be taken into account [201]. In armchair tubes the two transitions energies are degenerate. See also [150]

9.2 Interference Effects

Turning back to Fig. 56 we note that in metallic tubes [(13,1), (15,0) and (16,1) branches] only the lower parts of the V-shaped branches have been observed experimentally [63, 64, 111, 242]. In contrast to semiconducting tubes, where the upper and lower part of a V have a different branch index β (they originate from different tubes), the two parts come from two close-by transitions in the same tubes in metallic nanotubes, i.e., the two parts of the V have the same branch index. Thus, the missing resonances cannot be due to differences in the abundance of certain chiralities in the sample.

In metallic nanotubes, trigonal warping of the graphene band structure always leads to two close-by transition energies $M-E_{ii}^{+}$ and $M-E_{ii}^{-}$. This is illustrated in the enlarged Kataura plot in Fig. 58. The (12,6), for example, has $M-E_{11}^{+} = 1.95$ and $M-E_{ii}^{-} = 2.1$ eV.[9] The first energy was measured, e.g., by *Telg* et al. [63], whereas the second one is obtained from the theoretical splitting between E_{11}^{-} and E_{11}^{+} [6], see Fig. 58 (we dropped the M in front of the energies for simplicity). *Bussi* et al. [201] showed that quantum-interference effects arise in the resonant excitation profiles of metallic nanotubes. The interferences occur between the two close-by transitions in metallic nanotubes. As we will see, this, unfortunately, does not explain the vanishing Raman intensity for the upper metallic branches in Fig. 56. Nevertheless, it is an intriguing feature and affects the transition energies extracted from a resonance profile.

---

[9] $+/-$ is chosen in analogy to the $+/-1$ semiconducting families; therefore the $+$ branch has the lower transition energy for E_{11}.
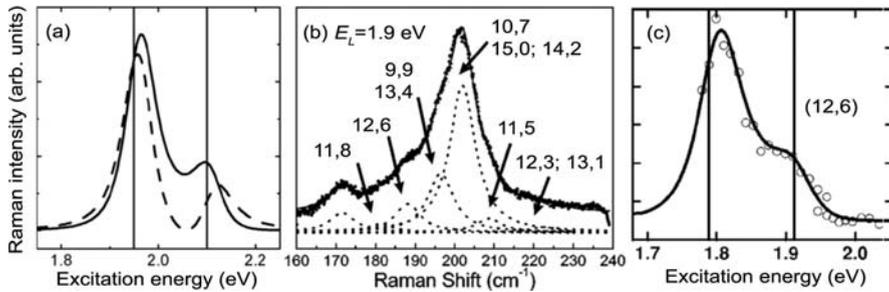
Fig. 59. Raman intereferences in metallic nanotubes. (**a**) Calculated resonance profile for two close-by transition energies $E_{11}^+ = 1.94$ eV and $E_{11}^- = 2.1$ eV. *Full line*: negative ratio between the electron–phonon matrix elements for the two transitions, $\mathcal{M}_{11}^+/\mathcal{M}_{11}^- < 0$, as found from ab-initio calculations. *Dashed line*: $\mathcal{M}_{11}^+/\mathcal{M}_{11}^- > 0$. This plot proves that Raman-interference effects are present in the Raman resonances of metallic tubes, because the calculated profiles differ (*full* and *dashed lines*). (**b**) Raman spectrum of bundled carbon nanotubes produced by pulsed-laser vaporization; the laser energy was $E_L = 1.9$ eV. (**c**) Raman resonance profile for the mode at $188 \, \mathrm{cm}^{-1}$ corresponding to the (12,6) nanotube. After [200] and [201]

Bussi et al. [201] modeled the Raman profiles using the single-resonance expression for band-to-band transitions (29) (p. 167). The sum in the Raman matrix element $K_{2f,10}$ runs over *all* intermediate electronic states including contributions from different excited states, i.e., different optical transitions. We obtain for two transitions E_{11}^+ and E_{11}^-

$$K_{2f,10} = \frac{L}{i\sqrt{2}\hbar^2\omega} \left[\frac{\mathcal{M}_{11}^+ \mu_{11}^{+\,1/2}}{(E_1 - E_{11}^+ - i\gamma)^{1/2}} - \frac{\mathcal{M}_{11}^+ \mu_{11}^{+\,1/2}}{(E_1 - \hbar\omega - E_{11}^+ - i\gamma)^{1/2}} \right.$$
$$\left. + \frac{\mathcal{M}_{11}^- \mu_{11}^{-\,1/2}}{(E_1 - E_{11}^- - i\gamma)^{1/2}} - \frac{\mathcal{M}_{11}^- \mu_{11}^{-\,1/2}}{(E_1 - \hbar\omega - E_{11}^- - i\gamma)^{1/2}} \right], \quad (43)$$

where $\mathcal{M}_{11}^+$ are the combined electron–photon and electron–phonon matrix elements for E_{11}^+; correspondingly for $\mathcal{M}_{11}^-$. $\mu_{11}^{+/-}$ are the reduced effective masses for the $v_1^{+/-}$ valence and the $c_1^{+/-}$ conduction band. Depending on the relative sign of $\mathcal{M}_{11}^+$ and $\mathcal{M}_{11}^-$ the two resonances in (43) will add up constructively or destructively, i.e., we obtain an interference in the Raman cross section as a function of E_1.

Figure 59a shows the Raman profile obtained from (43) for $\mathcal{M}_{11}^+/\mathcal{M}_{11}^- = -2$ by the full line and for $+2$ by the dashed line. The two profiles differ, which is the manifestation of quantum interference [201]. Let us now use (43) for fitting the resonance profile of a metallic nanotube. The matrix elements were obtained from first principles in [201]. They showed similar systematics as in semiconducting tubes. In particular, $\mathcal{M}_{11}/\mathcal{M}_{22}$ is always negative (see also [144]). Figure 59b shows the Raman spectrum of bundled tubes excited

at $E_L = 1.9$ eV [200]. We assigned the peaks based on the experimental Kataura plot as explained in Sect. 7 taking into account the redshift of $\approx$ 0.1 eV induced by the bundling [9, 245]. The experimental resonance profile of the (12,6) tube with $\omega_{RBM} = 188\,cm^{-1}$ (symbols in Fig. 59c) was fitted by two resonances at 1.79 eV and 1.91 eV (full line for the fit, vertical lines for the energies) [201]. As pointed out by *Bussi* et al. a Raman assignment based on the splitting between the two metallic resonances can be affected quite severely by Raman interferences (see [201] for further details; similar results were obtained also in [282]).

A remark about the experimental data in Fig. 59c as well as other resonance Raman profiles in the literature are necessary. First, there are a number of papers using joint density of electronic states to model the Raman intensity of carbon nanotubes, which is incorrect. Regardless of the model (band-to-band transitions, excitons) the incoming and outgoing resonant Raman profiles are always symmetric peaks (as a function of excitation energy) and never expected to follow a $1/\sqrt{E}$ dependence [201]. We have already discussed this in Sect. 6.2. The assignment based on $1/\sqrt{E}$ Raman profiles and the experimental values, e.g., for the broadening parameter γ need to be re-evaluated. The experimental data in Fig. 59c show a strong high-energy shoulder assigned to the second transition E_{11}^-, which was not observed in isolated nanotubes in solution. On the other hand, the Raman data on semiconducting bundled tubes have a similar asymmetric profile as observed for the (12,6) in [200], although interferences are not expected in semiconducting tubes where $E_{22} \gg E_{11}$. Comparing experimental data on nanotube bundles with a theory for isolated tubes is always a little delicate. The shift in the resonance energy for E_{11}^+ between (12,6) tubes in bundles and isolated (12,6) tubes in solution (0.1 eV), compare Fig. 59c and Table 10, is in rather nice agreement with ab-initio calculations and experiment [9, 245]. It needs to be clarified whether asymmetric profiles are really intrinsic to metallic tubes and why the surfactant-coated tubes do not show a second resonance.

In Fig. 59a the resonance due to E_{11}^+ is stronger than the E_{11}^- resonance. The ratio between the two intensities is on the same order as the squared ratio between the combined matrix elements for electron–photon and electron–phonon interaction (four). The absence of the upper resonance in metallic tubes in solution might be caused by larger differences between the $\mathcal{M}_{11}^+$ and $\mathcal{M}_{11}^-$ or by an additional mechanism not considered so far.

9.3 Kohn Anomaly and Peierls Distortion

Kohn showed in a seminal paper that metals have anomalies in their phonon dispersion with $|\nabla_q \omega(q)| = \infty$ [138]. For a simply connected Fermi surface, e.g., a circle, these anomalies occur at $q = 2k_F$, where $+k_F$ is the Fermi wavevector. For these qs and phonon symmetries that couple electrons at E_F the electron–phonon coupling is particularly large. This can even drive a static distortion of the entire lattice, which is known as a Peierls distortion for
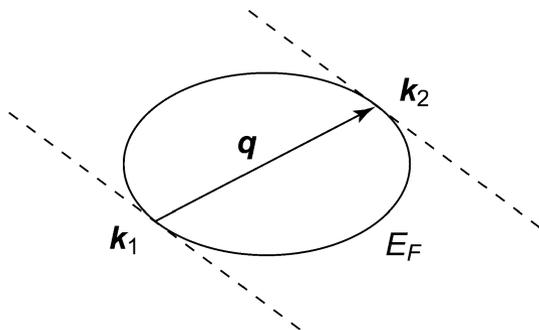
Fig. 60. Two parallel lines (*dashed lines*) touch the Fermi surface E_F in the points k_1 and k_2. At the wavevector $q = k_2 - k_1$ the phonon dispersion becomes singular. Behind this Kohn anomaly is an abrupt change in the ability of the electrons to screen the lattice vibrations. After [138]

a one-dimensional system [283]. An atomic chain will dimerize and double its periodicity. The distortion opens up a gap at the Fermi energy and thus lowers the total energy of the system. Kohn anomalies and Peierls transitions are currently widely discussed for carbon nanotubes [127, 140–142].

Figure 60 shows the condition for the phonon wavevectors q at which $\omega(q)$ becomes singular [138]. Two parallel lines (dashed lines) touch the Fermi surface (full line) in k_1 and k_2. Then a Kohn anomaly occurs at $q = k_2 - k_1$ given the phonon has the right symmetry to couple electrons at E_F. The Fermi surface is a single point in graphene; hence, in the limit $k_2 \to k_1$ we expect a Kohn anomaly at $q = 0$. A second anomaly occurs for the wavevector connecting the K and K' point, i.e., $q = K$. Only the E_{2g} optical branch at Γ and the TO (A') branch at K become singular in graphene for symmetry reasons [127].

Metallic nanotubes with $d \approx 1\,\mathrm{nm}$ and above show two Kohn anomalies. One for the axial modes at Γ originating from the E_{2g} phonon of graphene and one for the backfolded branch at $2\pi/3a$ originating from the TO branch at K [3, 127]. These phonons are anomalous also in graphite, the $d \to \infty$ limit of carbon nanotubes. When the diameter of the tubes decreases the number of anomalous branches increases to five, see Fig. 61a [140, 142]. This is an interesting example of symmetry lowering and structural distortions in low-dimensional structures. In graphite, only the E_{2g} phonon at Γ and the TO branch at K can couple the π and π^* bands close to E_F [125, 207]. In carbon nanotubes we find, e.g., for armchair tubes that the coupling is allowed by symmetry for phonon branches correlated with the A_{1u}, A_{2g}, B_{1u} and B_{2g} representations at Γ; these modes are shown in Fig. 61b. Five optical modes and the rotation around z belong to these representations, see Table 5. A_{1u} and B_{2g} correspond to the anomalous graphite branches at Γ and K, respectively. Although four other modes are allowed to couple electrons at E_F as well, this will not have a strong effect until the atomic
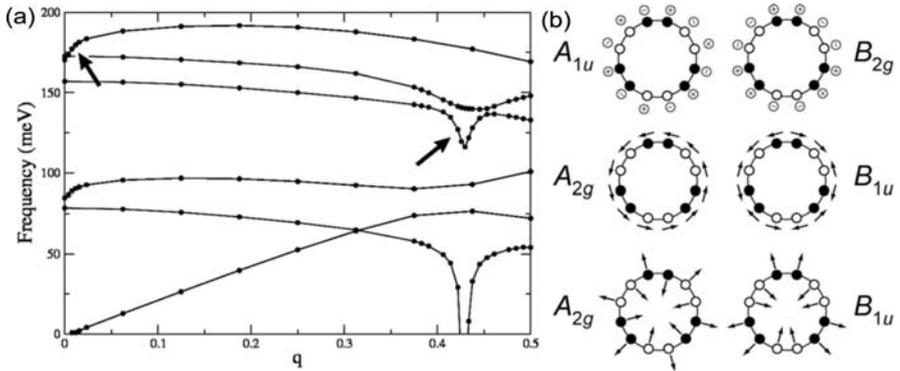
Fig. 61. Kohn anomaly and Peierls distortion in a (3,3) armchair nanotube. (**a**) Anomalous phonon branches calculated from first principles showing giant Kohn anomalies. The two modes indicated by *arrows* behave singular for larger-diameter tubes and graphene as well, see [127] and [141]. (**b**) Γ-point eigenvectors of the anomalous branches. The two axial modes belong to the arrowed branches in (**a**). The A_{2g} mode with the displacement along the circumference is the rotation around z (forth acoustic branch); the radial A_{2g} mode corresponds to the out-of-plane optical phonon of graphite (ZO mode). The radial B_{1u} mode drops to zero in (**a**); it induces the Peierls transition in the (3,3) tubes

structure becomes significantly different from the graphene cylinder limit. This only happens for tubes with $d \ll 1\,\mathrm{nm}$ as for the (3,3) tube in Fig. 61a with $d = 4\,\text{Å}$ [154].

The Kohn anomaly for the radial branch with B_{1u} symmetry in a (3,3) nanotube is so strong that the phonon frequency was found to be imaginary in ab-initio calculations [140, 142]. This means the tube will undergo a Peierls transition; the transition energy was predicted between $240\,\mathrm{K}$ and $400\,\mathrm{K}$ (see [140] and [142] for details). Note that the phonon q vector inducing the Peierls transition is incommensurable with the unit cell. Thus, straightforward total-energy calculations of a (3,3) nanotube will not predict this transition.

A Kohn anomaly always implies a particularly strong electron–phonon coupling for the qs where $\omega(q)$ turns singular. In metals, the Raman spectrum, therefore, often reflects the strength of the electron–phonon coupling as a function of ω (note that in metals wavevector conservation is relaxed due to the small penetration length of the light) [139]. A strong experimental indication for the presence of the Kohn anomaly in graphite and carbon nanotubes is thus the high-energy range of the Raman spectrum. The spectra are dominated by scattering from the tangential A_1 high-energy vibrations (the axial mode of metallic tubes is singular at Γ) and the D mode (singular at $2\pi/3a$). Metallic isolated nanotubes often show a strong and sharp D line (see [99]).

According to [133] and [141] phonon softening due to Kohn anomalies is stronger in metallic tubes than in graphite. This results from the one-dimensional character of single-walled carbon nanotubes. The axial tangential mode periodically opens and closes a gap in metallic tubes, whereas it only shifts the Fermi point in graphene. Because of this oscillation of the bandgap *Dubay* et al. [133] used the term Peierls-like distortion when discussing lattice dynamics of metallic tubes. Experimentally, the D mode is indeed at lower frequencies in carbon nanotubes than in graphite, although a detailed study of this phenomenon is missing. Also, the excitation-energy dependence of the high-energy phonons in carbon nanotubes confirmed the extremely strong overbending for the softened axial phonon at Γ (see Sect. 8).

The calculated electron–phonon matrix element for the graphite optical modes is $200\,\mathrm{meV}$ at Γ ($\omega = 1540\,\mathrm{cm}^{-1}$) and $300\,\mathrm{meV}$ ($1250\,\mathrm{cm}^{-1}$) for the transverse branch at K [127]. In carbon nanotubes the coupling of these modes to the electronic system is thus at least an order of magnitude larger than for the RBM (see Table 11), in contrast to the predictions of [75]. Since electron–phonon interaction is also crucial for the relaxation of photoexcited carriers and in connection with the breakdown of ballistic transport in carbon nanotubes, we expect more studies of electron–phonon coupling to appear in the near future.

10 D Mode, High-Energy Modes, and Overtones

The D mode in graphite and carbon nanotubes is characterized by the dominance of the Raman double resonance in the spectra. The double resonance for the high-energy mode in nanotubes has similar experimental characteristics, but they are not as prominent. A similar statement holds for the overtones of the D and G modes. The detailed mechanism of this process was explained in Sect. 6.3. We summarize here the experimental evidence most frequently found for a double resonance [20, 125, 207, 230].

1. In the first-order spectrum the strength of the Raman signal is related to the number of defects or other symmetry-breaking elements, like the surface in Ge where visible light is strongly absorbed [213, 214] or the end of a nanotube [4, 218].
2. Excitation-energy dependence of the corresponding Raman peak, as best seen for the D band in graphite or in carbon nanotubes, see Fig. 38. The excitation-energy dependence is particularly large for the D band because the electronic and phononic bands are strongly dispersive for the double-resonant k and q vectors. In Ge, the excitation-energy dependence is less pronounced due to the flat optical-phonon bands [4, 210].
3. A large Raman intensity as seen, e.g., for individual carbon nanotubes, see Fig. 53 [4, 99, 284].
4. Frequency and lineshape differences in Stokes and anti-Stokes spectra, see [20, 125, 205, 211, 219, 230], or Fig. 37c.
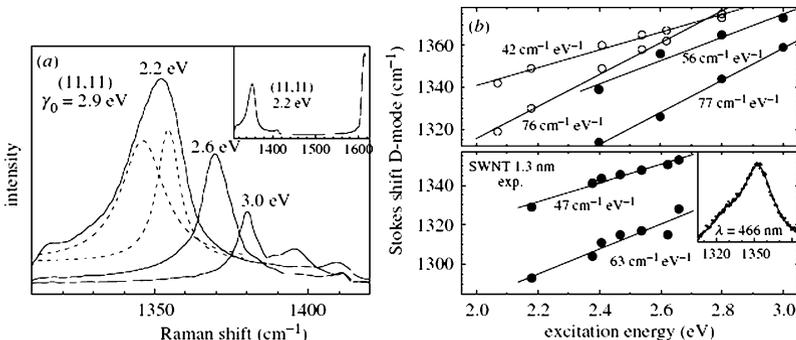
Fig. 62. (**a**) Calculated D-mode Raman spectrum of an (11,11) nanotube for different excitation energies (*inset*) extended scale. (**b**) Frequencies of the two D-mode components as a function of excitation energy. *Open symbols* refer to a (10,10) nanotube, *closed* ones to an (8,8). Experimental values are shown for comparison in the *lower part* of the figure. From [230]

5. Deviations from Lorentzian lineshapes, as observed for the high-energy mode in carbon nanotubes [194].

Not all of these observations are sufficient to identify double resonance; two-phonon scattering, e.g., also leads to deviations from a Lorentzian lineshape in the spectra. In the following sections we discuss several aspects of double resonance in the high-energy region ($> 1000\,\mathrm{cm}^{-1}$).

10.1 D Mode and Defects

The D mode in the Raman spectrum of graphite was discussed extensively in connection with the double-resonance process in Sect. 6.3, and we focus here on some special aspects in nanotubes. The similarity of the excitation-energy-dependent shift found in the nanotubes suggested a physical process similar to that found in graphite. *Maultzsch* et al. [206] showed that there is a selection rule for the D mode related to the chirality of the nanotube. Namely, only when $(n_1 - n_2)/3n =$ integer (the so-called $\mathcal{R} = 3$ tubes) is D-mode scattering allowed. All other tubes ($\mathcal{R} = 1$) can also have double resonances, but the phonons involved are near-Γ-point phonons and hence not in the energy region of the typical D mode (see also Table 1).

In Fig. 62 we show the calculated D mode of an (11,11), a (10,10), and an (8,8) nanotube based on the double-resonance model in comparison to an experiment on nanotube bundles. The observed shift of the Raman frequency with excitation energy is well reproduced, which is the most prominent criterion for the observation of double resonance. The D mode is also observed in individual nanotubes, see Fig. 53, which implies that its Raman cross section is unusually large; the lineshape is non-Lorentzian. Differences in the Stokes
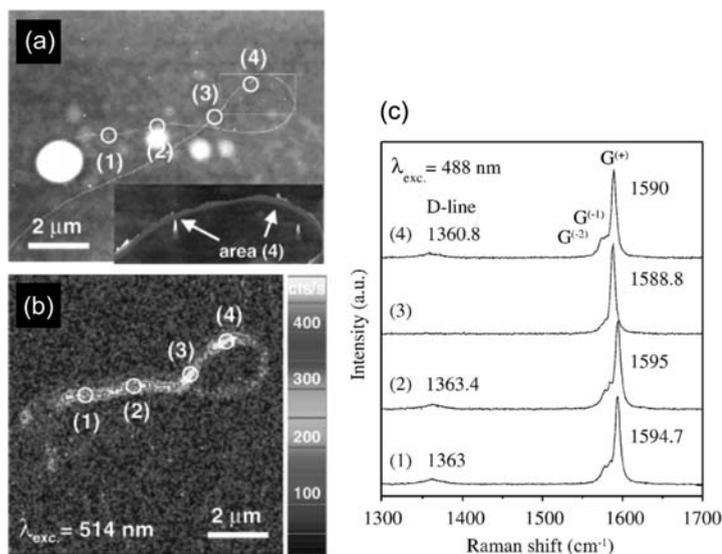
Fig. 63. (**a**) Atomic-microscope image of a carbon nanotube grown by a CVD method. The numbers mark four spots along the nanotube, for which the Raman spectra are shown in (**c**). (**b**) Raman image obtained by imaging the energy region of the G mode. (**c**) Raman spectra recorded at the specified points of the image in (**a**). Note the difference in D-mode intensity for the different spots, which reflects structural inhomogeneities along the nanotube. After [286]

and anti-Stokes spectra of the D mode have been reported also. They support the origin of the D mode in nanotubes as a double resonance [230].

The signal in Raman double resonance depends on a convolution of the two resonances. In carbon nanotubes the intensity therefore increases when the laser energy matches the separation in energy between a maximum in a valence band and a minimum in a conduction band in the band-to-band transition picture (only this model has been used, so far, for a calculation of the D-mode spectra). This can be seen in the variation of the Raman signal with excitation energy in Fig. 62a. The signal increases when the laser energy approaches the energies of the critical points in the electronic band structure, which was further discussed by *Kürti* et al. [285]. Note, however, that *Kürti* et al. disarded the selection rules for elastic scattering developed by *Maultzsch* et al. [206]. Conclusions about D-mode intensities for varying chirality, therefore, differ in [285] and [206].

Confocal Raman spectroscopy combined with atomic-force microscopy allows a space-resolved imaging of individual carbon nanotubes. We show in Fig. 63a combined measurement by *Jiang* et al. [286]. In Fig. 63a the atomic-force microcope picture of a curved nanotube is shown. Figure 63b shows the Raman image of the same tube taken by recording the spatially resolved G-
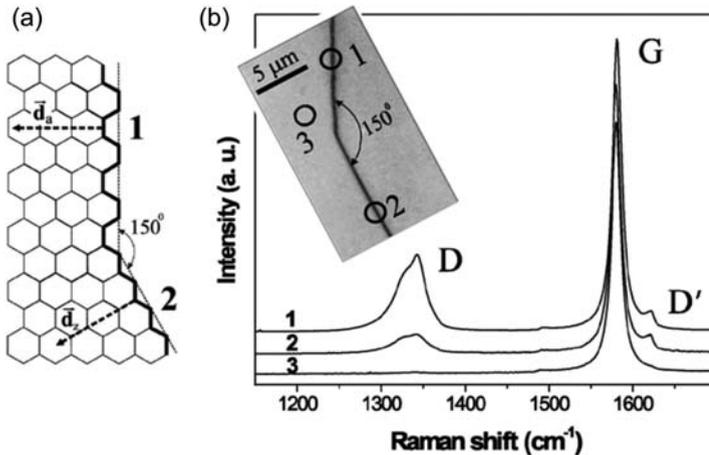
Fig. 64. (**a**) Orientation of a small HOPG crystallite as determined by atomic-force microscopy. Armchair and zigzag directions are indicated. (**b**) Raman spectra taken off the edge of a small HOPG crystallite at the numbered points 1,2 and 3. The D mode is largest at point 1, which corresponds to the "armchair" edge of the crystallite. At point 2, the "zigzag" edge, the D mode is nearly absent. These spectra verify the selection rules predicted in [206] for D-mode scattering. After [287]

mode intensity. A bright spot corresponds to a high G-mode intensity; it is by no means as homogeneous as one might expect for a first-order Raman process. Instead, the Raman intensity varies considerably along the tube, which is reminiscent of double-resonance scattering. Unfortunately, the authors of [286] did not show the intensity of the overtone spectra, which should be independent of defect density and would clarify the type of Raman process (see Sect. 10.3). As it stands, the variations in intensity of the D mode could be due to different defect concentrations or selection rules ($\mathcal{R} = 3$ vs. $\mathcal{R} = 1$) in the different tube sections or to a variation of the defect type and density.

A confirmation of the $\mathcal{R} = 3$ selection rule was given by *Cançado* et al. [287]. These authors recorded Raman spectra of different types of edges of HOPG graphite crystallites that they also investigated with an atomic-force microscope (AFM). While there was no D mode far from a crystallite edge (position 3 in Fig. 64), they found a large D mode on one type of edge (position 1) and an ≈ 4 times smaller one on another type of edge (position 2), see Fig. 64b. Here the edge of the crystallite serves to break the translational symmetry, as is the case of the surface of the Ge crystal [213, 214]. From the AFM analysis the authors identified the graphite edge with a large D mode with an armchair-type edge, while the smaller D mode originated from a zigzag-type edge, see inset of Fig. 64b and a. Since all zigzag tubes are $\mathcal{R} = 1$ tubes, the D-mode scattering from the zigzag edge is forbidden by the selection rule derived in [206]. The small residual peak observed in the spectra is probably due to imperfections. Note also that the intensity of the
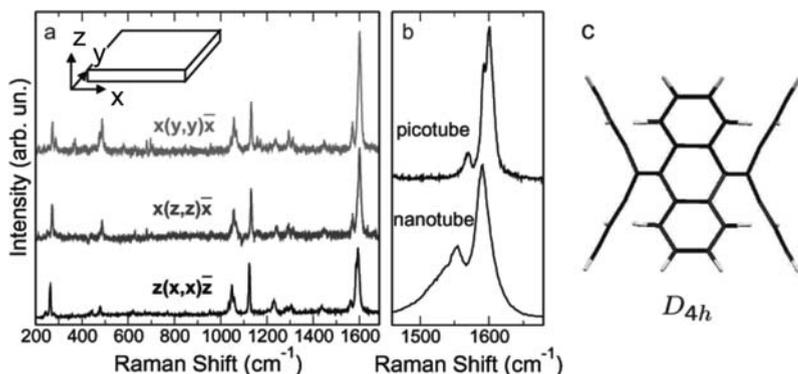
Fig. 65. (**a**) Raman spectra of a macroscopic picotube crystal for three different orientations along the crystal edges as shown in the *inset*. (**b**) a blowup of the high-energy Raman spectrum of the picotube crystal compared to that of a bundle of nanotubes at the same excitation energy (1.96 eV). The picotube spectra resemble those of nanotubes only for the HEM region. (**c**) Side view of the (4,4) picotube molecule. Shown is the idealized D_{4h} structure with inversion symmetry. The center ring of hexagons is the same as that of a (4,4) armchair nanotube. In the real molecule upper and lower wings bend away by different amounts from the z-axis of the tube. Going around the tube, larger and smaller bending angles alternate, resulting in a D_{2d} symmetry of the real molecule. After [288]

D' mode is constant in position 1 and 2. The double-resonant process giving rise to D' in graphite is the one responsible for the high-energy Raman spectra (G mode) in single-walled carbon nanotubes. This mode was predicted to be double resonant for $\mathcal{R} = 1$ and 3 tubes alike [206], in agreement with the edge Raman spectra in Fig. 64b [287].

10.2 Picotubes

A nice example of a material where a Raman double resonance does *not* occur, although the atomic structure is quite similar to those of nanotubes, are the recently investigated carbon picotubes [288]. They are molecules with the chemical formula $C_{56}H_{32}$ and D_{2d} symmetry and resemble short sections of (4,4) carbon nanotubes. They crystallize in macroscopic molecular crystals. See Fig. 65c for the structure of a single molecule; the crystal structure as deduced from X-ray diffraction can be found in [288]. These molecules have carbon-bond-related vibrational frequencies and Raman spectra quite similar to that of the corresponding nanotube. The interactions between the molecules are so weak and the picotubes so short that there is no dispersion in the vibrations. Consequently, the vibrational modes in picotube crystals do not show an excitation-energy dependence (also, the bandgap of picotubes is in the UV [289, 290]).

In Fig. 65a we show the Raman spectrum of a tiny picotube crystal for three different crystal orientations; the corresponding Raman tensors and mode symmetries were analyzed in [288]. Note the similarity of the high-energy mode in picotube crystals (upper trace) and in bundles of nanotubes (lower) in the enlarged spectrum in Fig. 65b. The trace of the picotube crystal is a simple superposition of three or more peaks with Lorentzian lineshape. In the metallic nanotubes, however, at $E_{exc} = 1.96$ eV the spectrum at $\approx 1540\,cm^{-1}$ in bundled nanotubes is asymmetric, as is typical for metallic nanotubes (see Sect. 8.1). At the same time, the high-energy shoulder of the largest peak in the nanotube bundle has broadened into a non-Lorentzian lineshape, which is characteristic of the double-resonance process. The lineshape of the high-energy mode in double resonance was calculated by *Maultzsch* et al. [194, 207]. In isolated nanotubes (i.e., unbundled ones) the high-energy mode becomes more symmetric and hence more like the spectrum in picotubes, but the asymmetry characteristic for double resonance remains [129]. The details of the asymmetry of this peak in metallic tubes are subject to ongoing discussion [252, 253]. Nevertheless, it is clear that in picotubes, for lack of appropriate transitions and the necessary phonon dispersion, the high-energy mode cannot be attributed to a double-resonance process.

Another important difference between picotubes and nanotubes is the absence of the shape-depolarization effect. As explained in Sect. 6.4 this effect in nanotubes is related to their large aspect ratio $\approx 10^2$ to 10^7. They exhibit a nonzero Raman intensity only if both the incoming and outgoing light are polarized along the nanotubes axis (zz configuration). Picotubes do not have a depolarization due to their shape, because they are very short (aspect ratio ≈ 1). Therefore, a Raman signal is observed in all three scattering configurations in Fig. 65a.

10.3 Two-Phonon Modes

The two-phonon Raman spectrum of graphite and carbon nanotubes extends from just above the high-energy mode to twice that frequency, say $1600\,cm^{-1}$ to about $3200\,cm^{-1}$ [145, 210]. This region is interesting not simply because overtones and combinations of the first-order modes can be found. Wavevector conservation plays an important role in two-phonon scattering, which we shall discuss in this section.

For the Raman double-resonance process we showed that for reasons of wavevector conservation a defect or a surface has to be involved (Sect. 6.3). This is best seen Fig. 36b, where the incident photon with ≈ 0 momentum (compared to the quasimomentum of the Brillouin zone) resonantly excites an electron–hole pair. The second resonant transition is scattering of the electron (or hole) by emission (or absorption) of a phonon (transition $a \rightarrow b$). In order to conserve quasimomentum the electron has to be scattered back to a point where its momentum is near that of the initial hole (or the hole has to be
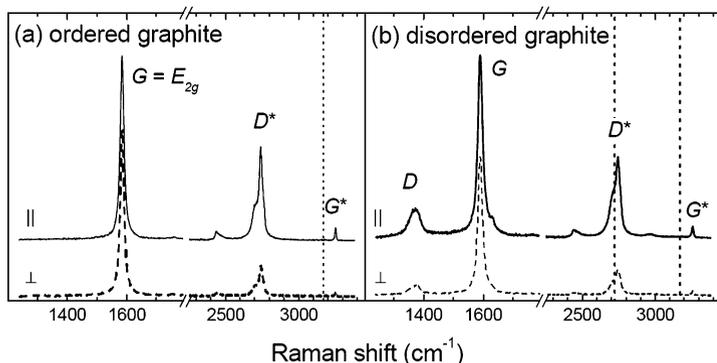
Fig. 66. The Raman spectrum of different spots of natural single-crystalline graphite (samples are $\sim 100\,\mu$m in each dimension). (**a**) Ordered graphite shows the allowed first-order mode at $1582\,\mathrm{cm}^{-1}$ and a second-order D^* mode at $2750\,\mathrm{cm}^{-1}$. Note the absence of the D mode in the spectra. (**b**) Disordered graphite also shows the well-known D mode, here at $1370\,\mathrm{cm}^{-1}$. It is apparently induced by defects in the lattice structure. Note also the overtone of the G mode at $3250\,\mathrm{cm}^{-1}$ in both ordered and disordered graphite. Its frequency is more than twice the first-order frequency because of the overbending of the corresponding phonon branch, see text. $\parallel$ and $\perp$ refer to parallel and perpendicular relative polarizations of the incident and scattered beams. From [125]

scattered to near the electron). The simplest form of scattering the electron back is inelastic scattering by a generic defect, which is shown as a horizontal dashed line in the figure. This is the double-resonance process that appears in the first-order Raman spectra [4, 125, 207].

It is also possible to conserve momentum by emitting (or absorbing) a second phonon. The essential difference as far as the Raman double resonance is concerned is that a defect is no longer necessary for quasimomentum conservation. Instead, the second phonon is emitted with equal and opposite momentum thus conserving momentum in the overall Raman process. It follows that an overtone in double resonance should shift with twice the rate as compared to the corresponding first-order mode. It should also have the additional characteristics of a double resonance, which are a large (relative) intensity, differences in Stokes and anti-Stokes frequencies, and non-Lorentzian lineshapes. All of these properties are indeed fulfilled for the overtone of the D mode in graphite, single and multiwalled nanotubes.

We show in Fig. 66 the role of defects in first-order and two-phonon scattering [125]. In ordered graphite (a) we see for both polarizations the strong G mode, which is the allowed mode (E_{2g} symmetry in graphite) [218]. At a frequency of $2750\,\mathrm{cm}^{-1}$ we see the D^* mode, and at even higher frequencies the second-order peak of the G mode, commonly referred to as the G^* mode, at $3250\,\mathrm{cm}^{-1}$. In disordered graphite, Fig. 66b, we see, in addition, the defect-induced D-mode at $1350\,\mathrm{cm}^{-1}$ [218]. D^* can be regarded as the overtone of

the D mode, which is only seen in the Raman spectra when induced by defects or when quasimomentum is conserved by a second emitted phonon. The D^* peak has approximately the same intensity in the two Raman spectra of Figs. 66a and b, whereas the first-order mode is completely absent in Fig. 66a. Hence the D^* mode is *not* induced by defects.

Owing to the lack of correlation of many of the defects the overtone D^* mode is ideally suited for a quantitative assessment of the defect density in graphite and graphite-based materials. Traditionally, this is done from Raman spectra by comparing the amplitude of the D mode to that of the G mode, which – as a first-order allowed mode – is supposed to be independent of defect density. In carbon nanotubes, however, there is still a large controversy as to whether the high-energy mode (the equivalence of the G mode in graphite) is truly a first-order mode [194, 291]; in fact, there is ample evidence that it is not. Even if it is only partially double resonant, it is not suited as normalization of the defect density, as its intensity is then partially dependent on defect density as well, which would result in a reduced defect-density dependence of the intensity ratio of the two peaks. Measurements on multiwalled carbon nanotubes with different concentrations of boron doping clearly show this effect [292]; see also Fig. 63, where the D and G-mode intensities vary along a curved nanotube.

The overtone spectra give us information about the phonon dispersion in a crystal. Because the quasimomentum conservation is fulfilled by the emission of the second phonon, the overtone spectra in a crystal reflect the density of phonon states. This effect is well known and, e.g., has led to an important conclusion as regards the phonon dispersion of graphite. In 1979 *Nemanich* and *Solin* [293] were the first to realize that the sharp peak at $3247 \, \text{cm}^{-1}$ in the second-order spectra of graphite was due to the overbending of the graphite phonon dispersion (see Sect. 3.3). The overbending leads to a peak in the overtone spectra at the highest phonon energies in the branch and can be estimated by $\omega_{2\text{ph}} - 2\omega_{\text{ph}} \approx 40 \, \text{cm}^{-1}$, see [125, 145, 293]. In Fig. 66 the positions of $2\omega_{\text{ph}}$ are indicated by vertical dashed lines. Raman spectra of single-walled carbon nanotubes showed that the highest overtone phonon frequencies is not more than twice the frequency at the corresponding Γ point [145]. This observation is in accordance with the softening calculated from ab-initio work as compared to the zone-folding methods, see also Sect. 3.3.

In Fig. 67a we show the excitation-energy dependence of the second-order D^*-mode of single-walled nanotubes [145]. It shows a roughly twice as large shift when compared to the first-order mode, as expected from double-resonance theory [4, 219]. Again, the phenomenon is not unique to carbon nanotubes, but was shown, e.g., by *Reedyk* et al. in $Pb_2Sr_2PrCu_3O_8$, a semiconducting compound structurally related to a high-T_c superconductor. For a detailed discussion of the Raman features of this compound, see [294].
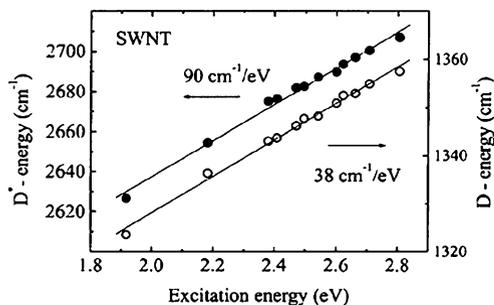
Fig. 67. The excitation-energy dependence of the overtone D^* in single-walled carbon nanotubes (*closed symbols*) as compared to that of the first-order mode (*open*). The overtone shifts with excitation energy roughly twice as fast as the first-order mode. From [145]

10.4 Phonon Dispersion

Double-resonant scattering involving large phonon q vectors may be utilized to map the phonon-dispersion relation as pointed out by *Thomsen* and *Reich* in [4]. This concept was first applied to graphite by *Saito* et al. [295], and later more completely by *Reich* and *Thomsen* [125]. The idea is based on the linear relation of the phonon wavevector q and the excitation energy in the double-resonance process (33). The (linearized) electronic dispersion is given by the Fermi velocities v_1 and v_2 and the phonon frequency $\hbar\omega_{\mathrm{ph}}(q)$. To a simplest approximation the phonon energy may be neglected compared to excitation energy and q evaluated straightforwardly. If $\hbar\omega_{\mathrm{ph}}(q)$ is to be taken into account, q involved in the double-resonance process may be obtained iteratively [4, 207].

Mapping the phonon dispersion in the simplest approximation corresponds to taking peaks identified as doubly resonant from Raman spectra (from their excitation-energy dependence) determining $q \approx E_1/v_i$ and plotting the so-obtained pairs of $[q, \hbar\omega_{\mathrm{ph}}(q)]$. Figure 68 shows such a plot obtained from various experimental data extant in the literature [215, 216, 223, 296, 297]. The experimental phonon dispersion is seen to fall nicely on the calculated dispersion curves, which are ab-initio calculated curves. They, in turn, describe very well recent inelastic X-ray data on graphite [3]. For more details of the evaluation, see [125].

11 Conclusions

Raman spectroscopy is a very important and useful tool for the study and characterization of carbon nanotubes. It has contributed tremendously to the understanding of these fascinating novel carbon allotropes. We have given a detailed overview of the effects of reducing graphite to one dimension,
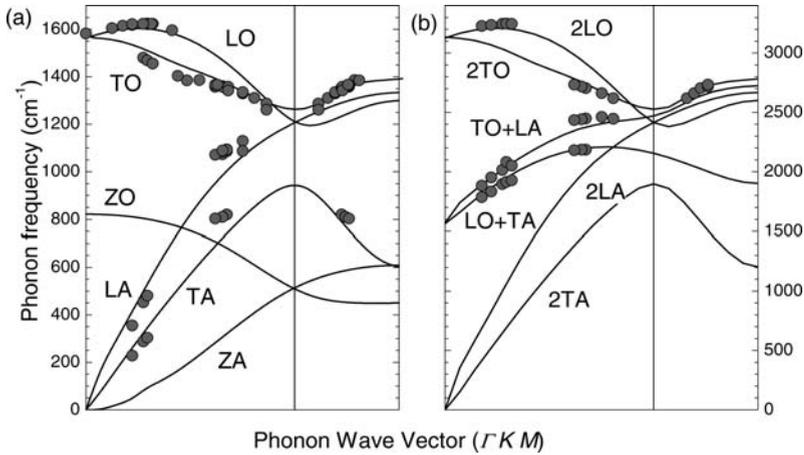
Fig. 68. (a) Phonon dispersion of graphite based on first-order disorder-induced double-resonant peaks in the Raman spectra. Data taken from various published experimental data in the literature, see [215, 216, 223, 296, 297] **(b)** Same as **(a)** but based on Raman peaks in the region of two-phonon spectra. *Solid lines* are dispersion curves from ab initio calculations [3] **(a)** or combinations and overtones with totally symmetric respresentations **(b)**. From [125]

which leads to the density-of-states singularities, to curvature-induced effects on the phonon frequencies, and to the classification of nanotubes into families and branches with similar physical properties. Most recent progress for both physics and technology is the identification of the chirality by resolving resonance Raman spectra as a function of excitation energy *and* wave-number shift in the experimental Kataura plots. Individual or bundled metallic and semiconducting nanotubes can now easily be identified. We have given a prescription for reliably identifying the chirality of an individual single-walled carbon nanotube. Recently, excitonic energies were determined experimentally, further enhancing the understanding of this fascinating class of materials.

Carbon nanotubes are a model system for one-dimensional solids. Throughout this Chapter we demonstrated how the geometry and the large aspect ratio, as well as electron and phonon confinement, can be studied by Raman spectroscopy. The most prominent example of how geometry changes the Raman spectra is the depolarization effect. Because of the anisotropic polarizability, the totally symmetric phonons strongly dominate scattering in carbon nanotubes. An exciting manifestation of electron and phonon confinement and the interaction between the confined quasiparticles are the phonon–plasmon coupled modes, the Kohn anomalies of several phonon branches and the Peierls distortion of very small diameter nanotubes. Much of this awaits final experimental verification.

From a spectroscopic point-of-view, the introduction of Raman double resonance as a process abundant in graphite-based materials has contributed much to their understanding. It provides a basis for the systematic analysis of defects and permits determination of the phonon dispersion in at least parts of the Brillouin zone. Extension to other suitable materials is conceivable.

In this Chapter we have presented the first attempts towards a unified description of the Raman effect in single-walled carbon nanotubes. This includes excitons as intermediate states in the Raman process, electron–phonon and electron–photon coupling. We expect many further studies to appear in the near future, in particular, turning away from the band-to-band transition picture towards a model accounting for the large electron–hole interaction in carbon nanotubes and the presence of excitons at room temperature.

Acknowledgements

References

[1] S. Iijima: Helical microtubules of graphitic carbon, Nature **354**, 56 (1991) 115, 122

[2] S. Iijima, T. Ichihasi: Single-shell carbon nanotubes of 1-nm diameter, Nature **363**, 603 (1993) 115, 122

[3] J. Maultzsch, S. Reich, C. Thomsen, H. Requardt, P. Ordejón: Phys. Rev. Lett. **92**, 075501 (2004) 116, 136, 139, 140, 143, 205, 215, 216

[4] C. Thomsen, S. Reich: Double-resonant Raman scattering in graphite, Phys. Rev. Lett. **85**, 5214 (2000) 116, 117, 163, 169, 170, 171, 172, 173, 207, 213, 214, 215

[5] P. R. Wallace: The band theory of graphite, Phys. Rev. **71**, 622 (1947) 116, 145, 146

[6] S. Reich, J. Maultzsch, C. Thomsen, P. Ordejón: Tight-binding description of graphene, Phys. Rev. B **66**, 035412 (2002) 116, 140, 144, 145, 146, 148, 149, 154, 181, 202

[7] V. N. Popov: New. J. Phys. **6**, 17 (2004) 116, 185

[8] D. Sánchez-Portal, E. Artacho, J. M. Soler, A. Rubio, P. Ordejón: *Ab initio* structural, elastic, and vibrational properties of carbon nanotubes, Phys. Rev. B **59**, 12678 (1999) 116, 137, 139, 141

[9] S. Reich, C. Thomsen, P. Ordejón: Electronic band structure of isolated and bundled nanotubes, Phys. Rev. B **65**, 155411 (2002) 116, 141, 142, 146, 148, 150, 185, 204

[10] C. D. Spataru, S. Ismail-Beigi, L. X. Benedict, S. G. Louie: Phys. Rev. Lett. **92**, 077402 (2004) 116, 150, 151, 158, 159

[11] V. Perebeinos, J. Tersoff, P. Avouris: Phys. Rev. Lett. **94**, 027402 (2005) 116, 161

[12] F. Wang, G. Dukovic, L. E. Brus, T. F. Heinz: The optical resonances in carbon nanotubes arise from excitons, Science **308**, 838 (2005) 116, 160, 161

[13] J. Maultzsch, C. Pomraenke, S. Reich, E. Chang, D. Prezzi, A. Ruini, E. Molinari, M. Strano, C. Thomsen, C. Lienau: Exciton binding energies from two-photon photoluminescence in single-walled carbon nanotubes, Phys. Rev. B **72**, 241402 (2005) 116, 158, 160, 161

[14] Q. Zhao, H. D. Wagner: Raman spectroscopy of carbon-nanotube-based composites, in A. C. Ferrari, J. Robertson (Eds.): *Raman Spectroscopy in Carbon: from Nanotubes to Diamond*, vol. 362, Philosophical Transactions of the Royal Society A (The Royal Society, London 2004) p. 2407 116

[15] R. Krupke, F. Hennrich, H. v. Löhneysen, M. M. Kappes: Science **301**, 344 (2003) 116

[16] S. Reich, L. Li, J. Robertson: Control the chirality of carbon nanotubes by epitaxial growth, Chem. Phys. Lett. **421**, 469–472 (2006) 116

[17] N. N. Ilichev: SWNTs as a passive Q-switches for self mode-locking of solid state lasers, in H. Kuzmany, J. Fink, M. Mehring, S. Roth (Eds.): *Electronic Properties of Novel Materials*, AIP Conference Proceedings (AIP, College Park 2005) 116

[18] A. B. Dalton, S. Collins, E. Muñoz, J. M. Razal., V. H. Ebron, J. P. Ferraris, J. N. Coleman, B. G. Kim, R. H. Baughman: Super-tough carbon-nanotube fibres – these extraordinary composite fibres can be woven into electronic textiles, Nature **423**, 703 (2003) 116

[19] R. H. Baughman, C. Cui, A. Zakhidov, Z. Iqbal, J. N. Barisci, G. M. Spinks, G. G. Wallace, A. Mazzoldi, D. D. Rossi, A. G. Rinzler, O. Jaschinski, S. Roth, M. Kertesz: Carbon nanotube actuators, Science **284**, 1340 (1999) 116, 193

[20] S. Reich, C. Thomsen, J. Maultzsch: *Carbon Nanotubes: Basic Concepts and Physical Properties* (Wiley-VCH, Berlin 2004) 116, 117, 126, 129, 131, 136, 137, 138, 141, 143, 144, 145, 146, 147, 148, 152, 153, 162, 169, 174, 176, 179, 199, 207

[21] M. S. Dresselhaus, G. Dresselhaus, P. C. Eklund: *Science of Fullerenes and Carbon Nanotubes* (Academic, San Diego 1995) 117, 129

[22] M. S. Dresselhaus, G. Dresselhaus, P. Avouris (Eds.): *Carbon Nanotubes: Synthesis, Structure, Properties, and Applications*, vol. 80, Topics in Applied Physics (Springer, Berlin, Heidelberg 2001) 117

[23] R. Saito, G. Dresselhaus, M. S. Dresselhaus: *Physical Properties of Carbon Nanotubes* (Imperial College Press, London 1998) 117, 129, 137, 144, 145, 146

[24] P. J. F. Harris: *Carbon Nanotubes and Related Structures* (Cambridge University Press, Cambridge 1999) 117

[25] T. Ando: Theory of electronic states and transport in carbon nanotubes, J. Phys. Soc. Jpn. **74**, 777 (2005) 117

[26] M. S. Dresselhaus, G. Dresselhaus, R. Saito, A. Jorio: Raman spectroscopy of carbon nanotubes, Phys. Rep. **409**, 47 (2005)   117, 162, 163, 168

[27] R. P. Raffaelle, B. J. Landi, J. D. Harris, S. G. Bailey, A. F. Hepp: Carbon nanotubes for power applications, Mater. Sci. Eng. B **116**, 233 (2005)   117

[28] J. Wang: Carbon-nanotube based electrochemical biosensors: A review, Electroanal. **17**, 7 (2005)   117

[29] U. D. Venkateswaran: Squeezing carbon nanotubes, phys. stat. sol. B **241**, 3345 (2004)   117

[30] C. Thomsen, H. Kataura (Eds.): *Focus on Carbon Nanotubes*, vol. 5, The New Journal of Physics (Institute of Physics and Deutsche Physikalische Gesellschaft, London 2003)   117

[31] A. C. Ferrari, J. Robertson (Eds.): *Raman Spectroscopy in Carbon: from Nanotubes to Diamond*, vol. 362, Philosophical Transactions of the Royal Society A (The Royal Society, London 2004)   117, 225

[32] Y. Baskin, L. Meyer: Lattice constant of graphite at low temperatures, Phys. Rev. B **100**, 544 (1955)   118

[33] Y. X. Zhao, I. L. Spain: X-ray diffraction data for graphite to 20 GPa, Phys. Rev. B **40**, 993 (1989)   118

[34] M. Hanfland, H. Beister, K. Syassen: Graphite under pressure: Equation of state and first-order Raman modes, Phys. Rev. B **39**, 12 598 (1989)   118

[35] J. C. Boettger: All-electron full-potential calculation of the electronic band structure, elastic constants, and equation of state for graphite, Phys. Rev. B **55**, 11202 (1997)   118

[36] J. Kürti, V. Zólyomi, M. Kertesz, G. Sun: New J. Phys. **5**, 125 (2003)   118, 130, 132, 133, 134

[37] A. Burian, J. Koloczek, J. Dore, A. Hannon, J. Nagy, A. Fonseca: Radial distribution function analysis of spatial atomic correlations in carbon nanotubes, Diam. Relat. Mater. **13**, 1261 (2004)   119

[38] S. Reich, C. Thomsen, P. Ordejón: Eigenvectors of chiral nanotubes, Phys. Rev. B **64**, 195416 (2001)   122, 130, 138, 139

[39] J.-C. Charlier, P. Lambin: Electronic structure of carbon nanotubes with chiral symmetry, Phys. Rev. B **57**, 15037 (1998)   122

[40] A. Thess, R. Lee, P. Nikolaev, H. Dai, P. Petit, J. Robert, C. Xu, Y. H. Lee, S. G. Kim, A. G. Rinzler, D. T. Colbert, G. E. Scuseria, D. Tománek, J. E. Fischer, R. E. Smalley: Crystalline ropes of metallic carbon nanotubes, Science **273**, 483 (1996)   122, 123

[41] K. Hata, D. N. Futaba, K. Mizuno, T. Namai, M. Yumura, S. Iijima: Water-assisted highly efficient synthesis of impurity-free single-walled carbon nanotubes, Science **306**, 1362 (2004)   123, 124

[42] L. X. Zheng, M. J. O'Connell, S. K. Doorn, X. Z. Liao, Y. H. Zhao, E. A. Akhadov, M. A. Hoffbauer, B. J. Roop, Q. X. Jia, R. C. Dye, D. E. Peterson, S. M. Huang, J. Liu, et al.: Ultralong single-wall carbon nanotubes, Nature Mater. **3**, 673 (2004)   124

[43] M. J. Bronikowski, P. A. Willis, D. T. Colbert, K. A. Smith, R. E. Smalley: J. Vac. Sci. Technol. A **19**, 1800 (2001)   124

[44] S. M. Bachilo, L. Balzano, J. E. Herrera, F. Pompeo, D. E. Resasco, R. B. Weisman: J. Am. Chem. Soc. **125**, 11186 (2003)   122, 123, 124, 125, 159

[45] Y. Miyauchi, S. Chiashi, Y. Murakami, Y. Hayashida, S. Maruyama: Chem. Phys. Lett. **387**, 198 (2004)   122, 124, 125, 158, 159

[46] N. Wang, Z. K. Tang, G. D. Li, J. S. Chen: Single-walled 4 Å carbon nanotube arrays, Nature (London) **408**, 50 (2000)   124, 174

[47] R. R. Bacsa, A. Peigney, C. Laurent, P. Puech, W. S. Bacsa: Phys. Rev. B **65**, 161404 (2002)   124, 136, 177

[48] S. Bandow, M. Takizawa, K. Hirahara, M. Yudasaka, S. Iijima: Chem. Phys. Lett. **337**, 48 (2001)   124

[49] T. W. Ebbesen, P. M. Ajayan: Large-scale synthesis of carbon nanotubes, Nature **358**, 220 (1992)   122

[50] D. S. Bethune, C. H. Kiang, M. S. deVries, G. Gorman, R. Savoy, J. Vazques, R. Beyers: Cobalt-catalyzed growth of carbon nanotubes with single-atomic-layer, Nature **363**, 605 (1993)   122

[51] C. Journet, W. K. Maser, P. Bernier, A. Loiseau, M. L. de la Chapelle, S. Lefrant, P. Deniard, R. Lee, J. E. Fischer: Large-scale production of single-walled carbon nanotubes by the electric-arc technique, Nature **388**, 756 (1997)   122

[52] H. Dai: in M. S. Dresselhaus, G. Dresselhaus, P. Avouris (Eds.): *Carbon Nanotubes*, vol. 80, Topics in Applied Physics (Springer, Berlin, Heidelberg 2001) p. 29   122

[53] M. Terrones: Carbon nanotubes: synthesis and properties, electronic devices and other emerging applications, Int. Mater. Rev. **49**, 325 (2005)   122

[54] A. A. Puretzky, D. B. Geohegan, S. Jesse, I. N. Ivanov, G. Eres: In situ measurements and modeling of carbon nanotube array growth kinetics during chemical vapor deposition, Appl. Phys. A: Mater. Sci. Process. **81**, 223 (2005)   122

[55] M. C. Schabel, J. L. Martins: Energetics of interplanar binding in graphite, Phys. Rev. B **46**, 7185 (1992)   123

[56] L. A. Girifalco, M. Hodak: Van der Waals binding energies in graphitic structures, Phys. Rev. B **65**, 125404 (2002)   123

[57] R. Z. H. Ulbricht, T. Hertel: Interlayer cohesive energy of graphite from thermal desorption of polyaromatic hydrocarbons, Phys. Rev. B **69**, 155406 (2004)   123

[58] S. Reich, C. Thomsen, P. Ordejón: Phys. Rev. B **65**, 153407 (2002)   123

[59] M. J. O'Connell, S. M. Bachilo, C. B. Huffman, V. C. Moore, M. S. Strano, E. H. Haroz, K. L. Rialon, P. J. Boul, W. H. Noon, C. Kittrell, J. Ma, R. H. Hauge, R. B. Weisman, R. E. Smalley: Band gap fluorescence from individual single-walled carbon nanotubes, Science **297**, 593 (2002)   123, 144, 157, 177

[60] S. M. Bachilo, M. S. Strano, C. Kittrell, R. H. Hauge, R. E. Smalley, R. B. Weisman: Structure-assigned optical spectra of single-walled carbon nanotubes, Science **298**, 2361 (2002)   123, 144, 151, 154, 155, 157, 158, 159, 160, 161, 178, 179, 185

[61] S. Lebedkin, F. Hennrich, T. Skipa, M. M. Kappes: Near-infrared photoluminescence of single-walled carbon nanotubes prepared by the laser vaporization method, J. Phys. Chem. B **107**, 1949 (2003)   123, 155, 159

[62] T. Hertel, A. Hagen, V. Talalaev, K. Arnold, F. Hennrich, M. Kappes, S. Rosenthal, J. McBride, H. Ulbricht, E. Flahaut: Spectroscopy of single- and double-wall carbon nanotubes in different environments, Nano Lett. **5**, 511 (2005) 123

[63] H. Telg, J. Maultzsch, S. Reich, F. Hennrich, C. Thomsen: Phys. Rev. Lett. **93**, 177401 (2004) 123, 136, 154, 155, 158, 159, 160, 161, 179, 180, 181, 182, 183, 197, 202

[64] C. Fantini, A. Jorio, M. Souza, M. S. Strano, M. S. Dresselhaus, M. A. Pimenta: Phys. Rev. Lett. **93**, 147406 (2004) 123, 154, 155, 158, 159, 179, 180, 184, 197, 202

[65] M. S. Strano, S. K. Doorn, E. H. Haroz, C. Kittrell, R. H. Hauge, R. E. Smalley: Assignment of (n, m) Raman and optical features of metallic single-walled carbon nanotubes, Nano Lett. **3**, 1091 (2003) 123, 179, 185, 197

[66] Z. F. Ren, Z. P. Huang, J. W. Xu, J. H. Wang, P. Bush, M. P. Siegal, P. N. Provencio: Synthesis of large arrays of well-aligned carbon nanotubes on glass, Science **282**, 1105 (1998) 124

[67] M. Chhowalla, K. B. K. Teo, C. Ducati, N. L. Rupesinghe, G. A. J. Amaratunga, A. C. Ferrari, D. Roy, J. Robertson, W. I. Milne: Growth process conditions of vertically aligned carbon nanotubes using plasma enhanced chemical vapor deposition, Appl. Phys. Lett. **90**, 5308 (2001) 124

[68] J. Lefebvre, Y. Homma, P. Finnie: Bright band gap photoluminescence from unprocessed single-walled carbon nanotubes, Phys. Rev. Lett. **90**, 217401 (2003) 124, 155, 159

[69] J. C. Meyer, M. Paillet, G. S. Duesberg, S. Roth: Electron diffraction analysis of individual single-walled carbon nanotubes, Ultramicroscopy **106**, 176 (2005) 124

[70] S. Hofmann, C. Ducati, B. Kleinsorge, J. Robertson: Direct growth of aligned carbon nanotube field emitter arrays onto plastic substrates, Appl. Phys. Lett. **83**, 4661 (2003) 124

[71] L. Guan, K. Suenaga, Z. Shi, Z. Gu, S. Iijima: Direct imaging of the alkali metal site in K-doped fullerene peapods, Phys. Rev. Lett. **94**, 045502 (2005) 125

[72] L. Henrard, A. Loiseau, C. Journet, P. Bernier: Synth. Met. **103**, 2533 (1999) 125

[73] L. Henrard, A. Loiseau, C. Journet, P. Bernier: Study of the symmetry of single-wall nanotubes by electron diffraction, Eur. Phys. B **13**, 661 (2000) 125

[74] S. Reich, C. Thomsen, J. Robertson: Exciton resonances quench the photoluminescence of zigzag carbon nanotubes, Phys. Rev. Lett. **95**, 077402 (2005) 125, 160, 161, 179, 201

[75] J. Jiang, R. Saito, A. Grüneis, S. G. Chou, G. G. Samsonidze, A. Jorio, G. Dresselhaus, M. S. Dresselhaus: Photoexcited electron relaxation processes in single-wall carbon nanotubes, Phys. Rev. B **71**, 045417 (2005) 125, 161, 168, 207

[76] B. W. Smith, M. Monthioux, D. E. Luzzi: Encapsulated C_{60} in carbon nanotubes, Nature **396**, 323 (1998) 125

[77] H. Kataura, Y. Maniwa, T. Kodama, K. Kikuchi, K. Hirahara, K. Suenaga, S. Iijima, S. Suzuki, Y. Achiba, W. Kratschmer: Synth. Met. **121**, 1195 (2001) 125

[78] T. Pichler, H. Kuzmany, H. Kataura, Y. Achiba: Metallic polymers of C_{60} inside single-walled carbon nanotubes, Phys. Rev. Lett. **87**, 267401 (2001) 125

[79] J. Sloan, M. C. Novotny, S. R. Bailey, G. Brown, C. Xu, V. C. Williams, S. Friedrichs, E. Flahaut, R. L. Callender, A. P. E. York, K. S. Coleman, M. L. H. Green, R. E. Dunin-Borkowskib, J. L. Hutchison: Two layer 4:4 coordinated KI crystals grown within single walled carbon nanotubes, Chem. Phys. Lett. **329**, 61 (2000) 125, 126

[80] J. Diefenbach, T. P. Martin: Model calculations of alkali halide clusters, J. Chem. Phys. **83**, 4585 (1985) 126

[81] M. Damnjanović, I. Milošević, T. Vuković, R. Sredanović: Full symmetry, optical activity, and potentials of single-wall and multiwall nanotubes, Phys. Rev. B **60**, 2728 (1999) 126, 127, 129, 138, 148

[82] M. Damnjanović, I. Milošević, T. Vuković, R. Sredanović: Symmetry and lattices of single-wall nanotubes, J. Phys. A **32**, 4097 (1999) 126, 129

[83] J. W. Mintmire, B. I. Dunlap, C. T. White: Are fullerene tubules metallic?, Phys. Rev. Lett. **68**, 631 (1992) 127, 144, 148

[84] M. Damnjanović, T. Vuković, I. Milošević: Modified group projectors: Tight binding method, J. Phys. A: Math. Gen. **33**, 6561 (2000) 127

[85] J. Maultzsch, S. Reich, C. Thomsen, E. Dobardžić, I. Milošević, M. Damnjanović: Phonon dispersion of carbon nanotubes, Solid State Commun. **121**, 471 (2002) 127, 143, 148, 191

[86] T. Vuković, I. Milošević, M. Damnjanović: Carbon nanotubes band assignation, topology, Bloch states, and selection rules, Phys. Rev. B **65**, 045418 (2002) 127, 143, 148

[87] I. Milošević, T. Vuković, S. Dmitrović, M. Damnjanović: Phys. Rev. B **67**, 165418 (2003) 127, 148, 152, 153

[88] E. Chang, G. Bussi, A. Ruini, E. Molinari: Excitons in carbon nanotubes: An ab initio symmetry-based approach, Phys. Rev. Lett. **92**, 196401 (2004) 127, 150

[89] T. Inui, Y. Tanabe, Y. Onodera: *Group Theory and its Application in Physics* (Springer Verlag, Berlin Heidelberg New York 1996) 127, 129

[90] E. B. Wilson, J. C. Decius, P. C. Cross: *Molecular Vibrations* (Dover, New York 1980) 127, 129

[91] M. S. Dresselhaus, G. Dresselhaus, R. Saito: Carbon fibers based on C_{60} and their symmetry, Phys. Rev. B **45**, 6234 (1992) 129

[92] R. A. Jishi, M. S. Dresselhaus, G. Dresselhaus: Symmetry properties of chiral carbon nanotubes, Phys. Rev. B **47**, 16671 (1993) 129

[93] M. S. Dresselhaus, P. C. Eklund: Adv. Phys. **49**, 705 (2000) 129

[94] A. Jorio, R. Saito, G. Dresselhaus, M. S. Dresselhaus: Determination of nanotube properties by Raman spectroscopy, in A. C. Ferrari, J. Robertson (Eds.): *Raman Spectroscopy in Carbons: From Nanotubes to Diamond* (Philosophical Transaction of the Royal Society 2004) p. 2311 129, 168

[95] R. A. Jishi, L. Venkataraman, M. S. Dresselhaus, G. Dresselhaus: Phonon modes in carbon nanotubules, Chem. Phys. Lett. **209**, 77–82 (1993) 129, 131

[96] D. L. Rousseau, R. P. Bauman, S. P. S. Porto: Normal mode determination in crystals, J. Raman Spectrosc. **10**, 253 (1981) 129

[97] A. Fainstein, P. Etchegoin, M. P. Chamberlain, M. Cardona, K. Tötemeyer, K. Eberl: Selection rules and dispersion of GaAs/AlAs multiple-quantum-well optical phonons studied by Raman scattering in right-angle, forward, and backscattering in-plane geometries, Phys. Rev. B **51**, 14 448 (1995) 130

[98] B. Jusserand, M. Cardona: Superlattices and other microstructures, in M. Cardona, G. Güntherodt (Eds.): *Light Scattering in Solids V*, vol. 66, Topics in Applied Physics (Springer, Berlin 1989) p. 49 130, 140

[99] G. S. Duesberg, I. Loa, M. Burghard, K. Syassen, S. Roth: Polarized Raman spectroscopy of individual single-wall carbon nanotubes, Phys. Rev. Lett. **85**, 5436 (2000) 130, 144, 175, 206, 207

[100] A. Ugawa, A. G. Rinzler, D. B. Tanner: Far-infrared gaps in single-wall carbon nanotubes, Phys. Rev. B **60**, R11 305 (1999) 130

[101] S. Reich, C. Thomsen, G. S. Duesberg, S. Roth: Intensities of the Raman active modes in single and multiwall nanotubes, Phys. Rev. B **63**, R041401 (2001) 130, 144, 175

[102] A. Jorio, A. G. S. Filho, V. W. Brar, A. K. Swan, M. S. Ünlü, B. B. Goldberg, A. Righi, J. H. Hafner, C. M. Lieber, R. Saito, G. Dresselhaus, M. S. Dresselhaus: Phys. Rev. B **65**, 121402 (2002) 130

[103] E. Dobardžić, I. M. B. Nikolić, T. Vuković, M. Damnjanović: Single-wall carbon nanotubes phonon spectra: Symmetry-based calculations, Phys. Rev. B **68**, 045 408 (2003) 130, 131, 138, 141, 191

[104] M. Damnjanović, E. Dobardžić, I. Milošević: Chirality dependence of the radial breathing mode: a simple model, J. Phys.: Condens. Matter **16**, L505 (2004) 130, 131

[105] G. D. Mahan: Phys. Rev. B **65**, 235402 (2002) 130

[106] R. Nicklow, N. Wakabayashi, H. G. Smith: Lattice dynamics of pyrolytic graphite, Phys. Rev. B **5**, 4951 (1972) 131

[107] O. L. Blakslee, D. G. Proctor, E. J. Seldin, G. B. Spence, T. Weng: Elastic constants of compression-annealed pyrolytic graphite, J. Appl. Phys. **41**, 3373 (1970) 131

[108] E. J. Seldin, C. W. Nezbeda: Elastic constants and electron-microscope observations of neutron-irradiated compression-annealed pyrolytic and single-crystal graphite, J. Appl. Phys. **41**, 3389 (1970) 131

[109] L. Wirtz, A. Rubio, R. A. de la Concha, A. Loiseau: Phys. Rev. B **68**, 45425 (2003) 131

[110] S. Niyogi, M. A. Hamon, H. Hu, B. Zhao, P. Bhowmik, R. Sen, M. E. Itkis, R. Haddon: Chemistry of single-walled nanotubes, Acc. Chem. Res. **35**, 1105 (2002) 132

[111] A. Jorio, C. Fantini, M. A. Pimenta, R. B. Capaz, G. G. Samsonidze, G. Dresselhaus, M. S. Dresselhaus, J. Jiang, N. Kobayashi, A. Grüneis, R. Saito: Resonance Raman spectroscopy (n, m)-dependent effects in small-diameter single-wall carbon nanotubes, Phys. Rev. B **71**, 075 401 (2005) 133, 134, 158, 179, 185, 197, 202

[112] V. N. Popov, L. Henrard: Phys. Rev. B **65**, 235415 (2002) 134, 135

[113] E. Dobardžić, J. Maultzsch, I. Milošević, C. Thomsen, M. Damnjanović: phys. stat. sol. (b) **237**, R7 (2003) 135

[114] G. Wu, J. Zhou, J. Dong: Radial-breathing-like phonon modes of double-walled carbon nanotubes, Phys. Rev. B **72**, 115 418 (2005) 135

[115] C. Kramberger, R. Pfeiffer, H. Kuzmany, V. Zólyomi, J. Kürti: Assignment of chiral vectors in carbon nanotubes, Phys. Rev. B **68**, 235 404 (2003)   135, 177

[116] R. Pfeiffer, H. Kuzmany, C. Kramberger, C. Schaman, T. Pichler, H. Kataura, Y. Achiba, J. Kürti, V. Zólyomi: Phys. Rev. Lett. **90**, 225501 (2003)   135, 177

[117] A. Kasuya, Y. Sasaki, Y. Saito, K. Tohji, Y. Nishina: Evidence for size-dependent discrete dispersions in single-wall nanotubes, Phys. Rev. Lett. **78**, 4434 (1997)   137, 139

[118] O. Dubay, G. Kresse: Accurate density functional calculations for the phonon dispersion relations of graphite layer and carbon nanotubes, Phys. Rev. B **67**, 035 401 (2003)   137, 139, 141, 191

[119] C. Thomsen, S. Reich, P. Ordejón: *Ab initio* determination of the phonon deformation potentials of graphene, Phys. Rev. B **65**, 073403 (2002)   137

[120] S. A. Solin, A. K. Ramdas: Raman spectrum of diamond, Phys. Rev. B **1**, 1687 (1970)   138

[121] J. Kulda, H. Kainzmaier, D. Strauch, B. Dorner, M. Lorenzen, M. Krisch: Phys. Rev. B **66**, 241202(R) (2002)   138

[122] S. Reich, A. C. Ferrari, R. Arenal, A. Loiseau, I. Bello, J. Robertson: Resonant Raman scattering in cubic and hexagonal boron nitride, Phys. Rev. B **71**, 205201 (2005)   138

[123] G. Kern, G. Kress, J. Hafner: *Ab-initio* lattice dynamics and phase diagram of boron nitride, Phys. Rev. B **59**, 8851 (1999)   138

[124] S. Reich, H. Jantoljak, C. Thomsen: Shear strain in carbon nanotubes under hydrostatic pressure, Phys. Rev. B **61**, R13 389 (2000)   138

[125] S. Reich, C. Thomsen: Raman spectroscopy of graphite, in A. C. Ferrari, J. Robertson (Eds.): *Raman Spectroscopy in Carbons: From Nanotubes to Diamond* (Philosophical Transaction of the Royal Society 2004) p. 2271   139, 171, 173, 205, 207, 213, 214, 215, 216

[126] R. Saito, A. Jorio, J. H. Hafner, C. M. Lieber, M. Hunter, T. McClure, G. Dresselhaus, M. S. Dresselhaus: Chirality-dependent *G*-band Raman intensity of carbon nanotubes, Phys. Rev. B **64**, 085312 (2001)   139

[127] S. Piscanec, M. Lazzeri, F. Mauri, A. C. Ferrari, J. Robertson: Phys. Rev. Lett. **93**, 185503 (2004)   139, 140, 143, 205, 206, 207

[128] M. Lazzeri, S. Piscanec, F. Mauri, A. C. Ferrari, J. Robertson: Electron transport and hot phonons in carbon nanotubes, Phys. Rev. Lett. **95**, 236802 (2005)   139

[129] J. Maultzsch, S. Reich, U. Schlecht, C. Thomsen: High-energy phonon branches of an individual metallic carbon nanotube, Phys. Rev. Lett. **91**, 087402 (2003)   139, 172, 192, 193, 212

[130] Z. M. Li, V. N. Popov, Z. K. Tang: A symmetry-adapted force-constant lattice-dynamical model for single-walled carbon nanotubes, Solid State Commun. **130**, 657 (2005)   139

[131] S. D. M. Brown, A. Jorio, P. Corio, M. S. Dresselhaus, G. Dresselhaus, R. Saito, K. Kneipp: Origin of the Breit-Wigner-Fano lineshape of the tangential *G*-band feature of metallic carbon nanotubes, Phys. Rev. B **63**, 155414 (2001)   139, 190

[132] K. Kempa: Phys. Rev. B **66**, 195406 (2002)   139, 190, 191

[133] O. Dubay, G. Kresse, H. Kuzmany: Phys. Rev. Lett. **88**, 235506 (2002) 139, 140, 141, 190, 191, 196, 207

[134] P. Y. Yu, M. Cardona: *Fundamentals of Semiconductors* (Springer-Verlag, Berlin 1996) 140, 152, 158, 159, 196

[135] X. Blase, L. X. Benedict, E. L. Shirley, S. G. Louie: Hybridization effects and metallicity in small radius carbon nanotubes, Phys. Rev. Lett. **72**, 1878 (1994) 140, 150

[136] M. Damnjanović, T. Vuković, I. Milošević: Fermi level quantum numbers and secondary gap of conducting carbon nanotubes, Solid State Commun. **116**, 265 (2000) Table 1 in the reference contains a small error: For chiral tubes and the $\tilde{k}$ quantum numbers $\tilde{k}_F = 2q\pi/3na$ for $\mathcal{R} = 3$ tubes and $\tilde{k}_F = 0$ for $\mathcal{R} = 1$ nanotubes. 140, 143

[137] A. Kleiner, S. Eggert: Curvature, hybridization, and STM images of carbon nanotubes, Phys. Rev. B **64**, 113402 (2001) 140

[138] W. Kohn: Image of the Fermi Surface in the Vibration Spectrum of a Metal, Phys. Rev. Lett. **2**, 393 (1959) 140, 204, 205

[139] M. V. Klein: Raman studies of phonon anomalies in transition-metal compounds, in M. Cardona, G. Güntherodt (Eds.): *Light Scattering in Solids III*, vol. 51, Topics in Applied Physics (Springer, Berlin 1982) p. 121 140, 206

[140] K.-P. Bohnen, R. Heid, H. J. Liu, C. T. Chan: Lattice dynamics and electron-phonon interaction in (3,3) carbon nanotubes, Phys. Rev. Lett. **93**, 245501 (2004) 140, 143, 191, 205, 206

[141] S. Piscanec, M. Lazzeri, A. C. Ferrari, F. Mauri, J. Robertson: private communication 140, 142, 143, 191, 205, 206, 207

[142] D. Connétable, G.-M. Rignanese, J.-C. Charlier, X. Blase: Room temperature Peierls distortion in small diameter nanotubes, Phys. Rev. Lett. **94**, 015503 (2005) 140, 143, 191, 205, 206

[143] J. Kürti, G. Kresse, H. Kuzmany: First-principles calculations of the radial breathing mode of single-wall carbon nanotubes, Phys. Rev. B **58**, 8869 (1998) 141

[144] M. Machón, S. Reich, H. Telg, J. Maultzsch, P. Ordejón, C. Thomsen: Phys. Rev. B **71**, 35416 (2005) 141, 158, 197, 198, 199, 200, 203

[145] C. Thomsen: Second-order Raman spectra of single and multi-walled carbon nanotubes, Phys. Rev. B **61**, 4542 (2000) 142, 162, 163, 212, 214, 215

[146] A. C. Ferrari, J. Robertson: Raman spectroscopy of amorphous, nanostructured, diamond-like carbon, and nanodiamond, in (2004) p. 2477 of Ref. [31] 143

[147] H. H. Gommans, J. W. Alldredge, H. Tashiro, J. Park, J. Magnuson, A. G. Rinzler: Fibers of aligned single-walled carbon nanotubes: Polarized Raman spectroscopy, J. Appl. Phys. **88**, 2509 (2000) 144, 175

[148] N. Hamada, S.-I. Sawada, A. Oshiyama: New one-dimensional conductors: Graphitic microtubules, Phys. Rev. Lett. **68**, 1579 (1992) 144, 150

[149] R. Saito, M. Fujita, G. Dresselhaus, M. S. Dresselhaus: Electronic structure of graphene tubules based on C_{60}, Phys. Rev. B **46**, 1804 (1992) 144, 150

[150] S. Reich, C. Thomsen: Chirality dependence of the density-of-states singularities in carbon nanotubes, Phys. Rev. B **62**, 4273 (2000) 144, 155, 156, 157, 181, 202

[151] G. G. Samsonidze, R. Saito, A. Jorio, M. A. Pimenta, A. G. Souza, A. Gruneis, G. Dresselhaus, M. S. Dresselhaus: The concept of cutting lines in carbon nanotube science, J. Nanosci. Nanotech. **3**, 431 (2003)   144

[152] R. F. Willis, B. Feuerbacher, B. Fitton: Graphite conduction band states from secondary electron emission spectra, Phys. Lett. A **34**, 231 (1971)   146

[153] J. W. Mintmire, C. T. White: Universal density of states for carbon nanotubes, Phys. Rev. Lett. **81**, 2506 (1998)   149, 152, 155, 167

[154] M. Machon, S. Reich, C. Thomsen, D. Sánchez-Portal, P. Ordejón: Phys. Rev. B **66**, 155410 (2002)   150, 152, 206

[155] Z. M. Li, Z. K. Tang, H. J. Liu, N. Wang, C. T. Chan, R. Saito, S. Okada, G. D. Li, J. S. Chen, N. Nagasawa, S. Tsuda: Polarized absorption spectra of single-walled 4 Å carbon nanotubes aligned in channels of an AlPO$_4$-5 single crystal, Phys. Rev. Lett. **87**, 127401 (2001)   150

[156] T. Miyake, S. Saito: Quasiparticle band structure of carbon nanotubes, Phys. Rev. B **68**, 155424 (2003)   150

[157] V. Barone, G. E. Scuseria: Theoretical study of the electronic properties of narrow single-walled carbon nanotubes: Beyond the local density approximation, J. Chem. Phys. **121**, 10376 (2004)   150

[158] V. N. Popov, L. Henrard: Comparative study of the optical properties of single-walled carbon nanotubes within orthogonal and nonorthogonal tight-binding models, Phys. Rev. B **70**, 115470 (2004)   150

[159] V. Zólyomi, J. Kürti: First-principles calculations for the electronic band structures of small diameter single-wall carbon nanotubes, Phys. Rev. B **70**, 085403 (2004)   150

[160] V. Perebeinos, J. Tersoff, P. Avouris: Phys. Rev. Lett. **92**, 257402 (2004)   151, 158, 159, 160

[161] H. Zhao, S. Mazumdar: Electron-electron interaction effects on the optical excitations of semiconducting single-walled carbon nanotubes, Phys. Rev. Lett. **95**, 157 402 (2005)   151, 158, 179

[162] A. Grüneis, R. Saito, G. G. Samsonidze, T. Kimura, M. A. Pimenta, A. Jorio, A. G. S. Filho, G. Dresselhaus, M. S. Dresselhaus: Phys. Rev. B **67**, 165402 (2003)   151, 152, 158

[163] C. T. White, J. W. Mintmire: Density of states reflects diameter in nanotubes, Nature (London) **394**, 29 (1998)   152, 155

[164] T. W. Odom, J. L. Huang, P. Kim, C. M. Lieber: Atomic structure and electronic properties of single-walled carbon nanotubes, Nature **391**, 62 (1998)   152, 177

[165] J. W. G. Wildöer, L. C. Venema, A. G. Rinzler, R. E. Smalley, C. Dekker: Electronic structure of atomically resolved carbon nanotubes, Nature **391**, 59 (1998)   152, 177

[166] H. Ajiki, T. Ando: Carbon nanotubes: Optical absorption in Aharonov-Bohm flux, Jpn. J. Appl. Phys. **Suppl. 34-1**, 107 (1994)   153, 174

[167] H. Kataura, Y. Kumazawa, Y. Maniwa, I. Umezu, S. Suzuki, Y. Ohtsuka, Y. Achiba: Optical properties of single-wall carbon nanotubes, Synth. Met. **103**, 2555 (1999)   154, 155

[168] P. M. Rafailov, H. Jantoljak, C. Thomsen: Electronic transitions in single-walled carbon nanotubes: A resonance Raman study, Phys. Rev. B **61**, 16 179 (2000)   154, 163, 168, 188, 189

[169] R. Saito, G. Dresselhaus, M. S. Dresselhaus: Trigonal warping effect of carbon nanotubes, Phys. Rev. B **61**, 2981 (2000)   155, 157

[170] V. N. Popov, L. Henrard, P. Lambin: Nano Lett. **4**, 1795 (2004)   158, 160, 197, 199

[171] R. B. Capaz, C. D. Spataru, P. Tagney, M. L. Cohen, S. G. Louie: Temperature dependence of the band gap of semiconducting carbon nanotubes, Phys. Rev. Lett. **94**, 036801 (2005)   158

[172] X.-F. He: Excitons in anisotropic solids: The model of fractional-dimensional space, Phys. Rev. B **43**, 2063 (1991)   158

[173] P. Lefebvre, P. Cristol, H. Mathieu: Unified formulation of excitonic spectra of semiconductor quantum wells, superlattices, and quantum wires, Phys. Rev. B **48**, 17308 (1993)   158

[174] C. L. Kane, E. J. Mele: Phys. Rev. Lett. **93**, 197402 (2004)   158, 159, 160, 179

[175] S. G. Chou, F. Plentz, J. Jiang, R. Saito, D. Nezich, H. B. Ribeiro, A. Jorio, M. A. Pimenta, G. G. Samsonidze, A. P. Santos, M. Zheng, G. B. Onoa, E. D. Semke, G. Dresselhaus, M. S. Dresselhaus: Phonon-assisted excitonic recombination channels observed in DNA-wrapped carbon nanotubes using photoluminescence spectroscopy, Phys. Rev. Lett. **94**, 127402 (2005)   161

[176] S. Lebedkin, K. Arnold, F. Hennrich, R. Krupke, B. Renker, M. M. Kappes: FTIR-luminescence mapping of dispersed single-walled carbon nanotubes, New J. Phys. **5**, 140 (2003)   161

[177] X. H. Qiu, M. Freitag, V. Perebeinos, P. Avouris: Photoconductivity spectra of single-carbon nanotubes: Implications on the nature of their excited states, Nano Lett. **5**, 749 (2005)   161

[178] J.-S. Lauret, C. Voisin, G. Cassabois, C. Delalande, P. Roussignol, O. Jost, L. Capes: Phys. Rev. Lett. **90**, 57404 (2003)   161

[179] T. Hertel, G. Moos: Phys. Rev. Lett. **84**, 5002 (2000)   161

[180] G. N. Ostojic, S. Zaric, J. Kono, M. S. Strano, V. C. Moore, R. H. Hauge, R. E. Smalley: Phys. Rev. Lett. **92**, 117402 (2004)   161

[181] S. Reich, M. Dworzak, A. Hoffmann, C. Thomsen, M. S. Strano: Excited-state carrier lifetime in single-walled carbon nanotubes, Phys. Rev. B **71**, 033402 (2005)   161

[182] O. J. Korovyanko, C.-X. Sheng, Z. V. Vardeny, A. B. Dalton, R. H. Baughman: Phys. Rev. Lett. **92**, 17403 (2004)   161

[183] M. Cardona, G. Güntherodt (Eds.): *Light Scattering in Solids I–VIII* (Springer, Berlin, Heidelberg 1982–2000)   162

[184] M. Cardona: Resonance phenomena, in M. Cardona, G. Güntherodt (Eds.): *Light Scattering in Solids II*, vol. 50, Topics in Applied Physics (Springer, Berlin 1982) p. 19   162, 165, 166, 169, 196

[185] R. M. Martin, L. M. Falicov: Resonant Raman scattering, in M. Cardona (Ed.): *Light Scattering in Solids I: Introductory Concepts*, vol. 8, 2nd ed., Topics in Applied Physics (Springer-Verlag, Berlin Heidelberg New York 1983) p. 79   162, 165, 166, 167, 170

[186] J. Maultzsch: *Vibrational properties of carbon nanotubes and graphite*, Ph.D. thesis, Technische Universität Berlin, Berlin (2004)   162

[187] A. M. Rao, E. Richter, S. Bandow, B. Chase, P. C. Eklund, K. A. Williams, S. Fang, K. R. Subbaswamy, M. Menon, A. Thess, R. E. Smalley, G. Dresselhaus, M. S. Dresselhaus: Diameter-selective Raman scattering from vibrational modes in carbon nanotubes, Science **275**, 187 (1997) 162, 163, 188

[188] M. A. Pimenta, A. Marucci, S. A. Empedocles, M. G. Bawendi, E. B. Hanlon, A. M. Rao, P. C. Eklund, R. E. Smalley, G. Dresselhaus, M. S. Dresselhaus: Raman modes of metallic carbon nanotubes, Phys. Rev. B **58**, R16 016 (1998) 162, 163, 188

[189] M. Milnera, J. Kürti, M. Hulman, H. Kuzmany: Periodic resonance excitation and intertube interaction from quasicontinuous distributed helicities in single-wall carbon nanotubes, Phys. Rev. Lett. **84**, 1324 (2000) 162

[190] R. R. Schlittler, J. W. Seo, J. K. Gimzewski, C. Durkan, M. S. M. Saifullah, M. E. Welland: Science **292**, 1136 (2001) 163

[191] M. F. Chisholm, Y. H. Wang, A. R. Lupini, G. Eres, A. A. Puretzky, B. Brinson, A. V. Melechko, D. B. Geohegan, H. T. Cui, M. P. Johnson, S. J. Pennycook, D. H. Lowndes, S. Arepalli, C. Kittrell, S. Sivaram, M. Kim, G. Lavin, J. Kono, R. Hauge, R. E. Smalley: Science **300**, 5623 (2001) 163

[192] M. E. Welland, C. Durkan, M. S. M. Saifullah, J. W. Seo, R. R. Schlittler, J. K. Gimzewski: Science **300**, 1236 (2001) 163

[193] S. Hofmann, C. Ducati, J. Robertson: Low-temperature self-assembly of novel encapsulated compound nanowires, Adv. Mater. **14**, 1821 (2002) 163

[194] J. Maultzsch, S. Reich, C. Thomsen: Raman scattering in carbon nanotubes revisited, Phys. Rev. B **65**, 233402 (2002) 163, 169, 175, 192, 196, 208, 212, 214

[195] Y. Miyauchi, S. Maruyama: Identification of excitonic phonon sideband by photoluminescence spectroscopy of single-walled carbon-13 nanotubes, Phys. Rev. Lett. (2005) submitted, cond-mat/0508232 163, 164

[196] C. Fantini, A. Jorio, M. Souza, L. Ladeira, A. S. Filho, R. Saito, G. Samsonidze, G. Dresselhaus, M. S. Dresselhaus, M. A. Pimenta: One-dimensional character of combination modes in the resonance Raman scattering of carbon nanotubes, Phys. Rev. Lett. **93**, 087401 (2004) 163

[197] F. Simon, C. Kramberger, R. Pfeiffer, H. Kuzmany, V. Zólyomi, J. Kürti, P. M. Singer, H. Alloul: Isotope engineering of carbon nanotube systems, Phys. Rev. Lett. **95**, 017401 (2005) 164

[198] G. Bussi, J. Menéndez, J. Ren, M. Canonico, E. Molinari: Quantum interferences in the Raman cross section for the radial breathing mode in metallic carbon nanotubes, Phys. Rev. B **71**, 041404 (2005) 165

[199] C. Trallero-Giner, A. Cantarero, M. Cardona, M. Mora: Phys. Rev. B **45**, 6601 (1992) 165

[200] M. Canonico, G. B. Adams, C. Poweleit, J. Menéndez, J. B. Page, G. Harris, H. P. van der Meulen, J. M. Calleja, J. Rubio: Phys. Rev. B **65**, 201402(R) (2002) 166, 168, 203, 204

[201] G. Bussi, J. Menéndez, J. Ren, M. Canonico, E. Molinari: Quantum interferences in the Raman cross section for the radial breathing mode in metallic carbon nanotubes, Phys. Rev. B **71**, 041404 (2005) 166, 167, 168, 199, 202, 203, 204

[202] J. Mathews, R. L. Walker: *Mathematical Methods of Physics*, 2nd ed. (Addison-Wesley, Redwood City 1970) 167

[203] A. Jorio, A. G. S. Filho, G. Dresselhaus, M. S. Dresselhaus, R. Saito, J. H. Hafner, C. M. Lieber, F. M. Matinaga, M. S. S. Dantas, M. A. Pimenta: Joint density of electronic states for one isolated single-wall carbon nanotube studied by resonant Raman scattering, Phys. Rev. B **63**, 245416 (2001) 168

[204] A. G. S. Filho, A. Jorio, J. H. Hafner, C. M. Lieber, R. Saito, M. A. Pimenta, G. Dresselhaus, M. S. Dresselhaus: Electronic transition energy E_{ii} for an isolated (n, m) single-wall carbon nanotube obtained by anti-Stokes/Stokes resonant Raman intensity ratio, Phys. Rev. B **63**, 241404 (2001) 168

[205] A. G. Souza Filho, S. G. Chou, G. G. Samsonidze, G. Dresselhaus, M. S. Dresselhaus, L. An, J. Liu, A. K. Swan, M. S. Ünlü, B. B. Goldberg, A. Jorio, A. Grüneis, R. Saito: Stokes and anti-Stokes Raman spectra of small-diameter isolated carbon nanotubes, Phys. Rev. B **69**, 115 428 (2004) 168, 177, 207

[206] J. Maultzsch, S. Reich, C. Thomsen: Chirality selective Raman scattering of the D-mode in carbon nanotubes, Phys. Rev. B **64**, 121407(R) (2001) 169, 208, 209, 210, 211

[207] J. Maultzsch, S. Reich, C. Thomsen: Double-resonant Raman scattering in graphite: Interference effects, selection rules, and phonon dispersion, Phys. Rev. B **70**, 155403 (2004) 169, 170, 171, 173, 205, 207, 212, 213, 215

[208] S. I. Gubarev, T. Ruf, M. Cardona: Doubly resonant Raman scattering in the semimagnetic semiconductor $Cd_{0.95}Mn_{0.05}Te$, Phys. Rev. B **43**, 1551 (1991) 170

[209] V. Sapega, M. Cardona, K. Ploog, E. Irchenko, D. Mirlin: Spin-flip Raman scattering in $GaAs/Al_xGa_{1-x}As$ multiple quantum wells, Phys. Rev. B **45**, 4320 (1992) 170

[210] R. P. Vidano, D. B. Fischbach, L. J. Willis, T. M. Loehr: Observation of Raman band shifting with excitation wavelength for carbons and graphites, Solid State Commun. **39**, 341 (1981) 171, 172, 207, 212

[211] P.-H. Tan, Y.-M. Deng, Q. Zhao: Temperature-dependent Raman spectra and anomalous Raman phenomenon of highly oriented pyrolytic graphite, Phys. Rev. B **58**, 5435 (1998) 171, 173, 207

[212] V. A. Gaisler, I. G. Neizvestnyi, M. P. Singukov, A. B. Talochkin: JETP Lett. **45**, 441 (1987) 172

[213] D. Mowbray, H. Fuchs, D. Niles, M. Cardona, C. Thomsen, B. Friedl: Raman study of the Ge phonon side band, in E. Anastassakis, J. Joannopoulos (Eds.): *20th International Conference on the Physics of Semiconductors* (World Scientific, Singapore 1990) p. 2017 172, 207, 210

[214] M. Mohr, M. Machón, J. Maultzsch, C. Thomsen: Double-resonant Raman processes in germanium: Group theory and *ab initio* calculations, Phys. Rev. B **73**, 035217 (2006) 172, 207, 210

[215] I. Pócsik, M. Hundhausen, M. Koos, L. Ley: Origin of the D peak in the Raman spectrum of microcrystalline graphite, J. Non-Cryst. Solids **227–230B**, 1083 (1998) 172, 215, 216

[216] Y. Wang, D. C. Alsmeyer, R. L. McCreery: Raman spectroscopy of carbon materials: Structural basis of observed spectra, Chem. Mater. **2**, 557 (1990) 172, 215, 216

[217] M. J. Matthews, M. A. Pimenta, G. Dresselhaus, M. S. Dresselhaus, M. Endo: Origin of dispersive effects of the Raman D band in carbon materials, Phys. Rev. B **59**, R6585 (1999) 172

[218] F. Tuinstra, J. L. Koenig: Raman spectrum of graphite, J. Chem. Phys. **53**, 1126 (1970)   172, 207, 213

[219] V. Zólyomi, J. Kürti: Phys. Rev. B **66**, 73418 (2002)   173, 207, 214

[220] C. Mapelli, C. Castiglioni, G. Zerbi, K. Müllen: Phys. Rev. B **60**, 12710 (1999)   173

[221] C. Castiglioni, F. Negri, M. Rigolio, G. Zerbi: J. Chem. Phys. **115**, 3769 (2001)   173

[222] A. Ferrari, J. Robertson: Phys. Rev. B **64**, 75414 (2001)   173

[223] P. Tan, L. An, L. Liu, Z. Guo, R. Czerw, D. L. Carroll, P. M. Ajayan, N. Zhang, H. Guo: Phys. Rev. B **66**, 245410 (2002)   173, 215, 216

[224] L. D. Landau, E. M. Lifschitz: *Elektrodynamik der Kontinua* (Akademie-Verlag, Berlin 1967)   174

[225] L. X. Benedict, S. G. Louie, M. L. Cohen: Phys. Rev. B **52**, 8541 (1995)   174

[226] S. Tasaki, K. Maekawa, T. Yamabe: π -band contribution to the optical properties of carbon nanotubes: Effects of chirality, Phys. Rev. B **57**, 9301 (1998)   174

[227] C. Thomsen, S. Reich, P. M. Rafailov, H. Jantoljak: Symmetry of the high-energy modes in carbon nanotubes, phys. stat. sol. B **214**, R15 (1999)   175

[228] J. Hwang, H. H. Gommans, A. Ugawa, H. Tashiro, R. Haggenmueller, K. I. Winey, J. E. Fischer, D. B. Tanner, A. G. Rinzler: Polarized spectroscopy of aligned single-wall carbon nanotubes, Phys. Rev. B **62**, R13 310 (2000)   175

[229] A. Hartschuh, E. J. Sánchez, X. S. Xie, L. Novotny: Phys. Rev. Lett. **90**, 95503 (2003)   175

[230] C. Thomsen, S. Reich, J. Maultzsch: Resonant Raman spectroscopy of nanotubes, in A. C. Ferrari, J. Robertson (Eds.): *Raman Spectroscopy in Carbons: From Nanotubes to Diamond* (Philosophical Transaction of the Royal Society 2004) p. 2337   175, 207, 208, 209

[231] H. Kuzmany, R. Pfeiffer, M. Hulman, C. Kramberger: Raman spectroscopy of fullerenes and fullerene-nanotube composites, in A. C. Ferrari, J. Robertson (Eds.): *Raman Spectroscopy in Carbons: From Nanotubes to Diamond* (Philosophical Transaction of the Royal Society 2004) p. 2375   176

[232] R. Pfeiffer, H. Kuzmany, T. Pichler, H. Kataura, Y. Achiba, M. Melle-Franco, F. Zerbetto: Electronic and mechanical coupling between guest and host in carbon peapods, Phys. Rev. B **69**, 035404 (2004)   175, 176

[233] P. M. Rafailov, V. G. Hadjiev, H. Jantoljak, C. Thomsen: Raman depolarization ratio of vibrational modes in solid C_{60}, Solid State Commun. **112**, 517 (1999)   176

[234] W. Hayes, R. Loudon: *Scattering of Light by Crystals* (Wiley and Sons Inc., New York 1978)   176

[235] P. Rafailov, C. Thomsen, K. Gartsman, I. Kaplan-Ashiri, R. Tenne: Orientation dependence of the polarizability of an individual WS_2 nanotube by resonant Raman spectroscopy, Phys. Rev. B **72**, 205436 (2005)   176, 177

[236] A. Jorio, R. Saito, J. H. Hafner, C. M. Lieber, M. Hunter, T. McClure, G. Dresselhaus, M. S. Dresselhaus: Structural (n, m) determination of isolated single-wall carbon nanotubes by resonant Raman scattering, Phys. Rev. Lett. **86**, 1118 (2001)   177

[237] H. Kuzmany, W. Plank, M. Hulman, C. Kramberger, A. Grüneis, T. Pichler, H. Peterlik, H. Kataura, Y. Achiba: Determination of SWCNT diameters from the Raman response of the radial breathing mode, Eur. Phys. J. B **22**, 307 (2001) 177

[238] C. L. Kane, E. J. Mele: Phys. Rev. Lett. **90**, 207401 (2003) 179

[239] G. G. Samsonidze, R. Saito, N. Kobayashi, A. Grüneis, J. Jiang, A. Jorio, S. G. Chou, G. Dresselhaus, M. S. Dresselhaus: Family behavior of the optical transition energies in single-wall carbon nanotubes of smaller diameters, Appl. Phys. Lett. **85**, 5703 (2005) 179

[240] C. Thomsen, H. Telg, J. Maultzsch, S. Reich: Chirality assignments in carbon nanotubes based on resonant Raman scattering, phys. stat. sol. **242** (2005) 179

[241] S. K. Doorn, D. A. Heller, P. W. Barone, M. L. Usrey, M. S. Strano: Resonant Raman excitation profiles of individually dispersed single walled carbon nanotubes in solution, Appl. Phys. A: Mater. Sci. Process. **78**, 1147 (2004) 179, 196, 197

[242] J. Maultzsch, H. Telg, S. Reich, C. Thomsen: Resonant Raman scattering in carbon nanotubes: Optical transition energies and chiral-index assignment, Phys. Rev. B **72**, 205438 (2005) 179, 180, 181, 182, 183, 185, 186, 187, 197, 198, 202

[243] I. Farkas, D. Helbing, T. Vicsek: Nature **419**, 131 (2002) 180

[244] C. Thomsen, S. Reich, A. R. Goñi, H. Jantoljak, P. Rafailov, I. Loa, K. Syassen, C. Journet, P. Bernier: Intramolecular interaction in carbon nanotube ropes, phys. stat. sol. B **215**, 435 (1999) 185

[245] M. J. O'Connell, S. Sivaram, S. K. Doorn: Near-infrared resonance Raman excitation profile studies of single-walled carbon nanotube intertube interactions: A direct comparison of bundled and individually dispersed hipco nanotubes, Phys. Rev. B **69**, 235 415 (2004) 185, 204

[246] R. B. Weisman, S. M. Bachilo: Nano Lett. **3**, 1235 (2003) 185

[247] A. Hagen, G. Moos, V. Talalaev, T. Hertel: Electronic structure and dynamics of optically excited single-wall carbon nanotubes, Appl. Phys. A: Mater. Sci. Process. **78**, 1137 (2004) 185

[248] R. Krupke: (2005) private communication 189

[249] R. Saito, T. Takeya, T. Kimura, G. Dresselhaus, M. S. Dresselhaus: Raman intensity of single-wall carbon nanotubes, Phys. Rev. B **57**, 4145 (1998) 191

[250] M. Lazzeri, S. Piscanec, F. Mauri, A. C. Ferrari, J. Robertson: Phonon linewidths and electron phonon coupling in nanotubes, Phys. Rev. B **73**, 155426 (2006) 191

[251] H. Telg, J. Maultzsch, S. Reich, C. Thomsen: Chirality dependence of the high-energy Raman modes in carbon nanotubes, in H. Kuzmany, J. Fink, M. Mehring, S. Roth (Eds.): *Electronic Properties of Novel Materials*, IWEPNM Kirchberg (2005) p. 162 191

[252] M. Paillet, P. Poncharal, A. Zahab, J.-L. Sauvajol, J. C. Meyer, S. Roth: Vanishing of the Breit-Wigner-Fano component in individual single-wall carbon nanotubes, Phys. Rev. Lett. **94**, 237 401 (2005) 191, 212

[253] C. Thomsen, J. Maultzsch, H. Telg, S. Reich: private communication 191, 212

[254] A. J. Shields, M. P. Chamberlain, M. Cardona, K. Eberl: Raman scattering due to interface optical phonons in GaAs/AlAs multiple quantum wells, Phys. Rev. B **51**, 17 728 (1995)   193

[255] C. Liu, A. J. Bard, F. Wudl, I. Weitz, J. R. Heath: Electrochem. Solid-State Lett. **2**, 577 (1999)   193

[256] A. S. Claye, J. E. Fisher, C. B. Huffman, A. G. Rinzler, R. E. Smalley: J. Electrochem. Soc. **147**, 2845 (2000)   193

[257] S. J. Tans, A. Verschueren, C. Dekker: Room-temperature transistor based on a single carbon nanotube, Nature (London) **393**, 6680 (1998)   193

[258] A. Modi, N. Koratkar, E. Lass, B. Wei, P. M. Ajayan: Nature (London) **424**, 171 (2003)   193

[259] A. M. Rao, P. C. Eklund, S. Bandow, A. Thess, R. E. Smalley: Evidence for charge transfer in doped carbon nanotube bundles from Raman scattering, Nature **388**, 257 (1997)   193

[260] S. Kazaoui, N. Minami, R. Jacquemin: Phys. Rev. B **60**, 13339 (1999)   193, 195

[261] L. Grigorian, K. A. Williams, S. Fang, G. U. Sumanasekera, A. L. Loper, E. C. Dickey, S. J. Pennycook, P. C. Eklund: Phys. Rev. Lett. **80**, 5560 (1998)   193

[262] N. Bendiab, L. Spina, A. Zahab, P. Poncharal, C. Marliere, J. L. Bantignies, E. Anglaret, J. L. Sauvajol: Phys. Rev. B **63**, 153407 (2001)   193

[263] N. Bendiab, E. Anglaret, J. L. Bantignies, A. Zahab, J. L. Sauvajol, P. Petit, C. Mathis, S. Lefrant: Phys. Rev. B **64**, 245424 (2001)   193

[264] T. Pichler, A. Kukovecz, H. Kuzmany, H. Kataura, Y. Achiba: Phys. Rev. B **67**, 125416 (2003)   193

[265] L. Kavan, P. Rapta, L. Dunsch: Raman and Vis-NIR spectroelectrochemistry at single-walled carbon nanotubes, Chem. Phys. Lett. **328**, 363 (2000)   193, 195

[266] L. Kavan, L. Dunsch, H. Kataura: Carbon **42**, 1011 (2004)   193

[267] P. Rafailov, J. Maultzsch, C. Thomsen, H. Kataura: Electrochemical switching of the Peierls-like transition in metallic single-walled carbon nanotubes, Phys. Rev. B **72**, 045411 (2005)   193, 194, 195, 196

[268] P. Corio, A. Jorio, N. Demir, et al.: Spectro-electrochemical studies of single wall carbon nanotubes films, Chem. Phys. Lett. **392**, 396 (2004)   193

[269] L. Kavan, P. Rapta, L. Dunsch, M. J. Bronikowski, P. Willis, R. Smalley: J. Phys. Chem. B **105**, 10764 (2001)   194, 195

[270] J. N. Barisci, G. G. Wallace, R. H. Baughman, L. Dunsch: J. Electroanalyt. Chem. **488**, 92 (2000)   194

[271] M. Stoll, P. M. Rafailov, W. Frenzel, C. Thomsen: Chem. Phys. Lett. **375**, 625 (2003)   194

[272] S. Gupta, M. Hughes, A. H. Windle, J. Robertson: Charge transfer in carbon nanotube actuators investigated using in situ Raman spectroscopy, J. Appl. Phys. **95**, 2038 (2004)   194

[273] P. Rafailov, M. Stoll, C. Thomsen: J. Phys. Chem. Solids **108**, 19241 (2004)   194

[274] P. Corio, P. S. Santos, V. W. Brar, G. G. Samsonidze, S. G. Chou, M. S. Dresselhaus: Chem. Phys. Lett. **370**, 675 (2003)   195

[275] L. Kavan, L. Dunsch, H. Kataura: Chem. Phys. Lett. **361**, 79 (2002)   195

[276] N. W. Ashcroft, N. D. Mermin: *Solid State Physics* (Saunders College, Philadelphia 1976) 196

[277] J. B. Renucci, R. N. Tyte, M. Cardona: Resonant Raman scattering in silicon, Phys. Rev. B **11**, 3885 (1975) 196

[278] R. Trommer, M. Cardona: Phys. Rev. B **17**, 1865 (1973) 196

[279] J. M. Calleja, J. Kuhl, M. Cardona: Phys. Rev. B **17**, 876 (1978) 196

[280] S. V. Goupalov: Chirality dependence in the Raman cross section, Phys. Rev. B **71**, 153404 (2005) 197, 199

[281] F. S. Khan, P. B. Allen: Deformation potentials and electron-phonon scattering: Two new theorems, Phys. Rev. B **29**, 3341 (1984) 198

[282] J. Jiang, R. Saito, A. Grüneis, S. G. Chou, G. G. Samsonidze, A. Jorio, G. Dresselhaus, M. S. Dresselhaus: Intensity of the resonance Raman excitation spectra of single-wall carbon nanotubes, Phys. Rev. B **71**, 205420 (2005) 199, 204

[283] R. E. Peierls: *Quantum Theory of Solids* (Oxford University Press, New York 1955) 205

[284] A. Jorio, A. G. Souza Filho, G. Dresselhaus, M. S. Dresselhaus, A. K. Swan, M. S. Ünlü, B. B. Goldberg, M. A. Pimenta, J. H. Hafner, C. M. Lieber, R. Saito: Phys. Rev. B **65**, 155412 (2002) 207

[285] J. Kürti, V. Zólyomi, A. Grüneis, H. Kuzmany: Phys. Rev. B **65**, 165433 (2002) 209

[286] C. Jiang, J. Zhao, H. A. Therese, M. Friedrich, A. Mews: J. Phys. Chem. B **107**, 8742 (2003) 209, 210

[287] L. Cançado, M. A. Pimenta, B. R. A. Nevesand, M. S. S. Dantas, A. Jorio: Influence of the atomic structure on the Raman spectra of graphite edges, Phys. Rev. Lett. **93**, 247401 (2004) 210, 211

[288] M. Machón, S. Reich, J. Maultzsch, H. Okudera, A. Simon, R. Herges, C. Thomsen: Structural, electronic and vibrational properties of (4,4) picotube crystals, Phys. Rev. B **72**, 155 402 (2005) 211, 212

[289] S. Kammermeier, P. G. Jones, R. Herges: Angew. Chem. Int. Ed. Engl. **35**, 2669 (1996) 211

[290] S. Kammermeier, P. G. Jones, R. Herges: Angew. Chem. **108**, 2834 (1996) 211

[291] M. Souza, A. J. C. Fantini, B. R. A. Neves, M. A. Pimenta, R. Saito, A. Ismach, E. Joselevich, V. W. Brar, G. G. Samsonidze, G. Dresselhaus, M. S. Dresselhaus: Single- and double-resonance Raman G-band processes in carbon nanotubes, Phys. Rev. B **69**, 241403 (2004) 214

[292] J. Maultzsch, S. Reich, C. Thomsen, S. Webster, R. Czerw, D. L. Carroll, S. M. C. Vieira, P. R. Birkett, C. A. Rego: Raman characterization of boron-doped multiwalled carbon nanotubes, Appl. Phys. Lett. **81**, 2647 (2002) 214

[293] R. J. Nemanich, S. A. Solin: First- and second-order Raman scattering from finite-size crystals of graphite, Phys. Rev. B **20**, 392 (1979) 214

[294] M. Reedyk, C. Thomsen, M. Cardona, J. S. Xue, J. E. Greedan: Observation of the effects of phonon dispersion on the Fröhlich-interaction-induced second-order Raman scattering in $Pb_2Sr_2PrCu_3O_8$, Phys. Rev. B **50**, 13762 (1994) 214

[295] R. Saito, A. Jorio, A. G. Souza-Filho, G. Dresselhaus, M. S. Dresselhaus, M. A. Pimenta: Phys. Rev. Lett. **88**, 27401 (2002) 215

[296] Y. Kawashima, G. Katagiri: Phys. Rev. B **52**, 10053 (1995) 215, 216

[297] P. Tan, C. Hu, J. Dong, W. Shen, B. Zhang: Phys. Rev. B **64**, 214301 (2001)
215, 216